NASA CR-54078

FZK-186-1

152 p

NUCLEAR RADIATION HEATING IN LIQUID HYDROGEN

VOLUME I: DESCRIPTION AND EXPERIMENT AND DISCUSSION OF RESULTS

by

W. A. Hehs
B. O. McCauley
G. E. Miller
D. M. Wheeler

prepared for

NATIONAL AERONAUTICS AND SPACE ADMINISTRATION

Contract NAS 3-3324

NUCLEAR AEROSPACE RESEARCH FACILITY

operated by
General Dynamics/Fort Worth

NOTICE

This report was prepared as an account of Government sponsored work. Neither the United States, nor the National Aeronautics and Space Administration (NASA), nor any person acting on behalf of NASA:

A.) Makes any warranty or representation, expressed or implied, with respect to the accuracy, completeness, or usefulness of the information contained in this report, or that the use of any information, apparatus, method, or process disclosed in this report may not infringe privately owned rights; or

B.) Assumes any liabilities with respect to the use of, or for damages resulting from the use of any information, apparatus, method or process disclosed in this report.

As used above, "persons acting on behalf of NASA" includes any employee or contractor of NASA, or employee of such contractor, to the extent that such employee or contractor of NASA, or employee of such contractor prepares, disseminates, or provides access to, any information pursuant to his employment or contract with NASA, or his employment with such contractor.

Request for copies of this report
should be referred to:

National Aeronautics and Space Administration
Office of Scientific and Technical Information
Washington 25, D.C.
Attention: AFSS-A

NASA CR-54078
FZK-186-I

NUCLEAR RADIATION HEATING IN LIQUID HYDROGEN

VOLUME I: DESCRIPTION AND EXPERIMENT AND DISCUSSION OF RESULTS

by

W. A. Hehs
B. O. McCauley
G. E. Miller
D. M. Wheeler

prepared for

NATIONAL AERONAUTICS AND SPACE ADMINISTRATION

30 JUNE 1964

Contract NAS 3-3324

Technical Management
NASA-Lewis Research Center
Advanced Development and Evaluation Division
Cleveland, Ohio
D. J. Connolley

NUCLEAR AEROSPACE RESEARCH FACILITY

operated by
General Dynamics/Fort Worth

A

ABSTRACT

A comprehensive collection of data is given for evaluating methods to calculate the nuclear-radiation energy-deposition rates and the resultant temperature distributions in liquid hydrogen in a pressurized tank.

Nuclear measurements provide data to determine heating gradients in the liquid hydrogen and to determine the contributions of neutron interactions and gamma interactions to the total heating rates. Boil-off and self-pressurization measurements determined the total heat input into the cryogenic system.

Temperature distributions in the liquid hydrogen were monitored under variable flow conditions: pressurization, flow rate, heating gradient, and heat input. No analysis of the resultant temperature distributions in the hydrogen was performed. Background information and accuracy of the data required to perform and evaluate an analysis have been provided.

The results of nuclear analyses made during the study with the C-17 shield penetration code and with the COHORT Monte Carlo procedures compare favorably with the measured nuclear-radiation distributions and energy-deposition rates. author

FOREWORD

The report of an investigation into nuclear-radiation heating of liquid hydrogen has been divided into two volumes. A description of the experimental equipment and procedures and a discussion of the results are contained in this volume, Volume I. The experimental data have been compiled in Volume II. The investigations were performed under Contract NAS 3-3324 at the Nuclear Aerospace Research Facility (NARF), General Dynamics/Fort Worth. The effort was sponsored by the National Aeronautics and Space Agency and was directed by the Lewis Research Center.

The authors wish to thank D. J. Connolley and his group at Lewis Research Center for their help in planning the investigation and in interpreting the data and H. G. Carter and J. J. Long of the Nuclear Shielding Group at NARF for performing the nuclear-radiation wall-heating and COHORT analyses.

TABLE OF CONTENTS

TABLE OF CONTENTS (Cond't)

LIST OF FIGURES

LIST OF FIGURES (Cont'd)

LIST OF FIGURES (Cont'd)

LIST OF TABLES

1. INTRODUCTION

The use of liquid hydrogen as the propellant for nuclear rocket engines has posed several vehicle-system design uncertainties. Among these is the uncertainty of the effects of heat generation in the propellant due to nuclear-radiation absorption with consequent effects on tank-pressurization requirements, on fluid conditions as the propellant is delivered to the turbopump, and on the propellant loss due to boil-off. Several calculational methods are in use to predict nuclear-radiation energy deposition rates and the resulting effects; however, these predictions are complicated by uncertainties in the nuclear-energy absorption rates, and the mixing behavior of liquid hydrogen in a propellant tank.

An experiment, sponsored by Lewis Research Center (LRC), was designed to provide information on the above uncertainties by (1) measuring the nuclear-radiation distributions in liquid hydrogen, (2) determining heat-generation rates under various system pressures and liquid volumes, and (3) measuring temperature distributions (degree of mixing or stratification) with combined thermal leakage and nuclear heating in the liquid hydrogen.

The Aerospace Systems Test Reactor (ASTR) was used as the radiation source to induce nuclear heating in a 125-gal tank of liquid hydrogen. The hydrogen tank and nuclear-radiation intensities were scaled to obtain useful magnitudes of heating.

The tests performed included:

- Measurement of nuclear heat generation in the tank walls.

- Mapping of radiation intensities in the tank, with and without LH_2.
- Measurement of self-pressurization rates and temperature distribution for various volumes of LH_2, with and without nuclear heating.
- Measurement of liquid vaporization rates as a function of tank content, with and without nuclear heating.
- Measurement of temperature distributions as a function of time with various liquid out-flow rates, heating rates, and pressurizations.

The above tests were performed with each of two different nuclear-heat-deposition gradients, obtained by altering the relative magnitude of the neutron and gamma-ray source intensities.

In addition to making the above measurements, calculations of the nuclear-radiation distributions and heat deposition in the liquid hydrogen and tank wall were made and compared with the experimental data. Other secondary results of the experiment were the experience gained in the operation of temperature sensors in nuclear-radiation fields, radiation detectors in LH_2, and cryogenic systems in the vicinity of nuclear reactors.

A brief description of the experimental setup and instrumentation is presented in Section 2; detailed descriptions may be found in Appendices A and B. The general procedures followed in performing the various tests are given in Section 3 to aid in the interpretation of the tests and utilization of the resultant data.

The results and discussions of the tests and calculations are presented in Section 4. Calculational methods and assumptions used in the nuclear analyses are given in Appendix C. The experimental data are presented in graphical and tabular form in Volume II.

2. EXPERIMENTAL SETUP AND INSTRUMENTATION.

The experimental hardware and instrumentation are discussed only briefly here, a more detailed description with operational details being given in Appendices A and B.

2.1 Experimental Geometry and Hardware

The experimental arrangement was designed to simulate the radiation source and liquid-hydrogen propellant-tank geometry of a typical nuclear-rocket-system design. The ASTR was utilized as the source of nuclear radiation, and a 125-gal liquid-hydrogen tank served as a scaled-down propellant tank. The hydrogen tank was centered in a vertical position over the radiation source. The LH_2 tank was cylindrical with a conical bottom. The diameter of the cylinder was 32 in., and the half-angle of the conical bottom was 45°.

A sketch of the experimental arrangement is shown in Figure 2.1-1. A liner tank, fastened between two I-beams spanning the water-filled ASTR pit, provided a dry volume above the reactor in which the LH_2 tank, or dewar, was positioned. The bottom of the liner tank was shaped to fit the curved surface of the reactor vessel so that the reactor could be raised into position snugly under the liner tank. With the reactor in this position, only about 1/4 in. of water separated the reactor pressure vessel and the liner tank. This geometry was called Configuration 1. The reactor pressure vessel was lowered 4 in. for the second experimental geometry, Configuration 2. These experimental configurations are illustrated in Figure 2.1-2.

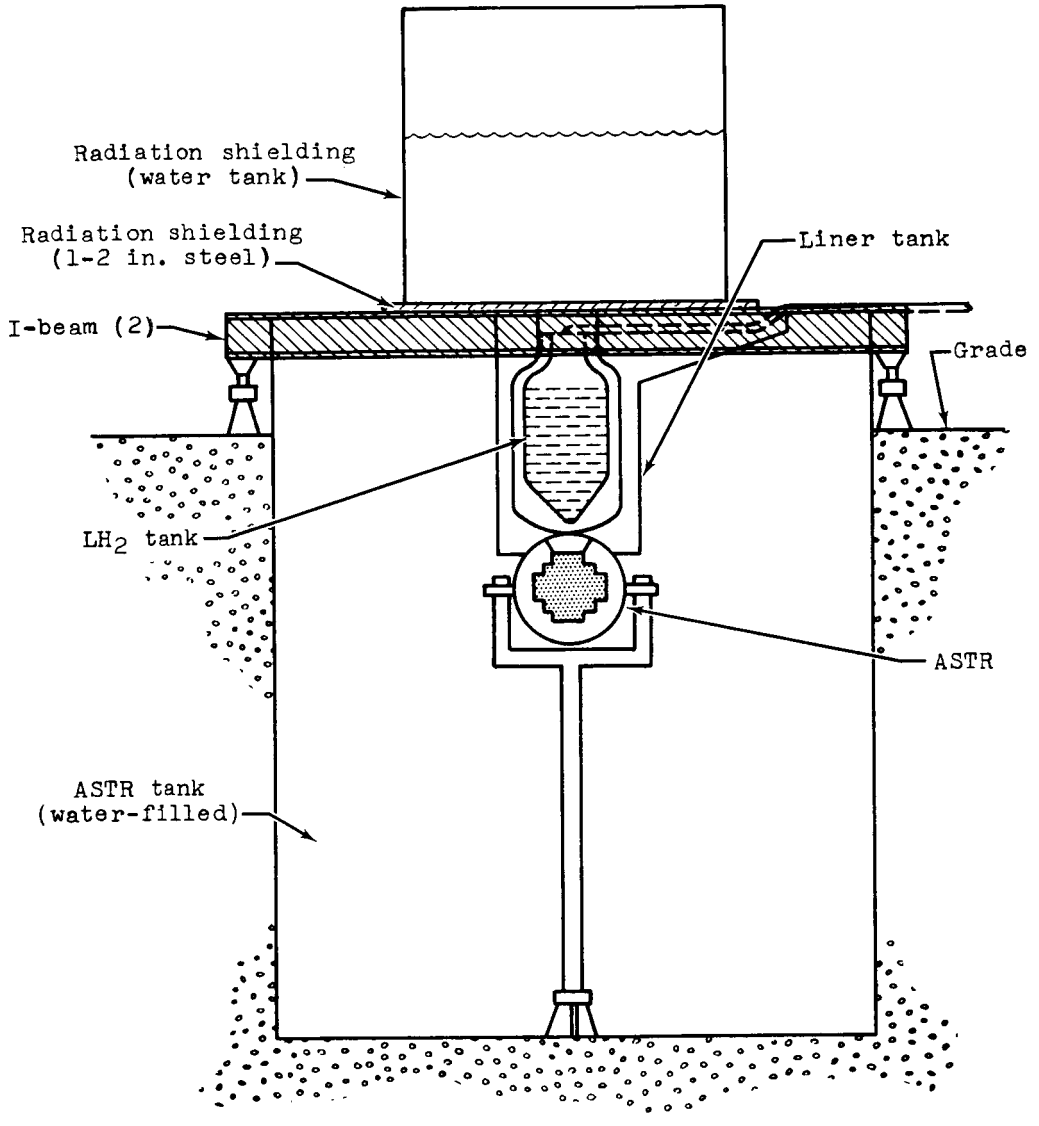

Figure 2.1-1 Experimental Setup

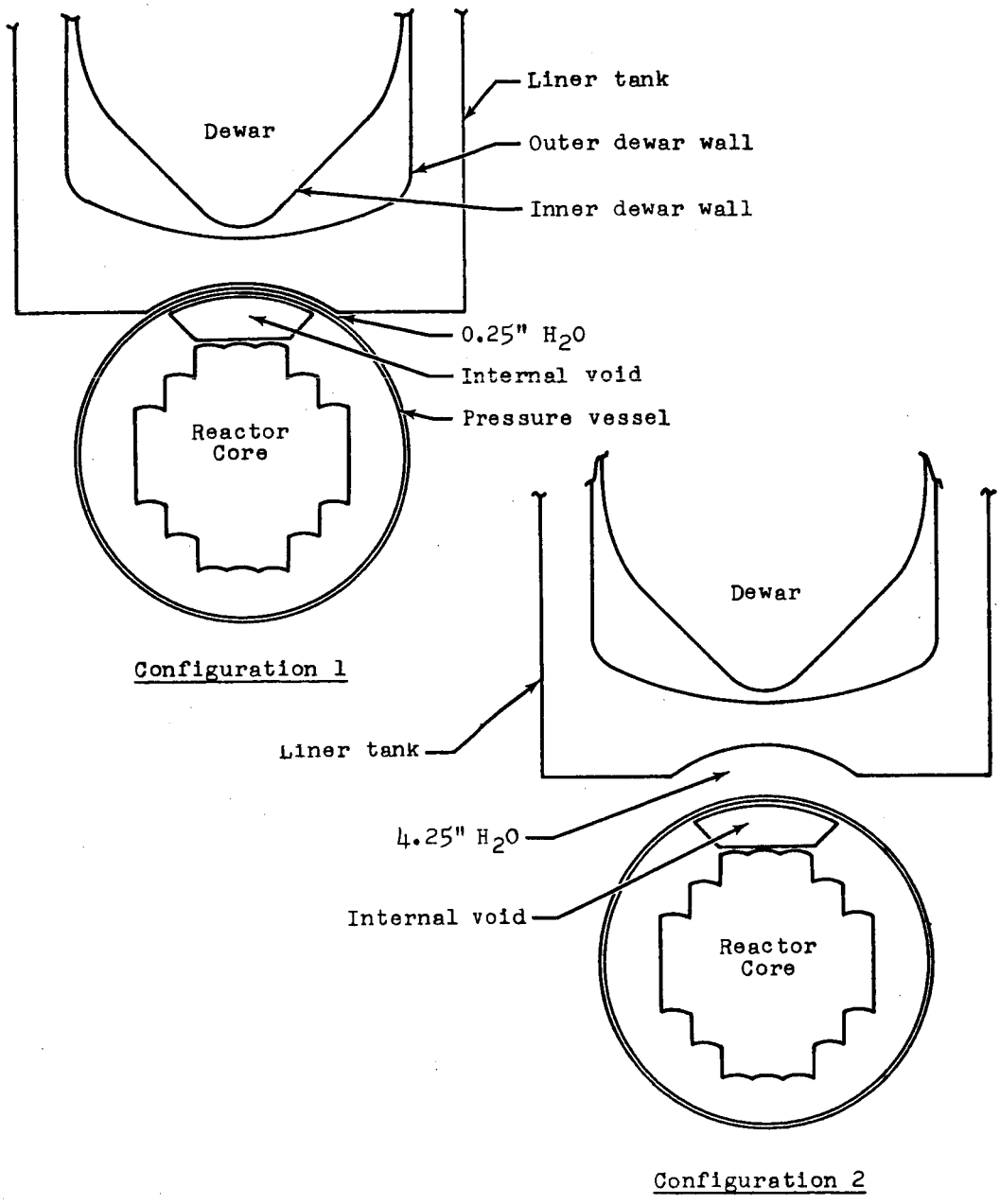

Figure 2.1-2 Liquid-Hydrogen Heating Experimental Configurations

The two configurations made available two different neutron-to-gamma ratios and, consequently, two different nuclear heating profiles in the liquid hydrogen. Changing the neutron-to-gamma ratio changes the nuclear heating profiles by virtue of the rather large difference in attenuation factors of neutrons and gamma rays in liquid hydrogen. Neutron attenuation is much higher. Thus, in the higher neutron-to-gamma ratio configuration, more of the nuclear energy is deposited in the lower portion of the hydrogen tank because the neutron flux decreases rapidly in the liquid hydrogen. In the lower neutron-to-gamma ratio configuration (Configuration 2), where the energy deposition results primarily from gamma rays, the energy deposition is more evenly distributed in the tank because gamma attenuation in liquid hydrogen is relatively low.

Nuclear-radiation shielding in the form of a steel slab and a tank of water was positioned on the I-beams above the liner tank and hydrogen tank. This was necessary to reduce the radiation leakage to a tolerable level in the surrounding areas.

2.2 Cryogenic System

The cryogenic system, as defined, includes the hydrogen tank and all the associated plumbing. A brief description of the hydrogen tank is given in the preceding section, and a more detailed description is given in Appendix A (Section A-2.1).

The associated plumbing includes the controls and auxiliary systems necessary to perform the various types of test runs. Figure 2.2-1 is a schematic indicating the major components of the system. As indicated in the figure, the plumbing can be divided into three sections: the gas line, the liquid line, and the vent line.

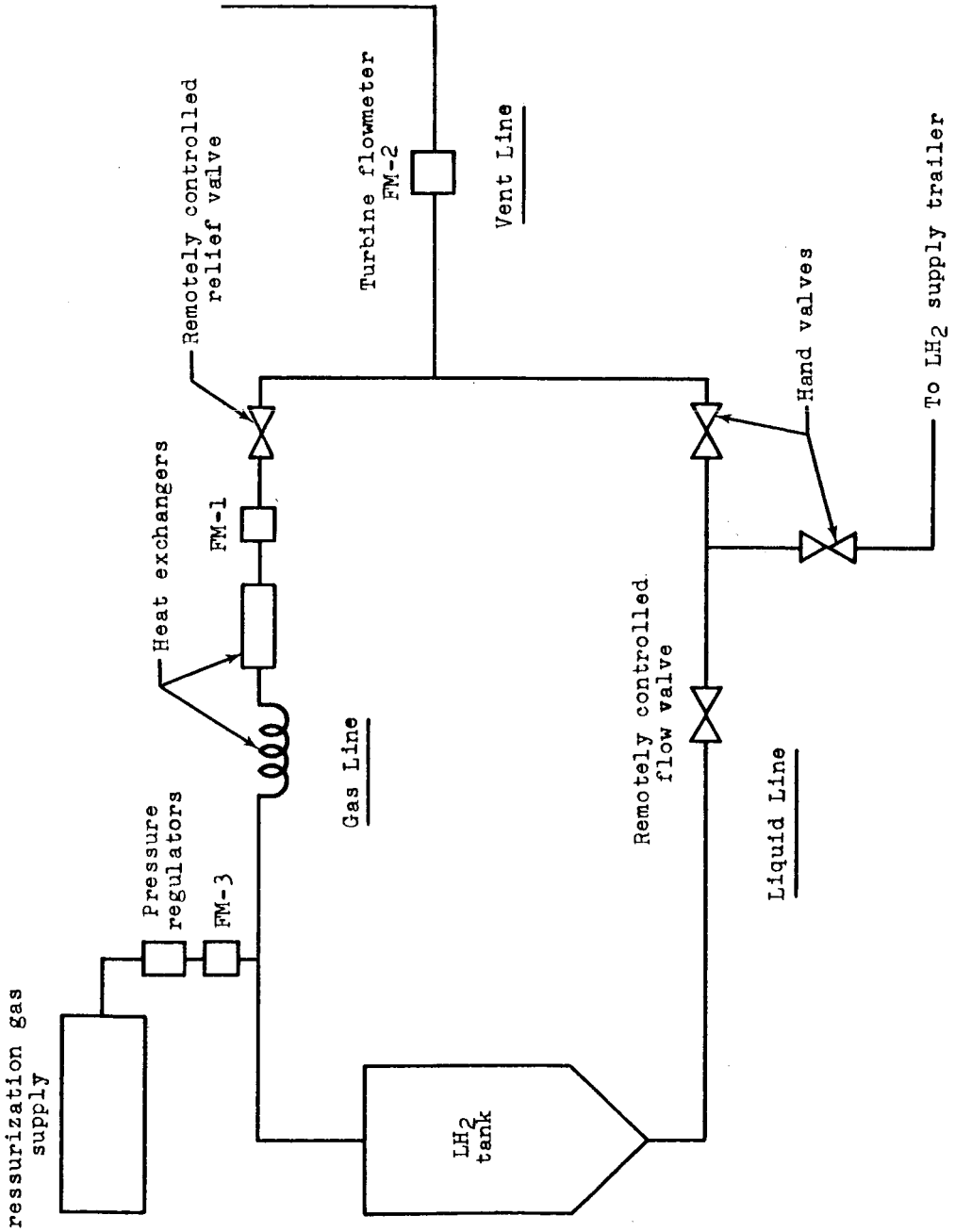

Figure 2.2-1 Cryogenic System Plumbing

The gas-line system controlled the entire system pressure and measured the amount of gas entering or leaving the system, depending upon the type of run. The remotely controlled relief valve regulated the maximum system pressure. In the test runs during which the liquid hydrogen was drained from the tank, the addition of gas was required to maintain the desired pressure in the tank. Hydrogen-gas bottles manifolded together served as the pressurization-gas supply, and regulators set at the desired dewar pressure regulated the gas flow from the gas supply. The amount and rate of pressurization-gas usage was measured by a gas meter (FM-3) in the line.

The other gas meter (FM-1) was used to measure the boil-off, or vaporized gas, from the bulk liquid hydrogen in the tank. The two heat exchangers, or gas heaters, preceding this flowmeter warmed the cold gas to prevent damage to the flowmeter.

Flow in the liquid line was regulated by the remotely controlled valve in the line. The opening of this valve could be varied to allow different liquid-hydrogen flow rates from the tank with a given pressure head.

The hand valves in the liquid line and in the short fill line to the hydrogen-supply trailer directed the hydrogen flow during dewar-filling and -emptying operations.

Both the gas line and the liquid line emptied into the vent line. As the dewar was emptied, the liquid hydrogen was poured directly into the vent line. The liquid hydrogen was vaporized before it reached the gas-turbine flowmeter (FM-2) in the line. The turbine flowmeter was used to monitor, not measure, the liquid flow from the tank. The vent line terminated in a 30-ft-high

stack through which the hydrogen was vented to the atmosphere.

2.3 Instrumentation

2.3.1 Temperature Measurements

Two temperature-measuring systems were utilized in the tests: one for the cryogenic temperature range and one for the ambient temperature range. The cryogenic-temperature-measuring system was composed of 30 platinum resistance thermometers with appropriate readout and recording devices. The positions of these 30 thermometers and 10 carbon-resistor liquid-level indicators are shown graphically in Figure 2.3-1 and tabulated in Table 2.3-1.

Most of the thermometers were placed along the tank centerline to monitor temperatures in the liquid hydrogen as a function of height in the tank. Three sensors were positioned very near the exit port in the bottom of the tank to make certain that valid exit temperatures of the liquid hydrogen were obtained during the liquid-flow tests. Thermometers were also clustered at 1-in. spacings near the full-tank level. These were to determine the degree of stratification during self-pressurization tests and to determine the degree of stratification prior to start of a flow run.

The thermometers on the two radial arms were to determine changes in temperature from the tank center to the tank wall and to determine the thickness of warmed-hydrogen laminar flow along the tank wall.

The output of each thermometer was recorded about every 18.5 seconds. Of the 30 thermometer outputs, ten were connected to a patch panel through which any four could be connected to strip-

NPC 20,707

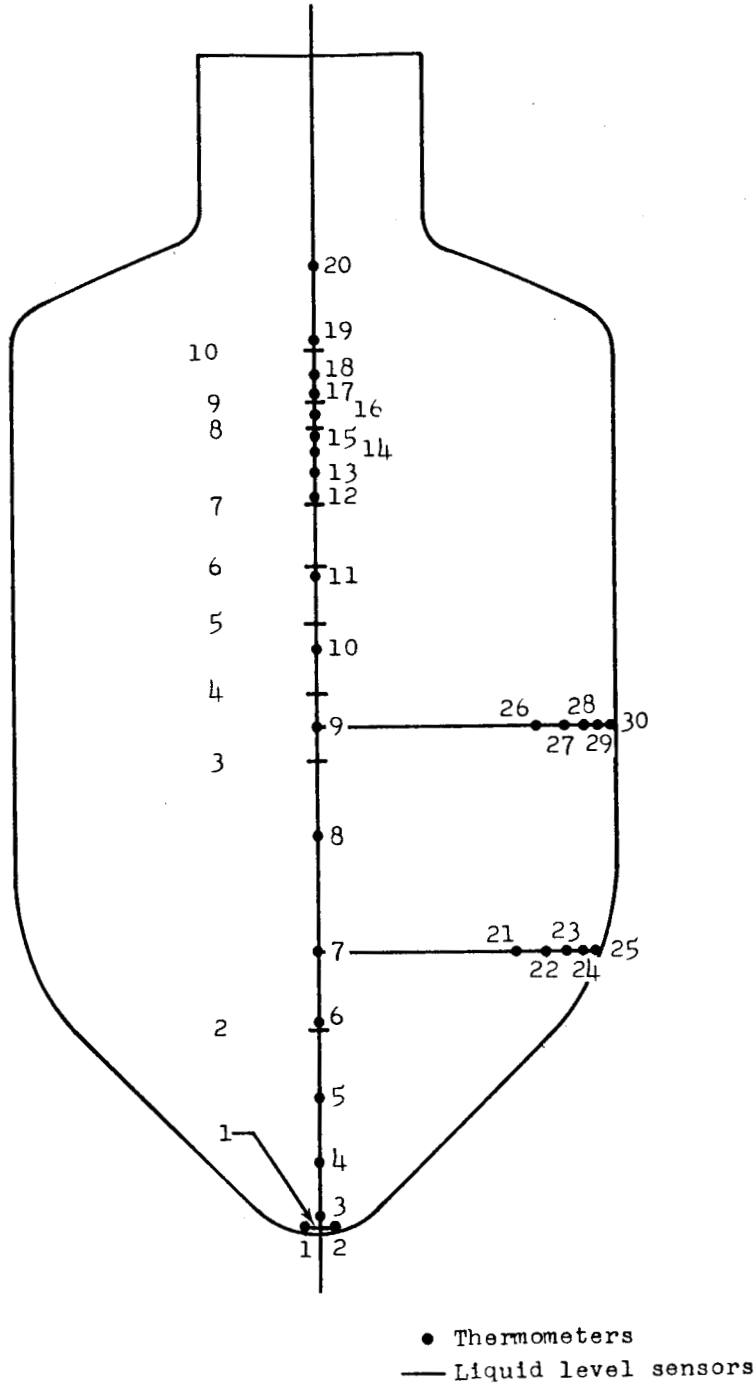

Figure 2.3-1 Thermometer and Liquid-Level Sensor Locations

Table 2.3-1

Thermometer and Liquid-Level-Sensor Locations

Thermometer Number	Liquid Level Sensor	Vertical Height[a] (in.)	Radial Distance From Centerline (in.)	Volume Below Sensor (gal)
20		51.69	0.5	--
19		47.69	0.5	132.5
	10	47.02	0.5	130.1
18		45.69	0.5	125.5
17		44.69	0.5	122.0
	9	44.13	0.5	120.3
16		43.69	0.5	118.5
15		42.69	0.5	115.0
	8	42.69	0.5	115.0
14		41.69	0.5	111.5
13		40.69	0.5	108.5
12		39.44	0.5	104.8
	7	39.25	0.5	103.7
	6	35.78	0.5	91.5
11		35.44	0.5	89.6
	5	32.30	0.5	79.4
10		31.44	0.5	76.1
	4	28.82	0.5	67.2
9		27.44	0.5	62.2
26		26.19	12.0	58.0
27		26.19	14.0	58.0
28		26.19	15.0	58.0
29		26.19	15.5	58.0
30		26.19	16.0	58.0
	3	25.32	0.5	55.0
8		21.44	0.5	41.5
7		15.44	0.5	21.4
21		14.19	12.0	17.7
22		14.19	14.0	17.7
23		14.19	15.0	17.7
24		14.19	15.5	17.7
25		14.19	16.0	17.7
6		11.44	0.5	10.5
	2	10.44	0.5	8.2
5		7.44	0.5	3.7
4		3.94	0.5	0.83
3		1.13	0.5	~0
	1	0.69	0.5	~0
2		0.07	0.5	~0
1		0.07	0.5	~0

[a]From inside bottom of tank.

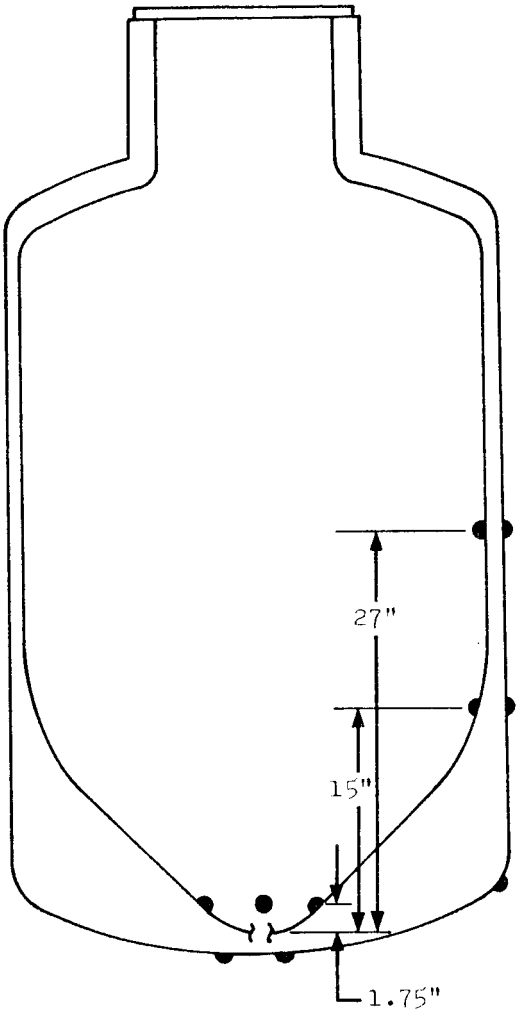

● Thermocouples

Figure 7.3-2 Thermocouple Locations

chart recorders for continuous recording.

The ambient-temperature-measuring system was used to determine the nuclear-energy deposition rates in the walls of the empty dewar by measuring the temperature rise of the walls during irradiation. Ten iron-constantan thermocouples were used for making these measurements. Five of the thermocouples were permanently attached to the outer dewar wall, and five were installed inside the dewar on a positioning rig. The positions of these thermocouples are shown in Figure 2.3-2.

2.3.2 Pressure Measurements

The pressure in the liquid-hydrogen tank was monitored by use of a pressure transducer and visual gages. The visual gages served as backup devices, and the readings from the pressure transducer were used as the recorded experimental data. The accuracy of the pressure measurements was $\pm 8\%$ of the measurement.

2.3.3 Nuclear-Radiation Measurements

The gamma-ray dose was measured by the use of cobalt-glass dosimeters. These were chosen because of their small size and adaptability to the cryogenic environment. Each piece of glass was placed in a small box made of boron-10 and epoxy for protection against slow-neutron effects in the readings of the dosimeters.

The neutron-flux distributions were measured with radioactivants. Gold foils were used as the thermal or subcadmium (< 0.48 ev) neutron-flux detectors, and sulfur, magnesium, and aluminum were used as fast-neutron detectors. Copper wire was

also used to map thermal-neutron profiles in the liquid hydrogen. The fast-neutron detectors were of the threshold reaction type, where the effective thresholds for sulfur, magnesium, and aluminum are 2.9, 7.5, and 8.1 Mev, respectively. The fast-neutron detectors were all 0.75 in. in diameter, and the gold foils were 0.444 in. in diameter.

Figure 2.3-3 shows the locations of the neutron and gamma detectors in and around the tank for each of the reactor runs; only the x,y-plane positions are shown, the x,z-plane position distances being identical. Gamma and all types of neutron detectors were used at the tank bottom and also at 1.4, 8.4, and 20.4 in. from the bottom along the tank centerline. All radiation detectors were also used at each position on the outside wall of the LH_2 tank. Only sulfur neutron detectors and cobalt-glass gamma dosimeters were positioned at all other locations. Copper wires to provide thermal-neutron maps were placed along the tank centerline and along each of the foil-holding radial arms at 21.4 and 33.4 in. from the tank bottom. The sulfur pellets and cobalt glass provided adequate maps of the fast-neutron and gamma-ray distributions, respectively, in the tank.

The radiation detectors were packeted between aluminum screen wire and attached to the foil support stand with steel wire. The foil support stand was fabricated of small-diameter stainless-steel rods.

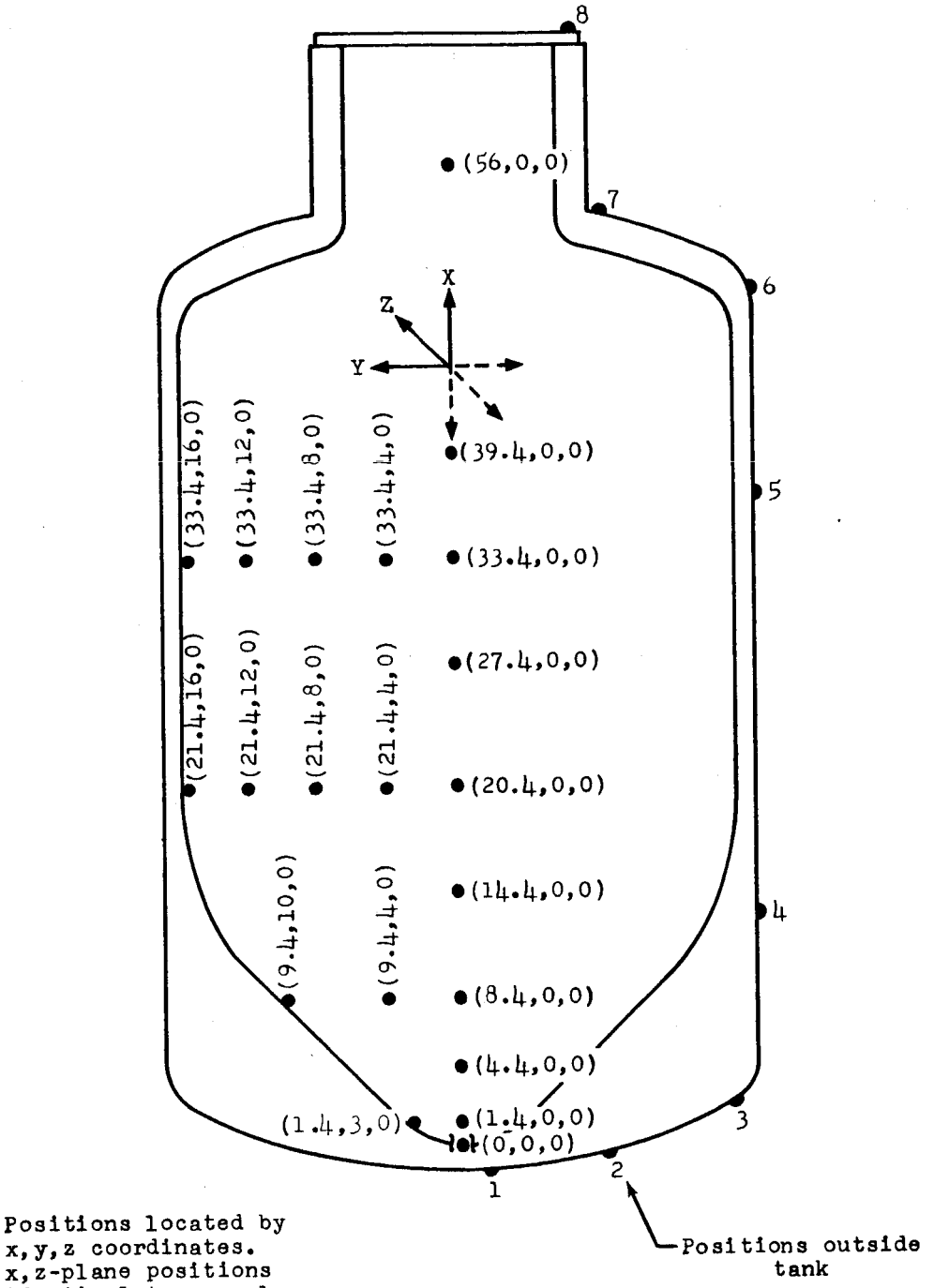

Figure 2.3-3 Diagram of Radiation-Detector Positions

3. EXPERIMENTAL PROCEDURES

There were basically five different types of tests or test runs required to make the desired measurements. These were as follows:

1. Nuclear-radiation mapping
2. Tank-wall nuclear heating
3. Liquid vaporization
4. Tank self-pressurization
5. Liquid flow from tank

The first four types of runs were either directly or indirectly concerned with the determination of the nuclear-energy deposition in the liquid hydrogen. The last type was concerned with the temperature distributions in the liquid hydrogen resulting from the deposition of nuclear energy as a function of time, liquid out-flow rates, heating rates, pressurization, and heating gradients.

In planning the individual test runs of the experiment, run numbers and data objectives were assigned to each run. During the experiment, it became necessary to repeat some of the runs because all data objectives or planned parameters were not met on the original run. Therefore, to distinguish the run and its repeat, the reactor run number was added to each.

A descriptive review of Test Runs 1 through 7 and objectives is as follows:

Run 1. A series of tests on the cryogenic system and instrumentation using both liquid nitrogen and liquid hydrogen

Run 2. Measurement of nuclear heating of the dewar, Configuration 1

Run 3. Measurement of nuclear heating of the dewar, Configuration 2

Run 4. Nuclear radiation mapping with the dewar empty, Configuration 1

Run 5. Nuclear radiation mapping with the dewar empty, Configuration 2

Run 6. Nuclear radiation mapping with the dewar full, Configuration 1

Run 7. Nuclear radiation mapping with the dewar full, Configuration 2

Runs 8 through 13 were concerned with vaporization and self-pressurization measurements for different experimental configurations and liquid levels in the tank. The parameters for each run were:

Run 8. Tank full and no reactor power (measurement of ambient heat leak)

Run 9. Tank half-full and no reactor power

Run 10. Tank full, Configuration 1

Run 11. Tank half-full, Configuration 1

Run 12. Tank full, Configuration 2

Run 13. Tank half-full, Configuration 2

Runs 14 through 23 were concerned with measurement of the temperature distribution in the hydrogen tank as the liquid was flowed from the tank with different combinations of the variable parameters. The parametric conditions for each run were:

Run	Config.	Flow Rate	Pressurization	Approx Reactor Power (Mw)
14	1	.04 lb/sec	30 psia	0.5
15	1	.04 lb/sec	60 psia	1.0
16	1	.12 lb/sec	60 psia	1.0
17	1	.12 lb/sec	60 psia	3.0

Run	Config.	Flow Rate	Pressurization	Approx Reactor Power (Mw)
18	1	.04 lb/sec	30 psia	0.5
19	2	.04 lb/sec	30 psia	1.0
20	2	.04 lb/sec	60 psia	2.0
21	2	.12 lb/sec	60 psia	1.5
22	2	.12 lb/sec	60 psia	6.0
23	2	.12 lb/sec	30 psia	2.0

A general description of the procedures for each type of run follows.

3.1 Nuclear-Radiation Mapping (Runs 4-7)

There were four radiation mapping runs. The radiation distribution in and around the tank was measured both with the tank empty and with the tank full of liquid hydrogen for each of the two reactor configurations. Both neutron and gamma measurements were obtained on each reactor run.

Prior to the experiment, the radiation detectors were placed on positioning rigs and tapes for each of the four runs. For the radiation measurements inside the tank, the detectors were fastened onto the stainless-steel foil-support stand. For the measurements on the outside wall of the tank, the detectors were held in position on a cloth tape.

Prior to each radiation-mapping run, a foil-support stand with the attached radiation detectors was positioned in the tank, and the proper tapes containing radiation detectors were positioned on the outside wall of the tank by means of clothes-line-type cables running to the bottom of the tank. The dewar lid and radiation shielding were then replaced, and the reactor was raised into the proper position.

For the two radiation-mapping runs with the tank full of

hydrogen, the tank was filled to about 45 in. In addition, ten carbon-resistor liquid-level indicators were fastened to the foil support to monitor the hydrogen level.

The reactor run time for each of the four mapping runs was 30 minutes. At the end of each run, the reactor was lowered and the radiation shielding was removed to allow access to the detectors. In the two runs with the hydrogen-filled tank, the hydrogen was drained from the tank before removal of the shielding. A rather lengthy system warm-up and purge procedure followed before retrieval of the detectors from inside the tank.

3.2 Tank-Wall Nuclear Heating (Runs 2 and 3)

The nuclear energy deposition and the resultant heating of the inner dewar wall was a major contributor to the total heat input into the system. To determine the net nuclear heating in the liquid hydrogen, the heat contribution from the dewar wall had to be determined and subtracted from the total heat input into the system. The rates of temperature rise were measured at five locations on the inside of the tank and at five points on the outside of the tank for each of the two experimental configurations. The installation of the thermocouples on the dewar walls was checked before these runs were started.

The radiation shielding was again replaced, and the reactor was raised to the correct position. The thermocouple-readout recorders were started, and the reactor was brought to power on a 7.5-sec period. The reactor was held at power for 15 min and then scrammed and immediately lowered. Recording of the temperatures continued for about 45 min after the reactor scram

to determine the slope of the heat-loss curve.

3.3 Vaporization and Self-Pressurization (Runs 8-13)

Both the vaporization and self-pressurization runs were made to measure the bulk heat input into the liquid hydrogen. These runs were made without reactor power to determine the nonnuclear heat inputs into the system and with reactor power for each of the two experimental configurations to determine the nuclear heat input for each configuration. The measurements were made with various levels of liquid hydrogen in the tank to determine the heating rates as a function of liquid level.

The platinum resistance thermometers were installed in the tank before the start of this series of runs, and the liquid-hydrogen temperatures were monitored at intervals during the runs. After the dewar was filled and sufficient time allowed for cool-down of the system, the rate of liquid vaporization, or boil-off, was measured by the rate of gas flow through the flowmeter. The heat input into the system could be calculated from this gas flow. The gas-flow rate was monitored for a minimum of 10 min and then the dewar system was valved shut to start the pressurization portion of the run. Pressurization was usually allowed to continue until the tank pressure approached about 45 psia. Again, the heat input could be calculated from the pressure rise in the dewar and the accompanying temperature rise of the liquid hydrogen. In the runs with the reactor at power, the power level was usually not changed at the end of the boil-off measurement and the start of self-pressurization.

In practice, the boil-off runs were not always followed by

self-pressurization runs. This was because boil-off measurements were made at more liquid levels than were self-pressurization measurements and because failure of flowmeter operation required that boil-off measurements be repeated several times.

During the vaporization and self-pressurization runs, attempts were made to determine what fraction of the energy deposited by nuclear radiation in liquid hydrogen is stored temporarily by the disassociation and excitation of H_2 molecules. This was primarily done by observing the boil-off and self-pressurization rates after the reactor was scrammed. In principle, the boil-off and pressurization rates immediately after reactor shutdown are proportional to the ambient heat leak into the system plus the heat produced by energy release of the storage mechanisms. Thus, the difference in boil-off and pressurization measurements made before reactor startup and those made immediately after reactor shutdown can be attributed to energy-storage mechanisms.

3.4 Liquid Flow from Tank (Runs 14-23)

This series of runs was concerned with measurement of the temperature distributions in the liquid hydrogen for different combinations of four parameters: (1) the rate of liquid-hydrogen flow from the tank, (2) the rate of heat input (reactor power), (3) the heating gradient (experimental configuration), and (4) the amount of tank pressurization. Of particular interest was the effect of these parameters on the exit temperature of the liquid hydrogen and the degree of mixing or stratification of the warmed hydrogen in the tank.

The reactor power levels were selected to give the desired temperature increases in the liquid hydrogen during a run and yet prevent boiling of the liquid at the given tank pressurization. The pressure in the tank was held at either 30 or 60 psia during these runs. Hydrogen gas was used in all but two runs as the pressurization gas; mixtures of hydrogen and helium were used in these two. It was desired to maintain the liquid-hydrogen flow from the tank at either 0.04 or 0.12 lb/sec. The two previously described experimental configurations provided the choice of two heating gradients.

The sequence of events for one of these flow runs was as follows:

1. The dewar was filled with LH_2 to a level of 115 to 120 gal.
2. The pressurization gas regulators were checked and set to supply the proper pressure.
3. The reactor was raised to the desired experimental position.
4. All instrumentation recorders were turned on.
5. The reactor was started to power, and pressurization of the tank was started.
6. As the reactor reached full power, the liquid flow valve was opened and flow was started.
7. When the liquid level reached level indicator 1 or thermometers 1 and 2, the reactor was scrammed.
8. The pressurization gas was shut off, and the liquid flow valve was closed.
9. The data recorders were turned off.

The procedure in bringing the reactor to power involved two steps. First, the reactor was brough to one thousandth of the

desired power on a long (approximately 30-sec) period. Then, a 7.5-sec period was used in proceeding to the desired power. Thus, slightly less than one minute was required on the last leg to increase the reactor power by a factor of 1000.

During some of the early flow runs, it was discovered that boiling did take place in the hydrogen just prior to the emptying of the tank. Consequently, the planned reactor powers were decreased for later runs, and tank pressurization was delayed until after the reactor had reached one thousandth of full power for the particular run.

4. RESULTS AND DISCUSSIONS

A summary of the data obtained and the conditions of each experimental run is given in Tables 4.0-1 and 4.0-2. In Table 4.0-1, a special numbering system was required to designate the series of runs under Run 10. Typical data and results from the various types of test runs and calculations are illustrated and discussed in the following sections. The experimental data from Runs 8 through 23 are presented in tabular and graphical form in Volume II of this report.

4.1 Nuclear-Radiation Mapping Data

The nuclear-radiation distributions inside the filled tank are of primary interest and are discussed in some detail. Not only were the heating gradients determined from these distributions, but the data also served as a starting point for calculating the nuclear energy deposited in the liquid hydrogen. In the following discussions, measurements made inside the full ($\sim$45 in.) hydrogen tank are compared with results from calculations made with the C-17 shield-penetration code (Ref. 1). The nuclear data appear in graphical form throughout the text and in tabular form at the end of Section 4 (Tables 4.1-1 through 4.1-8). The methods and assumptions used in the C-17 calculations are presented in Appendix C. Data obtained from measurements made with the tank empty are tabulated in Tables 4.1-5 and 4.1-7 at the end of this section.

4.1.1 Centerline Distributions

4.1.1.1 Neutron Flux

Both measured and calculated fast-neutron fluxes along

Table 4.0-1

Summary of Parametric Conditions for Wall-Heating, Radiation-Mapping, and Boil-Off Runs

Type of Test	Test No.	Reactor Run No.	Reactor Config.	Power Level (Mw)	Run Time (min)	Liquid Level (in.)	Liquid Volume (gal)	Boil-Off Data		Self-Press. Data	Temp Data
								w/o Nuc. Heating (watts)	w/ Nuc. Heating (w/Mw)		
System Checkout	1		Functional Test of Experimental System, No Data								
Wall Heating	2	86	1	1.34	15[a]	0	0				
	3	86	2	2.45	15[a]	0	0				
Radiation Mapping	4	84	1	0.255	30[a]	0	0				
	5	85	2	0.533	30[a]	0	0				
	6	87	1	0.522	30[a]	41.1	110				
	7	88	2	1.06	30[a]	39.4	103.5				
Boil-Off and/or Self-Pressurization	8	--	-	0	124[b]	40.7	108.5			x	x
	8	--	-	0	----	45.7	125.5	26			
	9	--	-	0	140[b]	26.2	58.0			x	x
	9	--	-	0	----	28.3	67.0	22.0			
	10	89	1	0	24[c]	40.7	108.5				x
				1.405	45.3[b]	40.7	108.5			x	x
		94	1	0	----	44.1	120.3	23.8			
	10(8-1)	105	1	1.00	----	43.7	118.5		403		
				1.0 & 2.1	10.9[b] 14.9	43.7	118.5			x	
	10(5-1)	105	1	1.56	----	32.3	79.4		366		
	10(3-1)	105	1	2.00	----	27.4	62.2		331		
	10(7-1)	106	1	1.964	----	18.0	29.7		271		
	10(5-2)	105	2	1.54	----	32.3	79.4		197		
	10(3-2)	105	2	2.05	13[b]	25.3	55.0		186	x	
	10(7-2)	105	2	2.07	----	18.0	29.7		136		
	11	92	1	0	1[c]	16.4	24.4				x
				1.35	37.0[b]	16.4	24.4			x	x
		95		0	----	27.4	62.2	22.3			
	12	90	2	0	40[c]	35.4	89.6				x
				2.807	57[b]	35.4	89.6			x	x
		103		5.725	----	44.7	122		204		
	13	93	2	0	1[c]	27.4	62.2				x
				2.55	43.2[b]	27.4	62.2			x	x
		96		0	----	24.5	52.0	23.3			

[a]Length of reactor time at specified power level

[b]Time from start of self-pressurization to scram or depressurization, whichever was first

[c]Length of data-accumulation time

the vertical centerline of the tank are shown in Figure 4.1-1 for Configuration 1. Fluxes above 2.9 and 8.1 Mev are shown to allow comparison of the calculated and measured fast-neutron spectrum. To obtain the calculated values, the C-17 neutron spectrum was integrated above 2.9 and above 8.1 Mev. Agreement of the fluxes above 2.9 Mev is quite good, while the agreement of the fluxes above 8.1 Mev is fair. Thus, the calculated neutron spectrum of Configuration 1 is in fair agreement with the measurements.

Figure 4.1-2 shows the measured and calculated fast-neutron fluxes for Configuration 2. Again, the agreement of measured and calculated neutron fluxes above 2.9 Mev is good; however, above 8.1 Mev the measured flux is about 30% lower than the calculated flux. In both configurations, the calculated fast-neutron spectra contain more neutrons above 8.1 Mev than the measurements indicate.

The measured thermal-neutron flux distributions along the centerline for Configurations 1 and 2 are shown in Figure 4.1-3. No calculated curves are available for comparison because the neutron-energy cutoff for the C-17 code is 0.33 Mev. These curves represent data derived from gold foils and copper wires.

4.1.1.2 Gamma Dose Rates

Measured and calculated gamma dose rates along the tank centerline are shown in Figures 4.1-4 and 4.1-5 for Configurations 1 and 2, respectively. The contributions of the various calculated components are plotted. The maximum difference between calculated and measured total dose rates for Configuration 1

Table 4.0-2

Summary of Parametric Conditions and Data Obtained for Flow Runs

Test No.	Reactor Run No.	Reactor Config.[a]	Power Level[b] (Mw)	Liquid Volume (gal)	Mean Flow Rate[c] (lb/sec)	Mean Press. (psia)	Temp Rise[c] (^{o}R)
14	97	1	0.711	115.0	0.031	29.5	3.5
14	99	1	0.492	118.5	0.048	28.5	3.4
15	98	1	0.985	118.5	0.052	59.8	5.1
15	110	1	1.043	115.0	0.038	60.0	7.7
16	101	1	0.715	115.0	0.135	59.0	1.1
16	110	1	1.065	115.0	0.134	54.0	1.6
17	108	1	3.00	109.0	0.125	55.0	4.0
18	100	1	0.555	116.5	0.039	29.0	4.2
19	101	2	0.985	111.5	0.055	29.4	2.6
19	110	2	1.092	111.5	0.041	34.3	3.2
20	102	2	2.175	111.5	0.037	57.0	9.6
21	102	2	1.560	115.0	0.101	58.8	1.8
22	109	2	5.72	118.5	0.13	54.0	4.0
23	101	2	2.22	115.0	0.104	27.4	2.7

[a]Heating gradient in LH_2 differed for the two configurations because of differing ratios of neutron/gamma-ray radiation intensities.

[b]Power levels are indicative of relative heating rates.

[c]Over time interval during which effects of transient conditions at beginning and end of test were negligible. See discussions on individual runs in Volume II, Section 4.

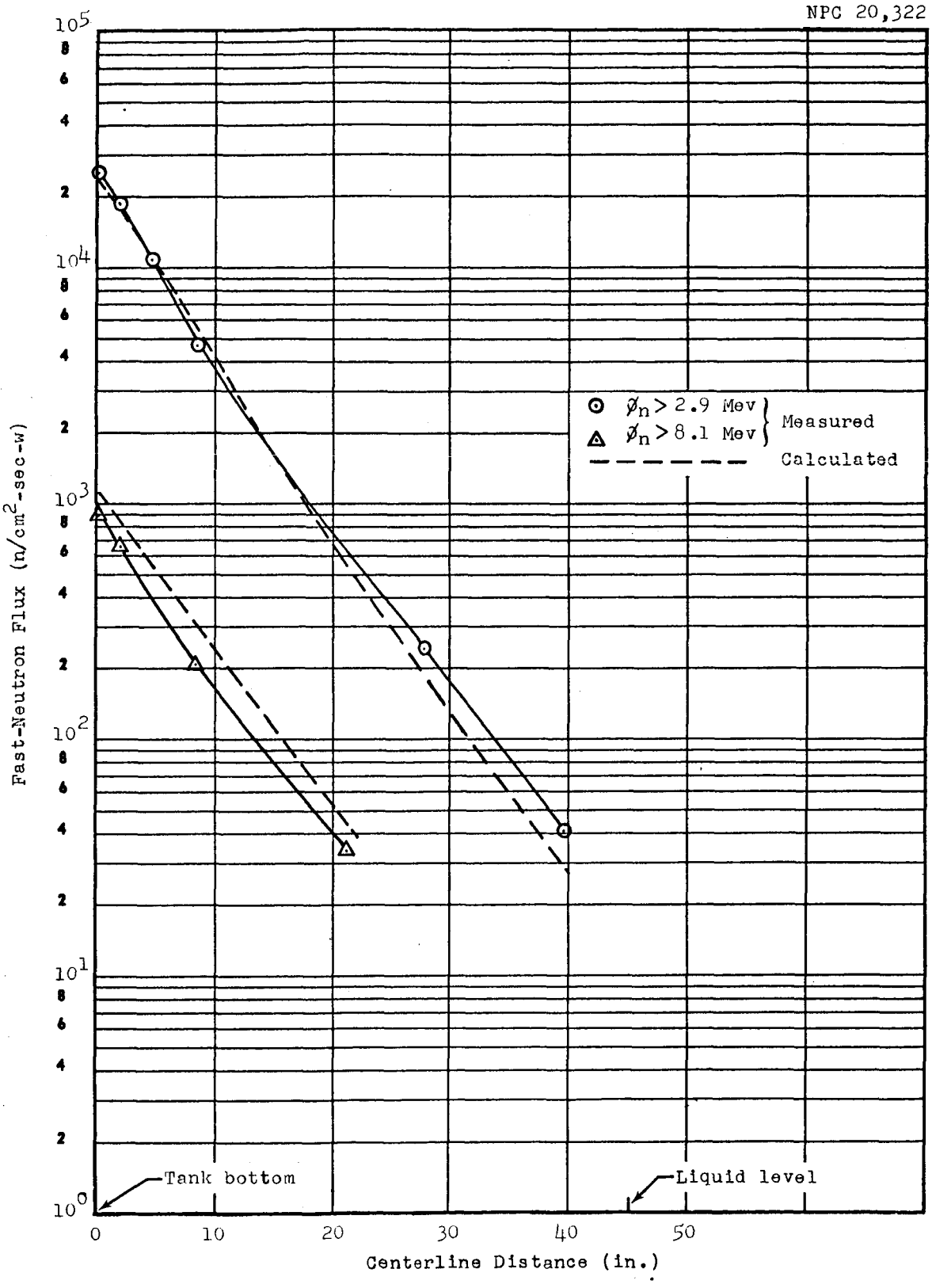

Figure 4.1-1 Fast-Neutron Flux Distribution in LH_2 along Vertical Centerline of Tank: Configuration 1

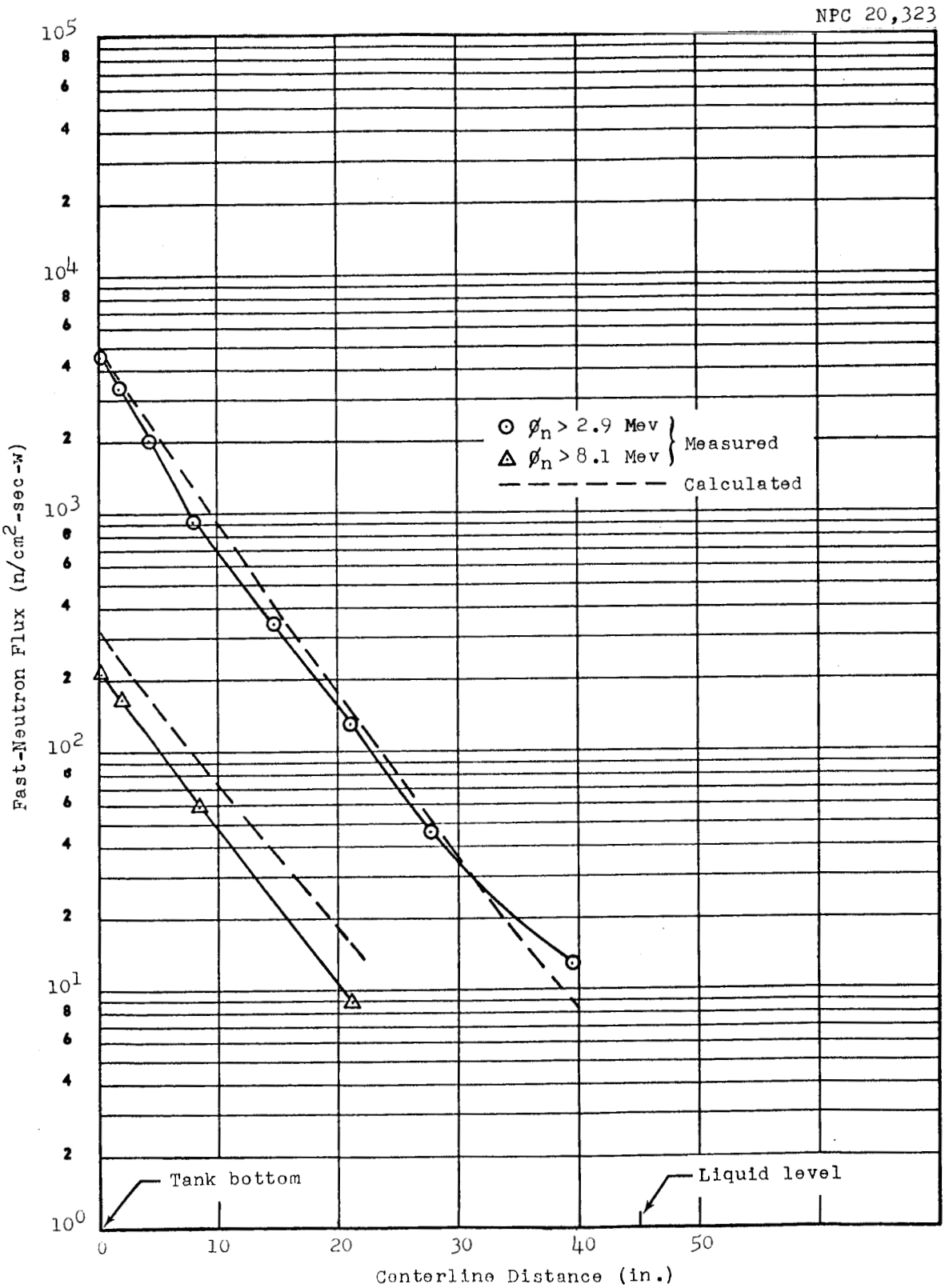

Figure 4.1-2 Fast-Neutron Flux Distribution in LH_2 along Vertical Centerline of Tank: Configuration 2

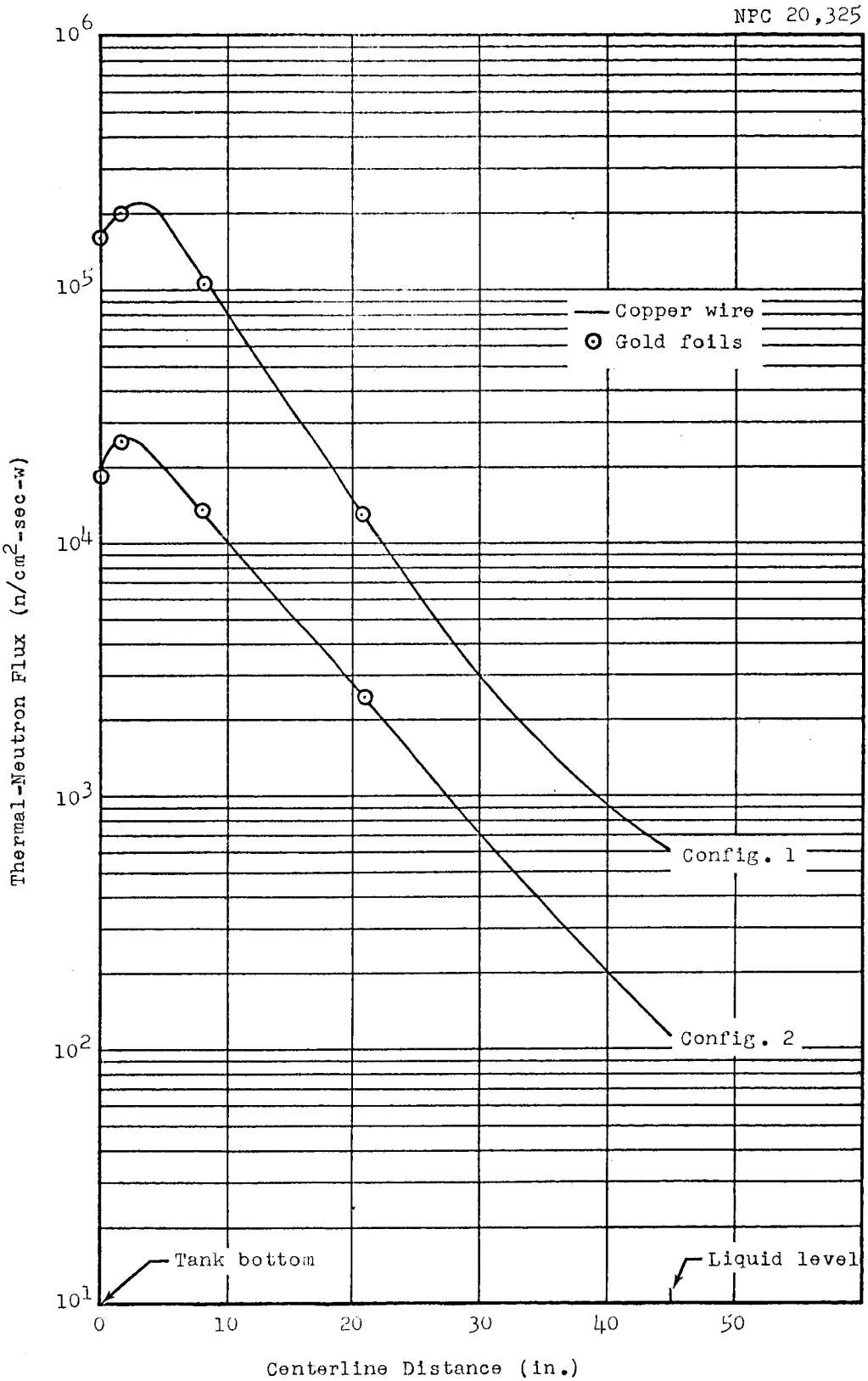

Figure 4.1-3 Thermal-Neutron Flux Distribution in LH_2 along Vertical Centerline of Tank

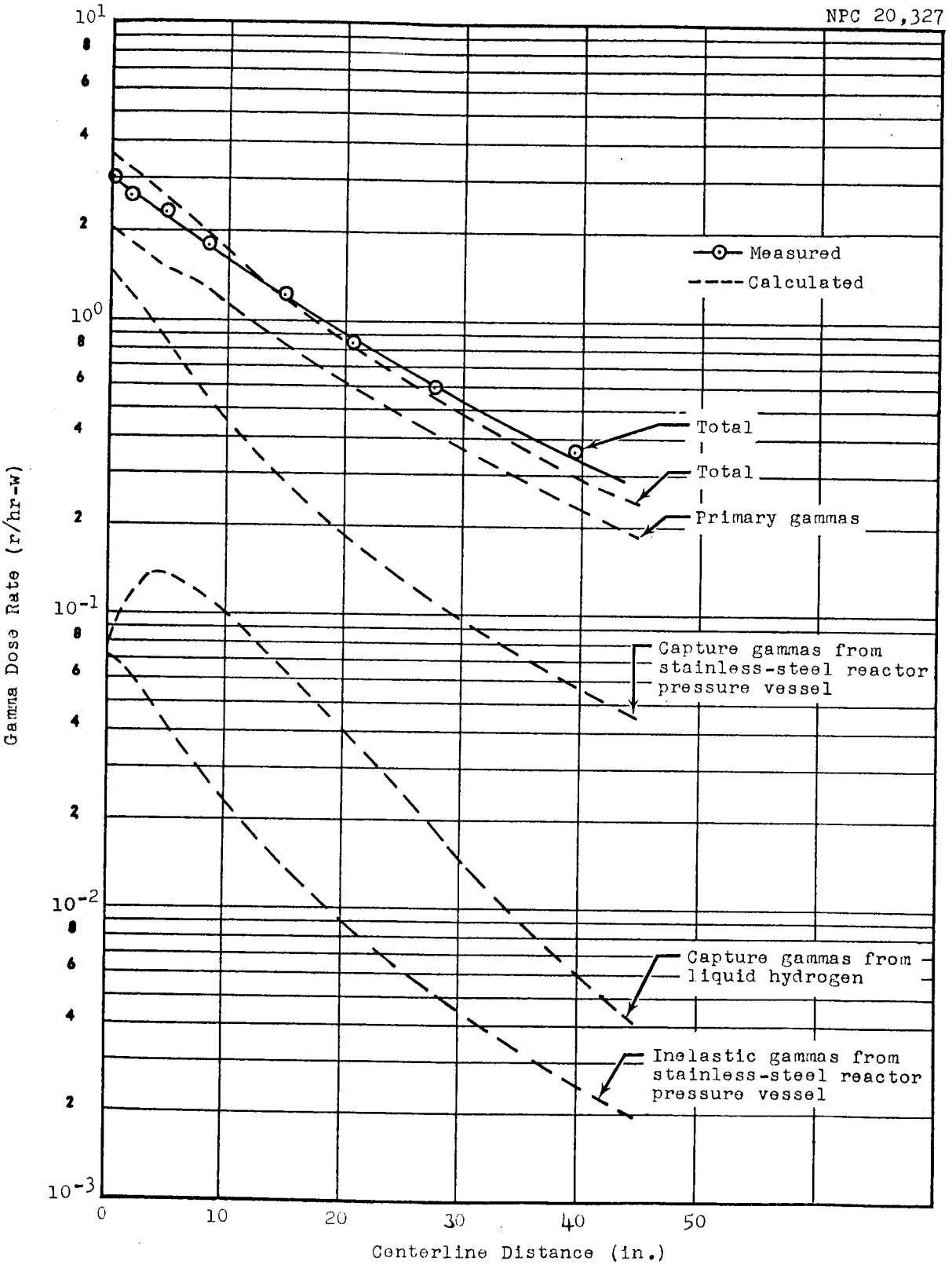

Figure 4.1-4 Gamma Dose-Rate Distribution in LH_2 along Vertical Centerline of Tank: Configuration 1

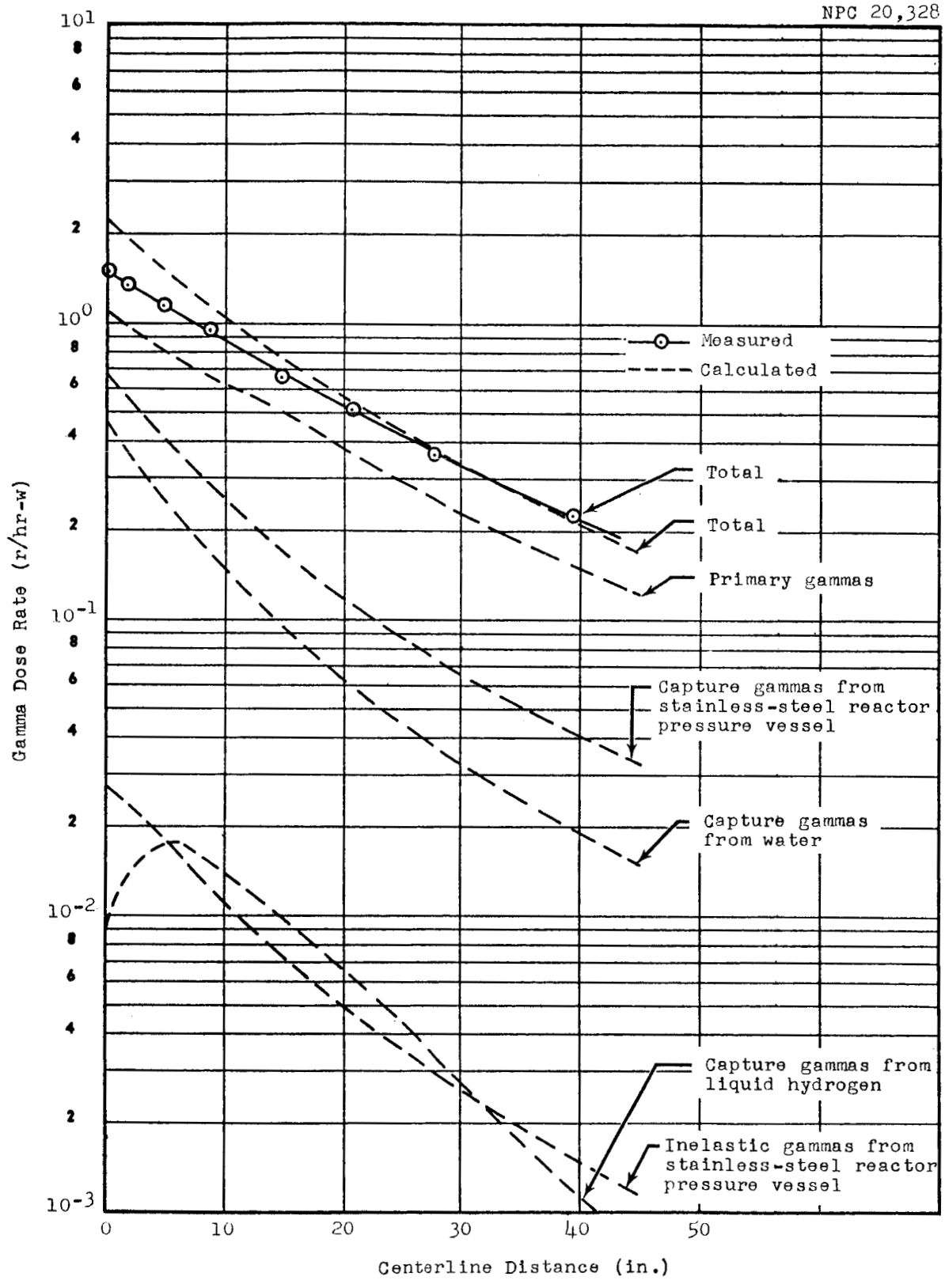

Figure 4.1-5 Gamma Dose-Rate Distribution in LH_2 along Vertical Centerline of Tank: Configuration 2

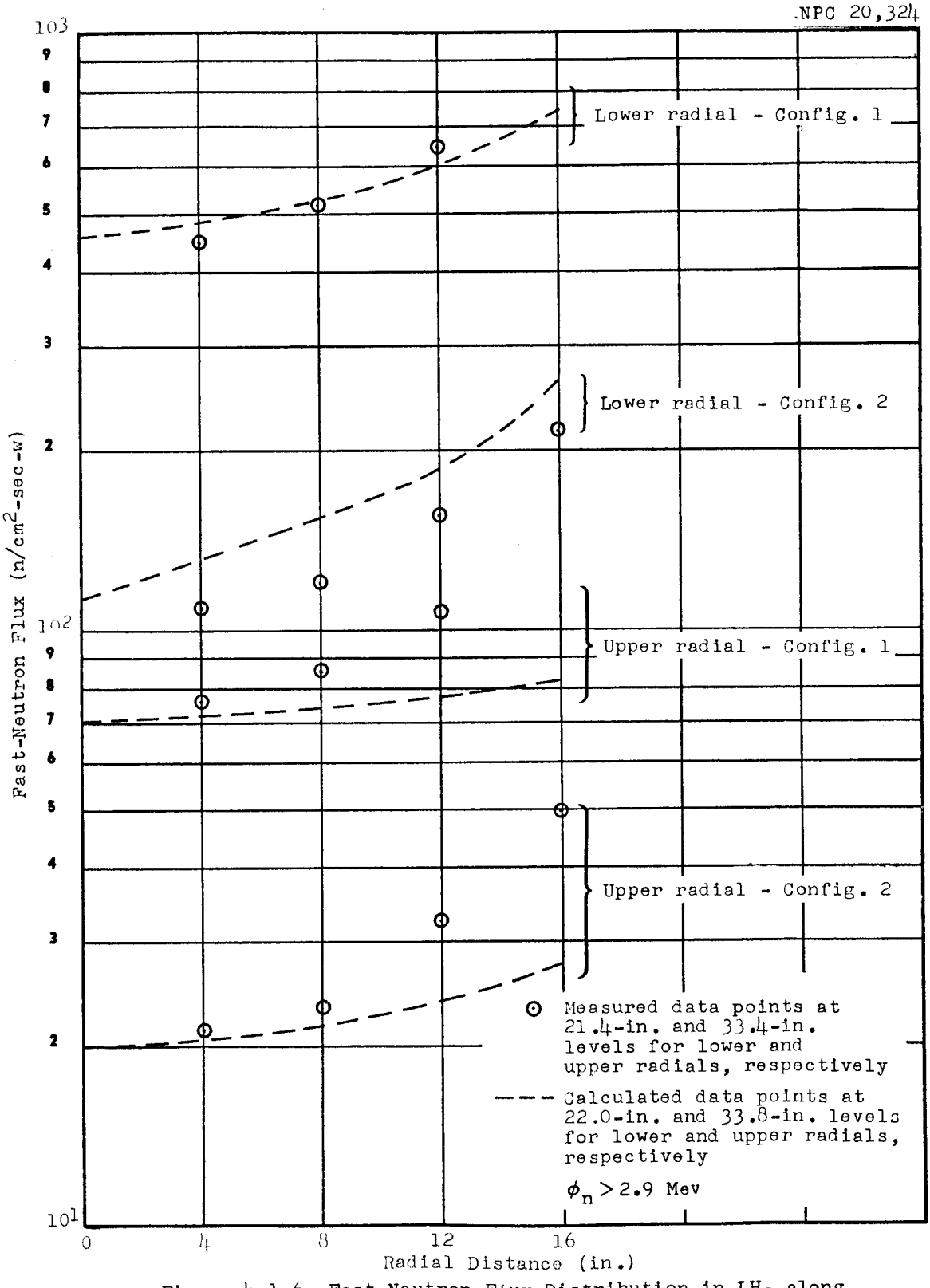

Figure 4.1-6 Fast-Neutron Flux Distribution in LH_2 along Upper and Lower Radials of Tank

is about 20%. The agreement for Configuration 2 is poor over the first few inches of liquid hydrogen, where the calculated dose rates are higher by a maximum difference of approximately 30%.

A comparison of the total gamma dose-rate curves for both configurations shows that the calculated-value curves have a slighthly steeper slope than do the measured-value curves. One possible explanation for this is the limitation of the penetration program in the use of the differential-energy-spectra data. The basic gamma-buildup data are more realistic (and the results are more reliable) when applied to calculating a modified spectrum after penetration of regions or materials of such dimensions as to appear to be infinite. Since the mass of hydrogen in the tank bottom, or conical portion of the tank, is not an infinite region, the calculated dose rates would most probably represent an overestimate of the true gamma dose rate in this vicinity.

4.1.2 Radial Distributions

4.1.2.1 Neutron Flux

The fast-neutron fluxes along the radials from the tank centerline in one vertical plane are shown in Figure 4.1-6. The calculated curves may be compared with the measured values plotted on the figure. Both calculations and measurements indicate that the symmetry of neutron distributions on the radials in x,y- and x,z-planes was quite good; therefore, the distributions in only one plane are discussed.

The C-17 code appears to predict the magnitude rather well where the scattered-neutron component is small, but the large differences on the upper radials of both Configurations 1 and 2

near the outer periphery of the tank are probably caused by neutrons scattering into the hydrogen from outside the hydrogen tank.

The measured thermal fluxes obtained with copper wire along the radials are shown in Figure 4.1-7; the measurements were normalized to gold-foil values. The decrease of thermal flux towards the tank wall is assumed to be due to absorption of thermal neutrons in the hydrogen-tank and liner-tank walls.

4.1.2.2 Gamma Dose Rates

As in the case of neutrons, the symmetry of gamma-ray distributions about the tank centerline was very good. The plots of the radial gamma-dose-rate distributions measured and calculated at two levels in the x,y-plane are shown in Figures 4.1-8 and 4.1-9. The discrepancy between calculated and measured dose rates near the tank wall in Configuration 1 indicates a possible capture component in the walls of the tank or the surrounding water medium. Since the agreement is better near the centerline, such a capture component must be in the low-energy range in order to be attenuated so rapidly by the hydrogen. This effect is not discernible for Configuration 2 because the neutron-to-gamma ratio is lower and the primary gamma component apparently overshadows the secondary component, which is lower for Configuration 2.

4.1.3 Measurements Outside of Tank

The nuclear-radiation measurements made on the outside surface of the dewar did not provide data essential in determining the heat input into the system, but they helped in checking the nuclear characteristics of the system. These measurements

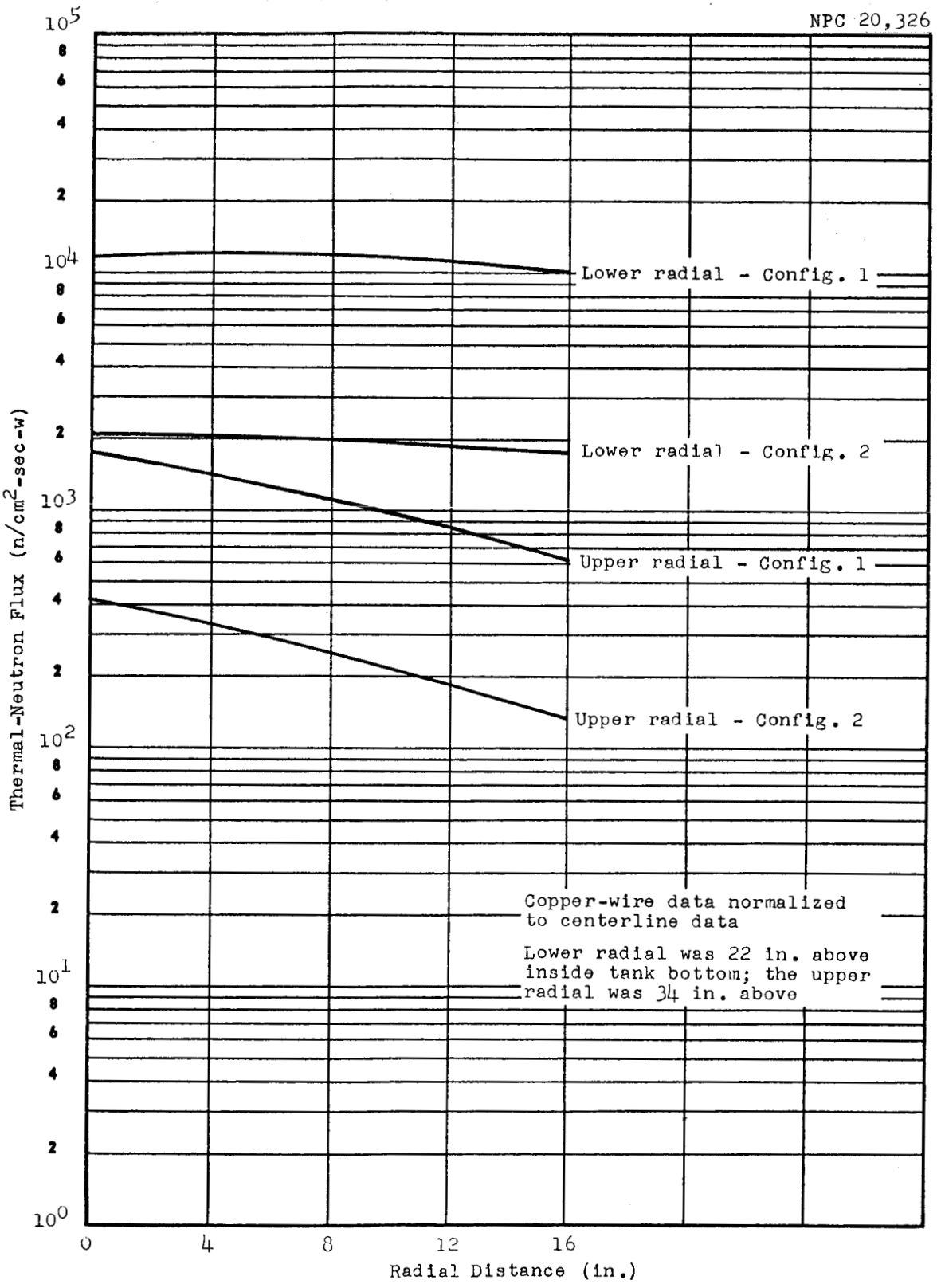

Figure 4.1-7 Thermal-Neutron Flux Distribution in LH_2 along Upper and Lower Radials of Tank

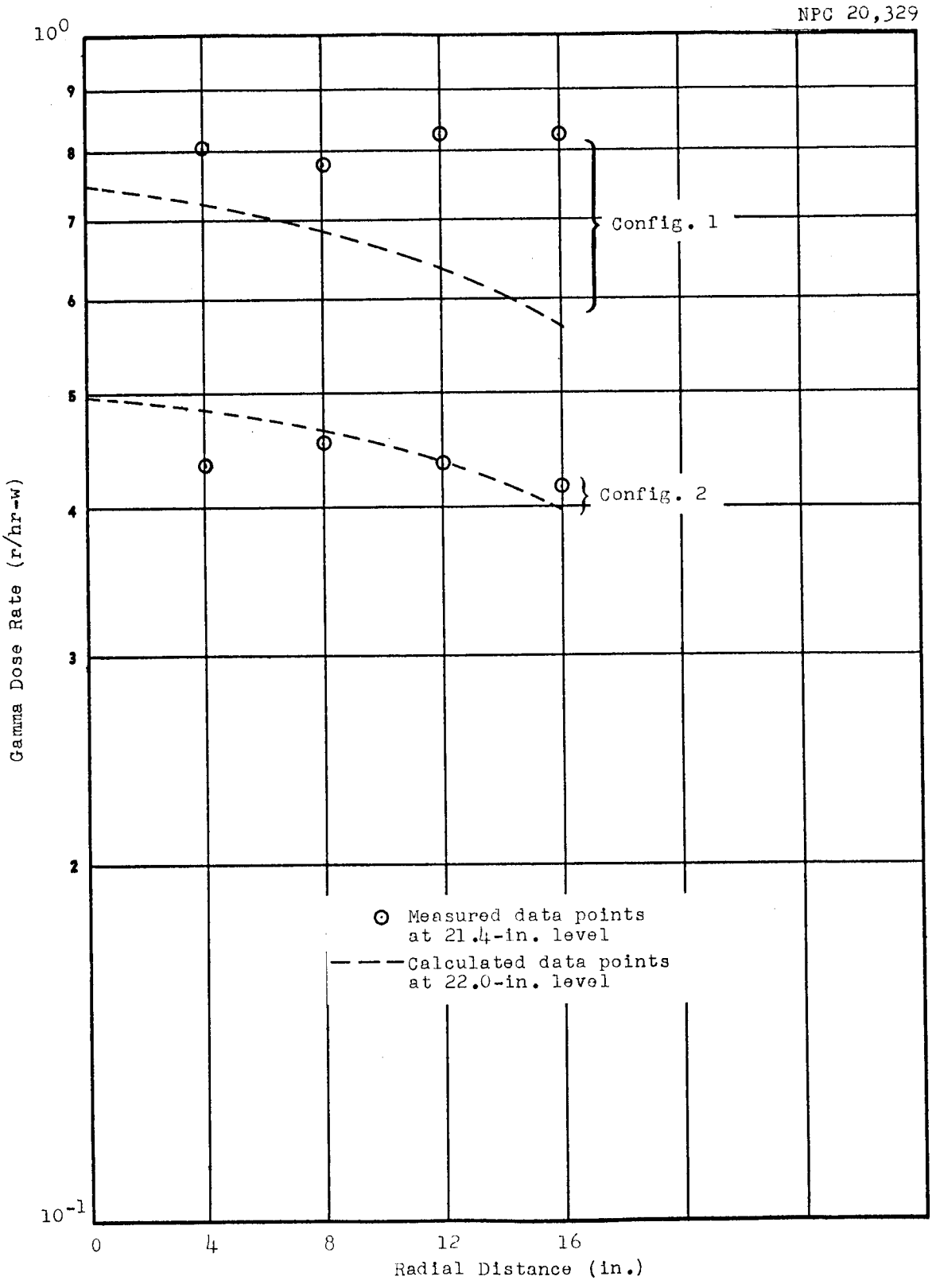

Figure 4.1-8 Total Gamma Dose-Rate Distribution in LH_2 along Lower Radial of Tank

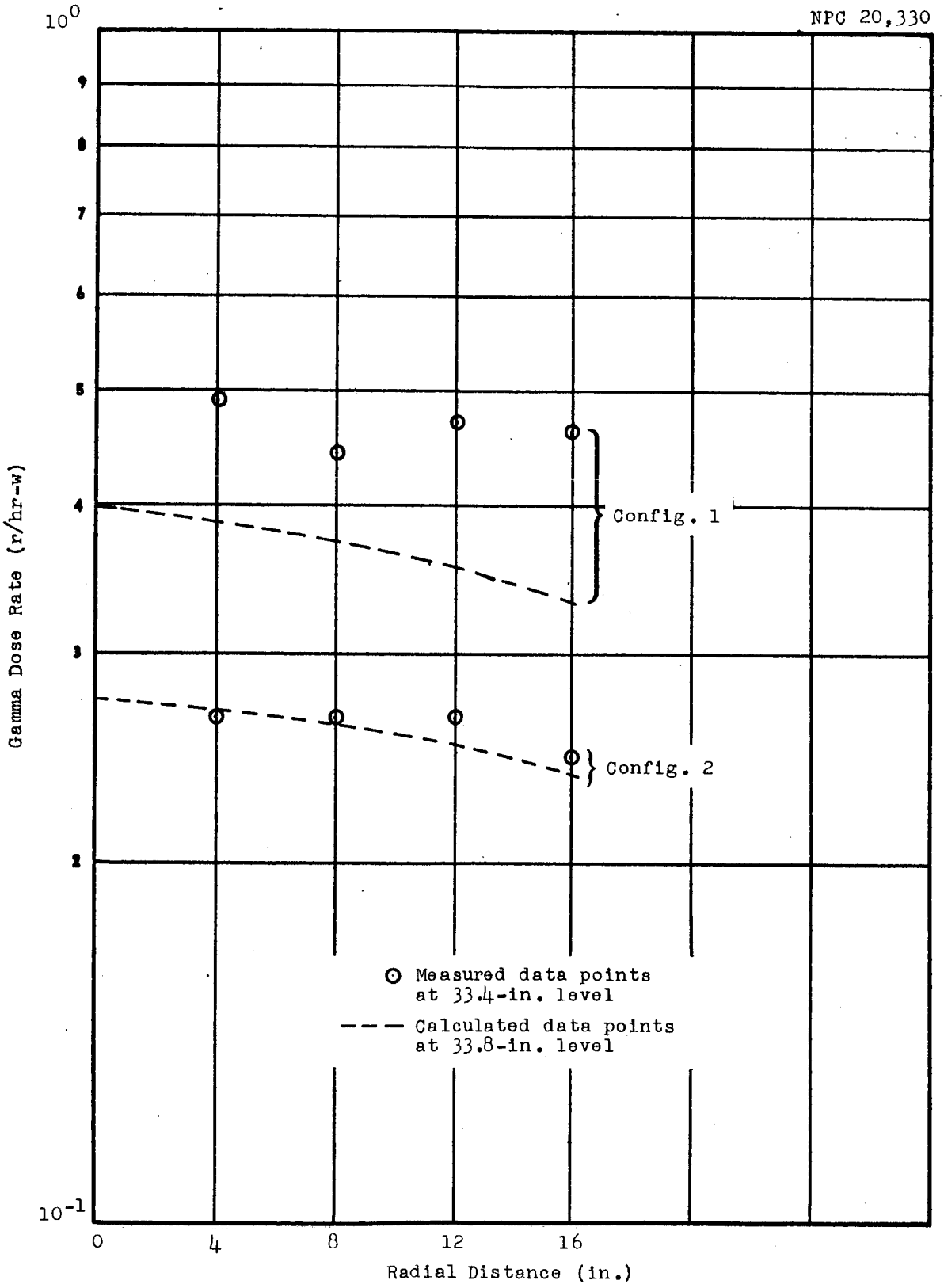

Figure 4.1-9 Total Gamma Dose-Rate Distribution in LH_2 along Upper Radial of Tank

indicate that the thermal-neutron leakage through the liner tank was small, thus keeping the activation and capture-gamma production in the dewar walls low. It was also interesting to note that the measured neutron flux and gamma dose rate at the bottom did not change significantly when the dewar was filled with hydrogen. This indicates that the hydrogen-capture gamma component was of little significance at this position and the thermal-neutron leakage from the dewar in this direction was small.

4.2 Nuclear-Radiation Heating in Tank Wall

The rates of gamma-ray energy deposition in the inner wall of the hydrogen-filled dewar for Configurations 1 and 2 have been calculated from C-17 results with corrections based on measured dose-rate data. A demonstration of the validity of this method is given by using it to predict the observed rate of temperature rise at points on the inner wall of the empty dewar, taking into account heat conduction along the wall and leakage into the air inside the dewar. Only energy deposition from gamma-rays was considered because the neutron contribution was less than 1%.

4.2.1 Calculations for Hydrogen-Filled Tank

The energy-deposition rate at points on the wall were calculated by multiplying the energy-deposition rates interpolated from C-17 data by the ratio of the (interpolated) measured dose rates to the corresponding (interpolated)C-17 dose rate. Letting

$\dot{h}$ = actual energy-deposition rate at a point in the wall,

$\dot{h}'$ = energy-deposition rate interpolated from C-17 results,

D_m = gamma dose rate interpolated from measurements at inside surface of inner wall, and

D_c = gamma dose rate interpolated from C-17 calculations,

it was assumed that

$$\dot{h} = (D_m/D_c)\dot{h}'.$$

Since the thickness of the wall is of the order of 0.07 in., it was assumed that both the dose rate and the heating rate were uniform along a normal through the inner wall.

The use of the above equation is based on an assumed proportionality between dose rate and energy flux; it does not consider the spectral effects and boundary perturbations.

The centerline of the dewar was divided into 0.787-in. intervals, and the volumes of the corresponding segments of the inner wall were calculated from design drawings. The rate of heat deposition in each segment was taken to be

$$\dot{h}\Delta V = (D_m/D_c)\dot{h}'\Delta V,$$

where ΔV is the volume of the segment. The geometry of the inner wall was described in terms of five sections: (1) hemispherical, (2) conical, (3) parabolic, (4) cylindrical, and (5) top. The "top" section consisted of the covering and neck of the inner wall, no part of which was in contact with the liquid. The calculated rate of energy deposition in each of the five sections and the total deposition in the wall for Configurations 1 and 2 are given on the following page.

Section	x Range (in.)	Energy Deposition Rate (watts/Mw) Configuration 1	Configuration 2
Hemispherical	(0-1.18)	2.65	1.17
Conical	(1.18-10.6)	27.38	16.16
Parabolic	(10.6-20)	21.43	13.49
Cylindrical	(20-49)	30.84	18.04
Top	(49-61)	6.40	4.14
Total Deposition Rate		88.70	53.00

4.2.2 Comparison of Predicted and Observed Rates of Temperature Rise

By use of the gamma dose rates measured on the empty tank during the radiation-mapping run and of the corresponding C-17 data, the rate of temperature rise for Configuration 1 was estimated. The heat conduction along the wall was calculated from interpolated heating gradients, and the leakage into the air was calculated from empirical relationships. Letting

$\dot{h}$ = the actual energy-deposition rate at a point in the wall,

$\dot{Q}$ = the net rate of heat increase per unit volume due to conduction,

$\dot{\ell}_c$ = the conductive and convective leakage per unit area into the air inside the dewar, and

$\dot{\ell}_r$ = the net radiative emission per unit area,

the rate of temperature rise at a point on a shell of thickness, τ is

$$\dot{T} = \left[\dot{h} + \dot{Q} + (\dot{\ell}_c/\tau) + (\dot{\ell}_r/\tau)\right]/\rho C_p,$$

where ρ is the density and C_p is the specific heat of the metal.

The energy deposition $\dot{h}$ is computed by use of a C-17 prediction corrected by measured dose-rate data.

The heat-flow vector at a point in the metal is

$$\left(\sigma \frac{\partial T}{\partial x}\bar{i} + \sigma \frac{\partial T}{\partial y}\bar{j} + \sigma \frac{\partial T}{\partial z}\bar{k}\right) = \sigma\bar{\nabla}T,$$

where σ is the thermal conductivity. The net heat change per unit volume is

$$\dot{Q} = \bar{\nabla}\cdot \sigma\bar{\nabla}T = \sigma\bar{\nabla}^2T .$$

Using spherical coordinates with r replaced by s,

$$\nabla^2 = \frac{\partial^2}{\partial s^2} + \frac{2}{s}\frac{\partial}{\partial s} + \frac{1}{s^2\sin\theta}\frac{\partial}{\partial\theta}(\sin\theta\,\partial) + \frac{1}{s^2\sin^2\theta}\frac{\partial^2}{\partial\phi^2}$$

where $\bar{s}$ is the position vector of a point with respect to the apex of the conical section. For the conical part of the shell, $\frac{\partial^2 T}{\partial\phi^2} = 0$ from symmetry and, if it is assumed that the temperature gradient along a normal through the shell is negligible, $\frac{\partial T}{\partial\theta} = 0$. Then, for the conical and cylinderical portions of the shell, the net heat loss per unit volume is

$$\dot{Q} = \sigma\left[\frac{\partial^2 T}{\partial s^2} + \frac{2}{s}\frac{\partial T}{\partial s}\right] \qquad \underline{\text{conical}}$$

$$\dot{Q} = \sigma\left[\frac{\partial^2 T}{\partial x^2}\right] \qquad \underline{\text{cylindrical}}$$

The conductive and convective heating was roughly accounted

for by the use of empirical engineering formulas (Ref. 2). For a shell of thickness τ cooling on one side only (the insulation is assumed to completely eliminate heat flow outward), the conductive and convective leakage is given by the following equation (an empirical formula for the cooling of vertical plates):

$$\dot{\ell}_c = \frac{-1}{\tau} (1.3627 \times 10^{-4}) (0.19)(\Delta T)^{1/3} \Delta T ,$$

where $\dot{\ell}_c$ is in cal/cm^3-sec with τ in cm and ΔT the temperature difference in ^oF between the metal and air.

An overestimate of the net loss of heat per cubic centimeter to cooler parts of the dewar by means of radiative emission and absorption is given by (Ref. 3):

$$\dot{\ell}_r = -(1.35 \times 10^{-12}) K(T^4 - T_c^4)/\tau ,$$

where

$$K = \epsilon^2 / \left[1-(1-\epsilon)^2\right]$$

with ϵ the emissivity of the metal. T is the temperature at the point of interest, and T_c is the coldest part of the inner wall. This overestimate of $\dot{\ell}_r$ is expected to be small compared to $\dot{\ell}_c$.

The temperature of the inner wall of the empty dewar was recorded for Configuration 1 at points corresponding to x = 1.75 in., x = 15 in., and x = 27 in. The first of these points was on the conical portion, which had an apex at x = 2.04 in. The second point was on the parabolic section and, for the purpose of calculating $\nabla^2 T$, was regarded as lying on a conical surface with an apex at x = 23.9 in. The third point was on the cylindrical sec-

tion, so that $\nabla^2 T = \partial^2 T/\partial x^2$. The record of these three temperature measurements is shown in Figure 4.2-1.

The three levels where the temperature was recorded were so for apart that a smooth curve drawn through the three temperature values (using certain inferences from dose-rate data) at a given time after startup gave only an order of magnitude estimate of $\partial^2 T/\partial s^2$, $\partial T/\partial s$, and $\partial^2 T/\partial x^2$. Moreover, the empirical leakage formula may not apply well to a surface with the shape and dimensions of the dewar walls. This means that the best to be expected in a prediction of $\dot{T}$ is that the $\dot{Q}$ and $\dot{\ell}_c$ contributions will be of the right order of magnitude to account for the discrepancy between the calculated contribution from $\dot{h}$ and the observed rate of temperature rise.

The calculated contribution to $\dot{T}$ from the several heating (or cooling) components for each of the three positions, together with the predicted and recorded values of $\dot{T}$ at five minutes after startup is given below.

Rate of Temperature Change
($^{\circ}$R/sec)

Position x(in.)	Calculated					Observed
	$\dot{h}/C_p$	$\dot{\ell}_c/\tau\rho C_p$	$\dot{\ell}_r/\tau\rho C_p$	$\dot{Q}/\rho C_p$	$\dot{T}$	$\dot{T}$
1.75	4.8(-2)	-.79(-2)	<-.009(-2)	-.92(02)	3.10(-2)	3.33(-2)
15.00	1.58(-2)	-.14(-2)	<-.009(-2)	-.036(-2)	1.40(-2)	1.08(-2)
27.00	1.15(-2)	-.07(-2)	<-.009(-2)	0	1.08(-2)	0.76(-2)

It is seen that the "correction" for heat flow along the wall for radiative emission, and for conductive and convective cooling

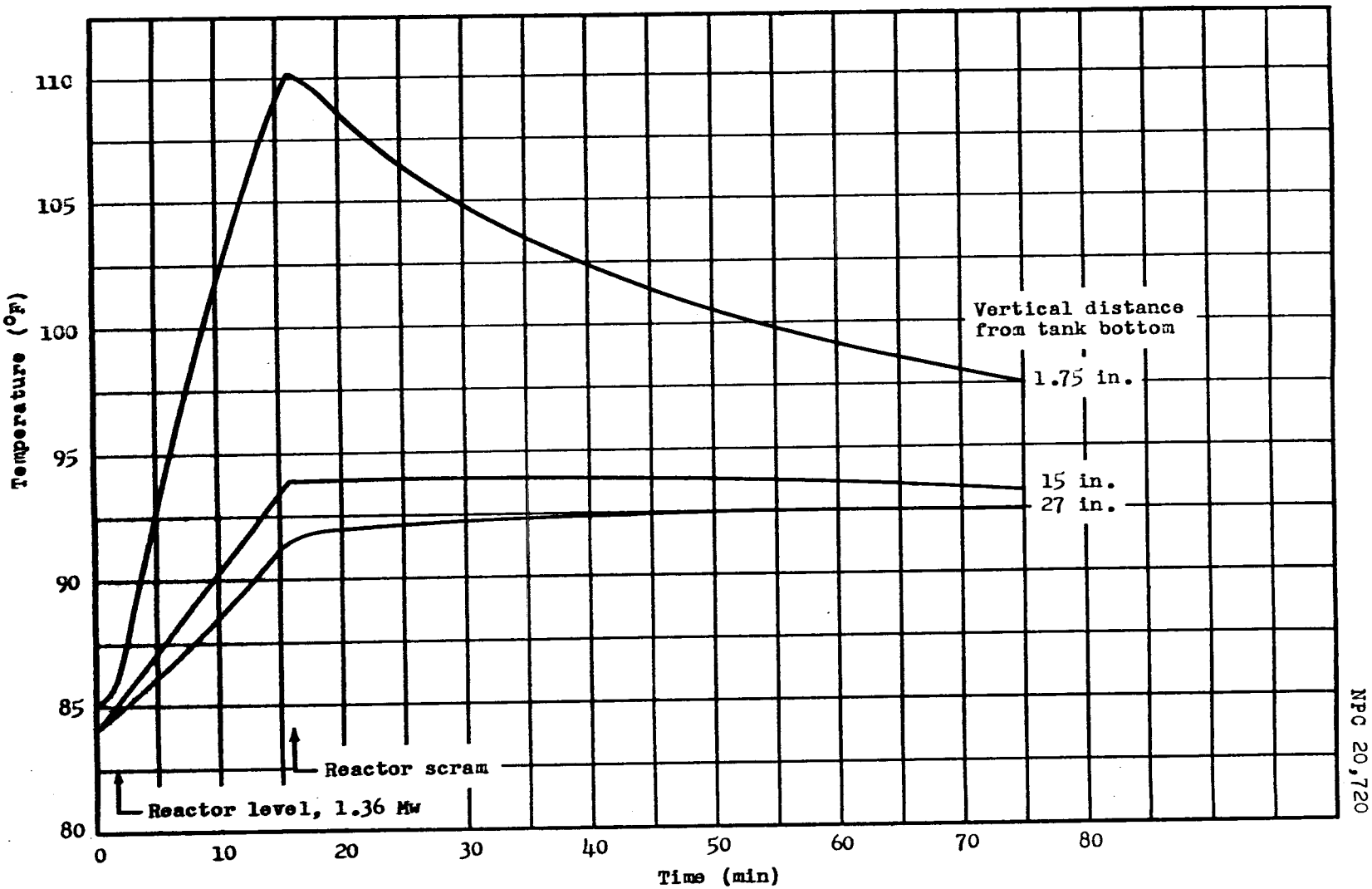

Figure 4.2-1 Tank Wall Temperature Measurements: Configuration 1

was of the right order to explain the difference between $\dot{h}/\rho C_p$ and the observed rate of temperature rise. However, the predicted $\dot{T}$ is progressively higher for larger values of x. The explanation for this effect could be that the calculated gamma spectrum contains more low-energy gammas than the true spectrum. The infinite-medium C-17 method effectively calculates a local flux of low-energy build-up gammas which, because of leakage, would not actually be produced in a thin shell.

In addition, it is conceivable that the escape of recoil electrons from the thin inner wall of the dewar might lead to an appreciable error in the C-17 calculations - which are based on the assumption that Compton-scattered electrons are absorbed practically at the point of scattering. The range of a 2-Mev Compton-scattered electron in metal is about 1.0 gm/cm^2 (Ref. 4), or about 0.051 in. for steel. Since the average distance to the boundary for points inside the lower part of the inner shell is only about 0.0315 in., it is possible that an appreciable fraction of scattered electrons left the shell. It is doubtful, however, that much radiation energy left the shell in this fashion.

On the basis of the predictions of temperature rise in the empty dewar, it is concluded that the overall heating rates for the filled dewar are in error by no more than about 25%. This follows from the consideration that spectral discrepancies due to hydrogen-capture gamma rays and flux perturbations at the liquid-hydrogen boundary should not be as great as those associated with the non-existence of low-energy build-up gammas in the dewar wall. The good agreement between the predicted and observed

values of $\dot{T}$ near the bottom of the dewar shows that the effect of electron leakage is not significant.

4.3 Nuclear-Radiation Heating in Liquid Hydrogen

The heat input into the liquid hydrogen is the basis for analysis of the flow runs; thus, several methods were used to determine the heating rates. For comparative purposes, the heating rates were determined from the following bases:

1. Measured hydrogen vaporization rates (boil-off).
2. Measured temperature rise during self-pressurization.
3. Measured radiation distribution and calculated energy deposition.
4. Calculated radiation distributions and calculated energy depositions.

The methods used and the results obtained for each of these determinations are described in subsections 4.3.1 through 4.3.4 The results are compared in subsection 4.3.5.

4.3.1 Heating Rates Calculated from Boil-Off Rates

The liquid-hydrogen vaporization or boil-off rates were measured as described in the procedures (Sec. 3.3). There is a rather large uncertainty in the accuracy of these measurements because it was discovered during the post-test calibration check of the flow-measuring system that the microswitch readout system on the flowmeter varied the readings of the meter. The microswitch imposed a load on the flowmeter measuring mechanism and thereby changed the meter calibration. Based on initial and post-test calibrations, measurement accuracy in terms of the measured parameter - that is, cubic feet of evolved hydrogen

gas - was ±17% of the measurement. Overall accuracy of the heat values (considering possible errors in reactor power level, gas temperature and pressure measurements, and conversion factors) is estimated to be ±25% of the calculated value. The boil-off data and resultant heating rates are given in Table 4.3-1 and are presented graphically in Figure 4.3-1. The figure indicates that the measurements were consistent, although the possible absolute error was large. The ambient heat leak (zero reactor power) was less than 10% of the total heating rate on all the boil-off runs.

4.3.2 Heating Rates Calculated from Pressurization-Temperature Data

Heating rates were calculated for the nine runs during which the system was allowed to self-pressurize. Two of these runs were made without reactor power to determine the ambient heat leak. The heating rates were calculated by use of the temperature data rather than the pressure data because the temperature was measured with a greater degree of accuracy. The calculations were made with a simplified relationship

$$\frac{\Delta q}{\Delta t} = Q = w(t) \cdot C(T) \cdot \frac{\Delta T}{\Delta t},$$

where

q = energy,

t = time,

Q = energy per unit time,

$w(t)$ = weight of liquid hydrogen as a function of time, and

$C(T)$ = specific heat as a function of temperature T.

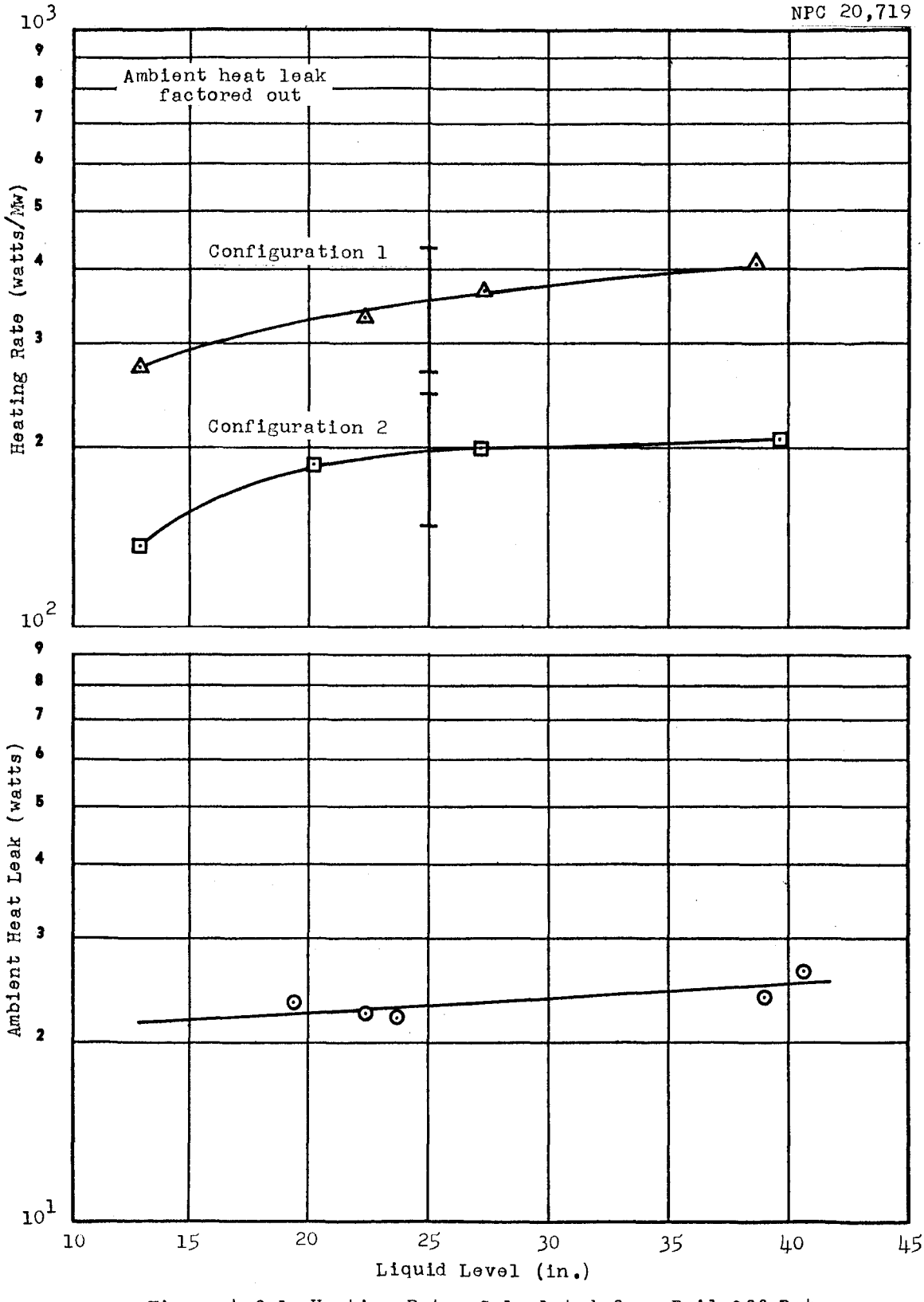

Figure 4.3-1 Heating Rates Calculated from Boil-Off Data

In these calculations, w(t) was assumed to be constant, since a level change did not occur within measurable limits during the self-pressurization portions of the runs. As an approximation, equilibrium conditions were assumed and values of the specific heat of liquid hydrogen under saturated vapor pressure, $C_s(T)$, were used. (The $C_s(T)$ data used are given in Reference 5.) Results of these calculations are given in Table 4.3-2, as are the time and temperature intervals considered and the averaged specific-heat values used in the calculations. The temperature data from Runs 10(3-2)-105 and 10(8-1)-105 that were used in this analysis were processed manually and are not reported elsewhere in the report.

The results given in Table 4.3-2 are presented graphically in Figure 4.3-2. The values for the ambient heat leak were interpolated from the available two data points for most of the runs and were used in arriving at the heat input per magawatt of reactor power.

The calculations did not constitute a rigorous heat-balance analysis, since this approach did not consider possible mass transfer between the liquid and gas phases and included only the secondary effects of heat added to the gas and work done in the system. The results are, however, indicative of the lower limits of the heating rates and serve as a basis for comparison with the heating rates determined by other methods.

4.3.3 Heating Rates Calculated from Measured and Calculated Nuclear-Radiation Distributions

Heating rates in the liquid hydrogen were calculated with

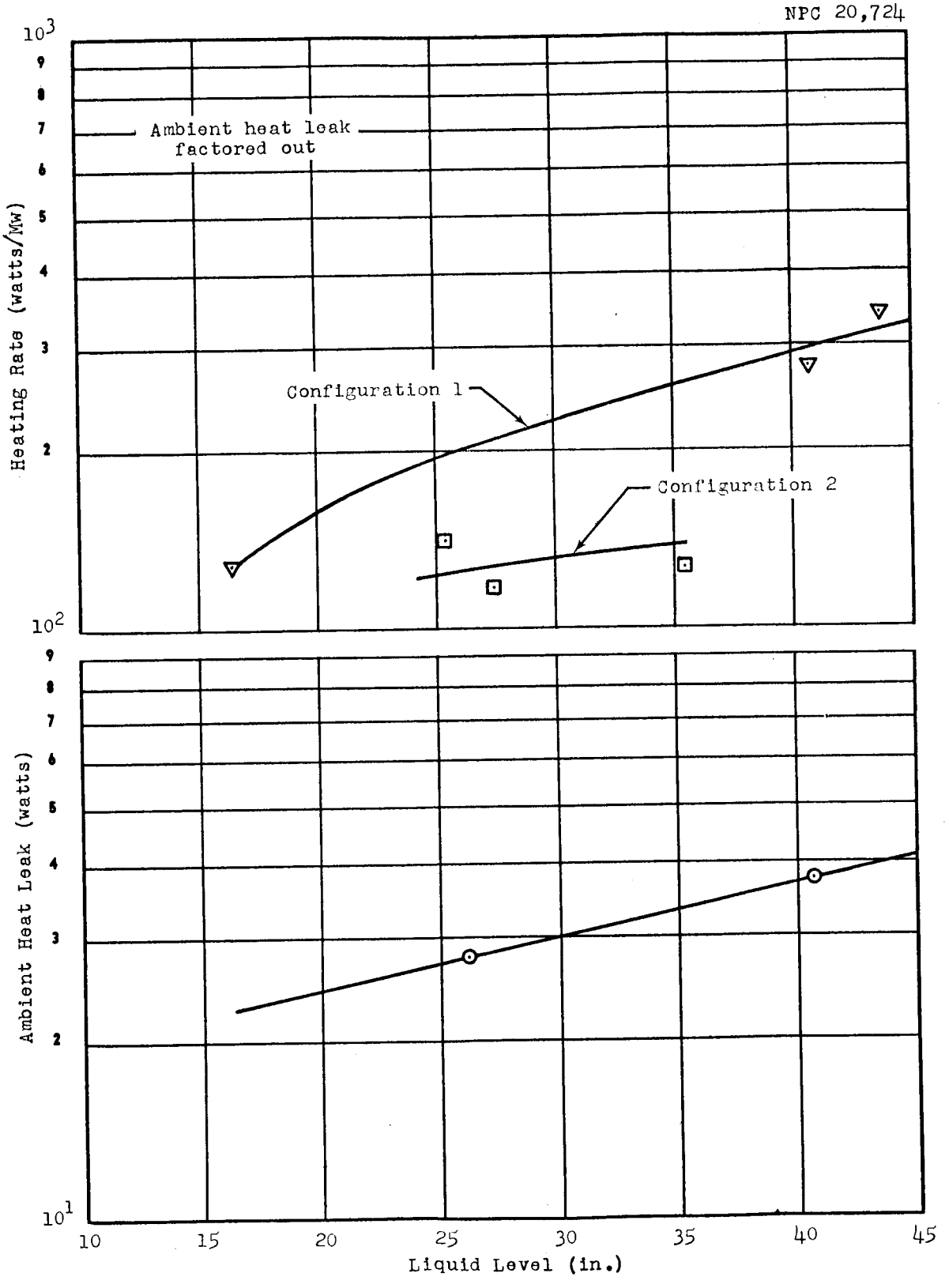

Figure 4.3-2 Heating Rates Calculated from Pressurization-Temperature Data

the C-17 procedure using the measured and C-17 calculated radiation distributions discussed in Section 4.1. These procedures yeilded the energy deposition rates caused by fast-neutron and gamma-ray interactions in the liquid hydrogen. The semi-empirical data on nuclear-radiation heating in the tank wall was combined with the liquid-hydrogen heating data to arrive at total heating rates comparable to those determined by the other methods.

The heating rates calculated on the basis of calculated radiation distributions for Configurations 1 and 2 are presented graphically in Figures 4.3-3 and 4.3-4, respectively. These figures show, as a function of liquid level, the total heating rate, the heating rates caused by gammas and fast neutrons, and the wall-heating component. The results of the heating calculations based on measured nuclear-radiation distributions are not shown graphically, since the results are almost identical.

4.3.4 Heating Rates Calculated by COHORT

The principal purpose of the calculations performed with the relatively new COHORT (Ref. 6) codes was to check the procedures by running a test problem and comparing the results with experimental data and with the results of C-17 calculations. The Configuration 1 geometry was used for the COHORT calculation. The assumptions and methods used in performing the calculations are discussed in Appendix C.

The nuclear-energy deposition rates in the liquid hydrogen at seven different levels were calculated by dividing the hydrogen into seven different regions. The calculated neutron and gamma

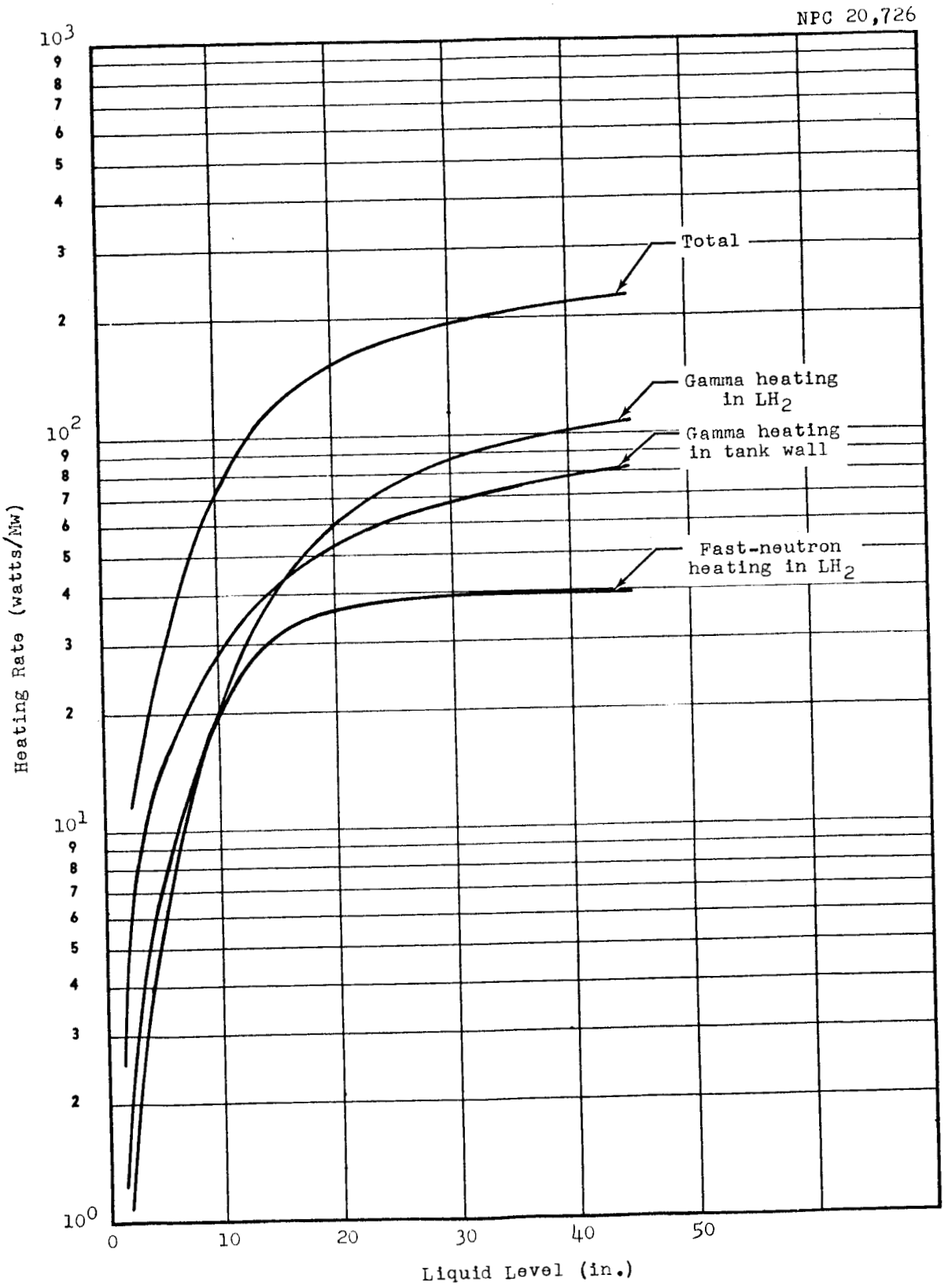

Figure 4.3-3 C-17 Calculated Nuclear-Radiation Heating Rates: Configuration 1

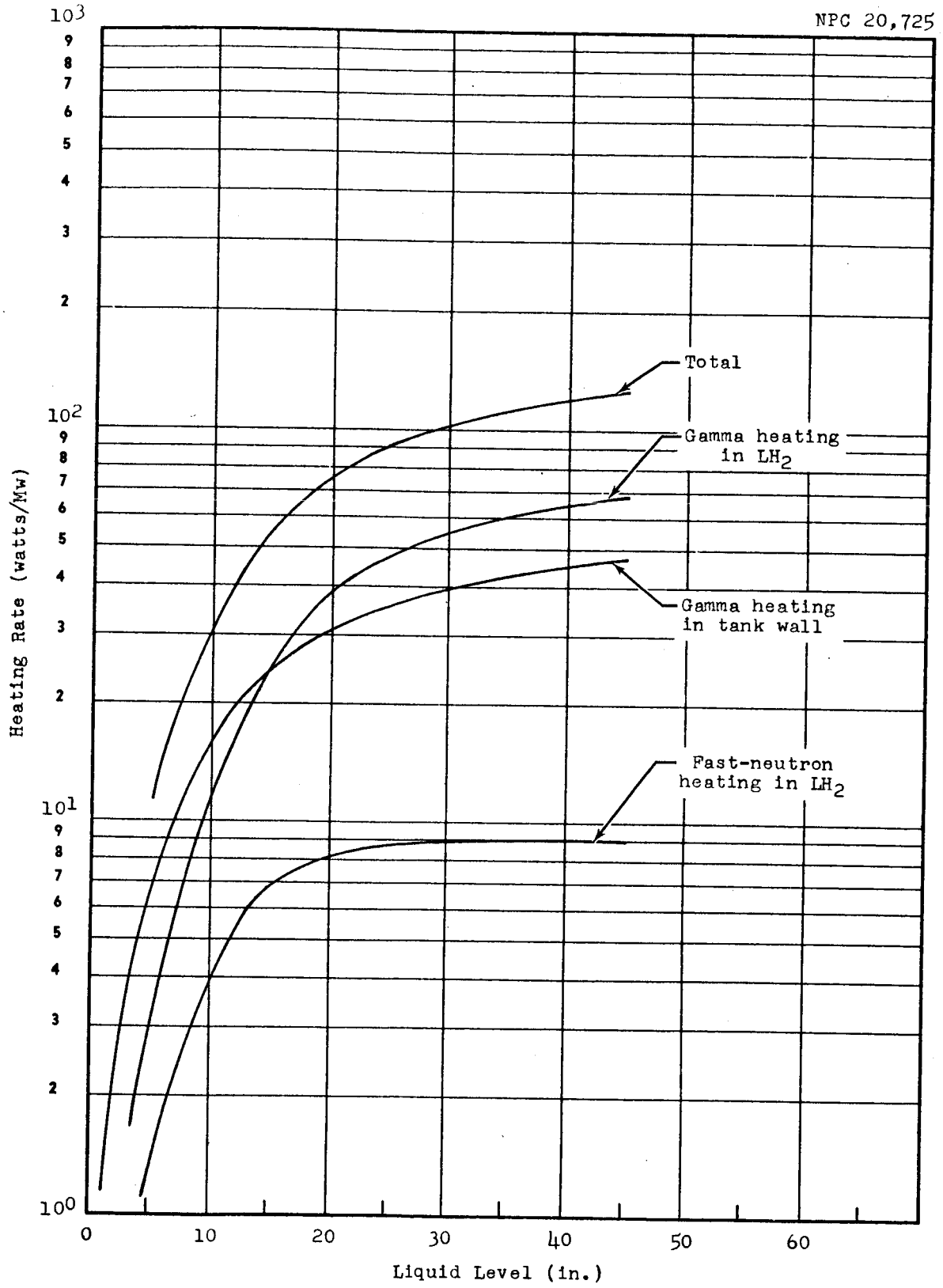

Figure 4.3-4 C-17 Calculated Nuclear-Radiation Heating Rates: Configuration 2

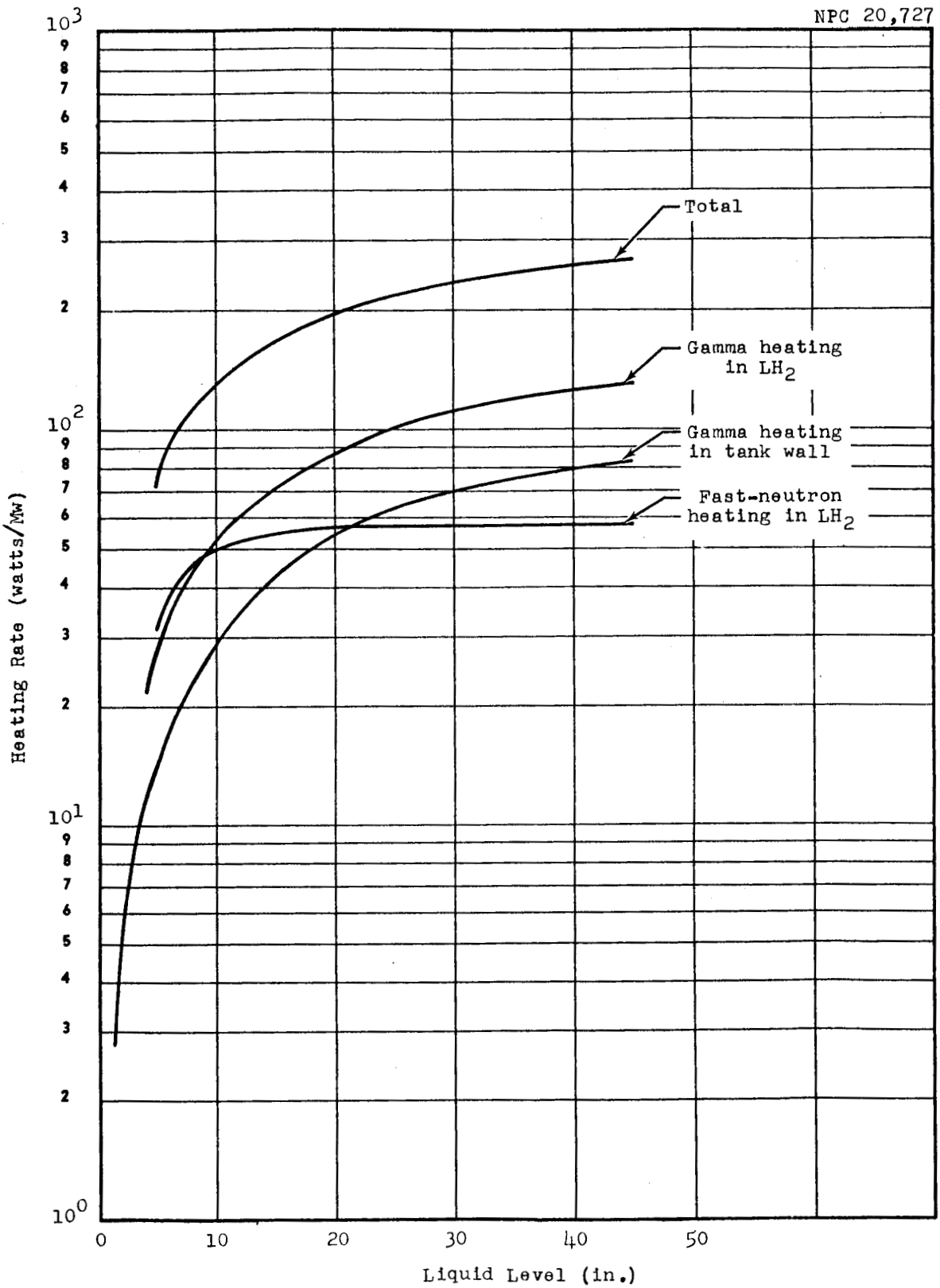

Figure 4.3-5 COHORT-Calculated Nuclear-Radiation Heating Rates: Configuration 1

heating rates, as a function of liquid level in the tank, are shown in Figure 4.3-5. The gamma heating rates shown in the wall are those discussed in Section 4.2.

4.3.5 Comparison of the Heating-Rate Data

The ambient-heat-leak values, as determined from boil-off data and from the temperature data from self-pressurization tests, are compared in Figure 4.3-6. The ambient heat leak determined from the pressurization-temperature data indicate greater variation as a function of liquid level than that from the boil-off data.

The heating-rate curves for Configurations 1 and 2 calculated by the various methods are shown in Figure 4.3-7 and 4.3-8, respectively. A comparison of the C-17 and COHORT calculations for Configuration 1 can be made in Figure 4.3-7. The COHORT results are approximately 20% higher than the C-17 calculated heating rates.

In interpreting and using the data presented in Figures 4.3-7 and 4.3-8 the following factors should be considered:

- The absolute accuracy of the boil-off data is estimated to be $\pm$ 25%.
- The accuracy of the heating rates calculated from the pressurization-temperature data must be qualified by the calculational methods used and by the evident 10 to 20% scatter in the results.
- The accuracy of the heating rates calculated with the C-17 procedure using nuclear-radiation distributions must be qualified by the effects of the finite lower energy considered by the C-17 program. This limitation would also affect the wall-heating calculations. The wall-heating curves did not include heat conduction from the walls above the liquid level and nuclear heating

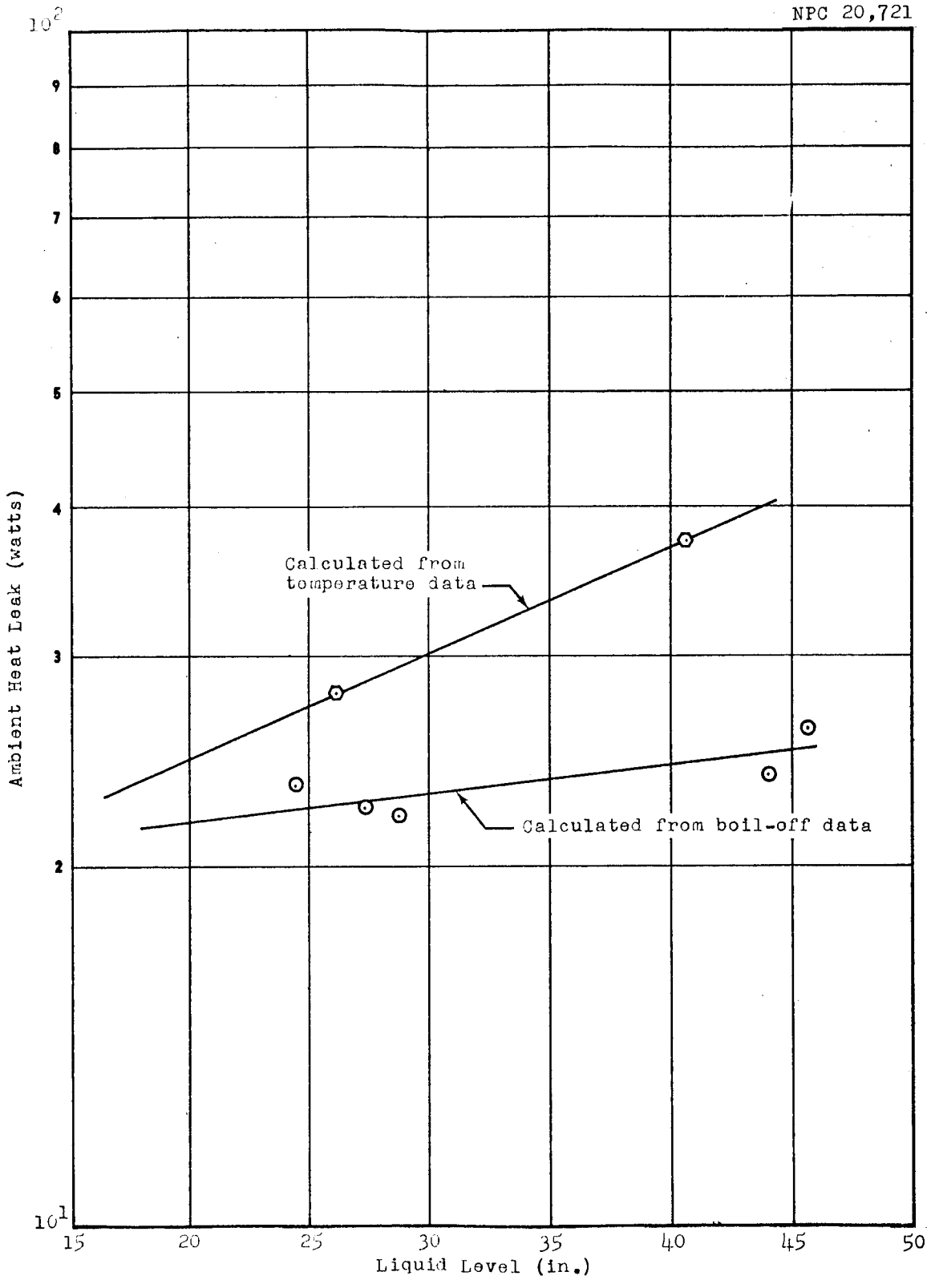

Figure 4.3-6 Comparison of Ambient-Heat-Leak Values Determined from Boil-Off and Pressurization-Temperature Data

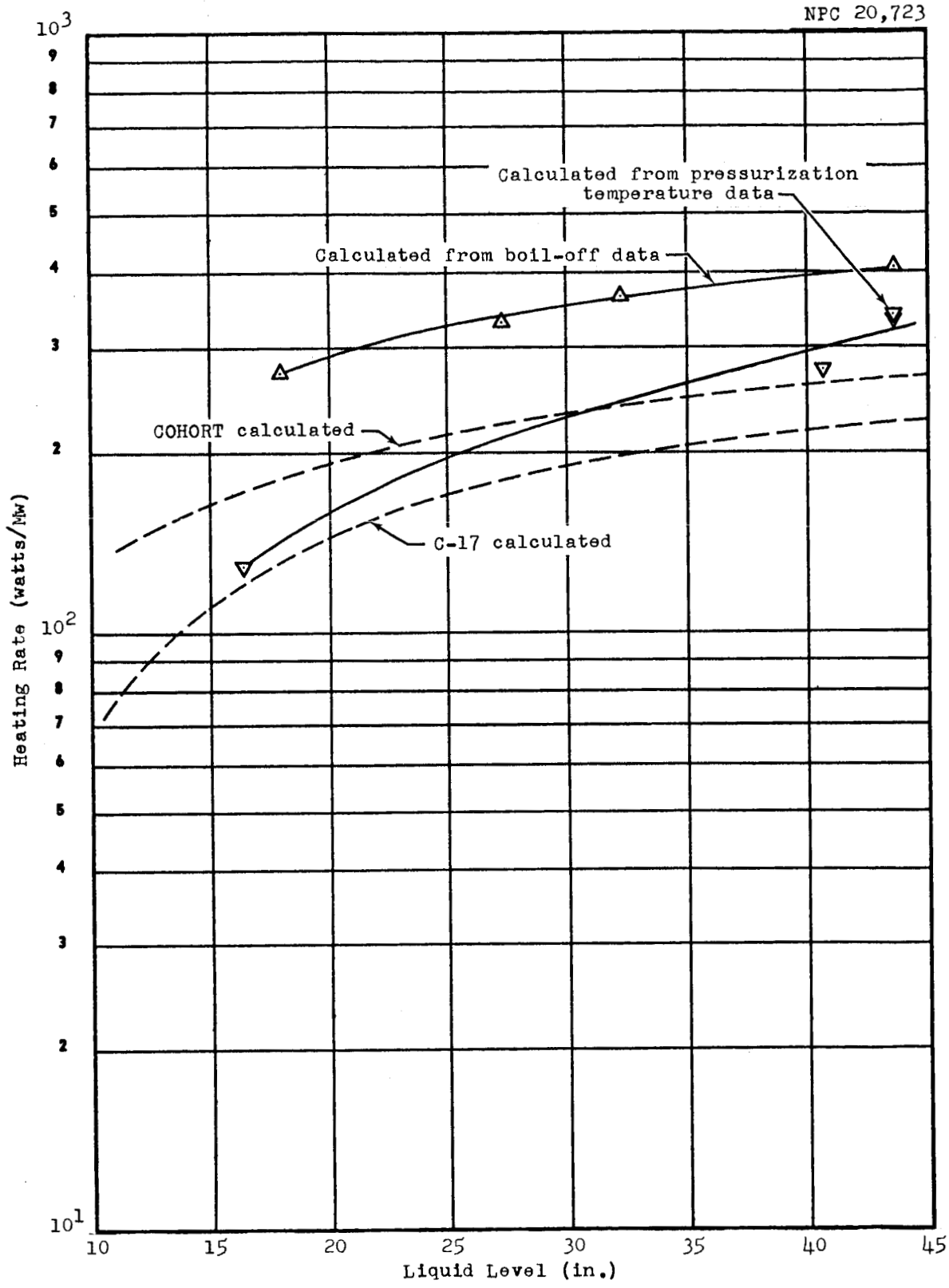

Figure 4.3-7 Comparison of Nuclear Heating Rates: Configuration 1

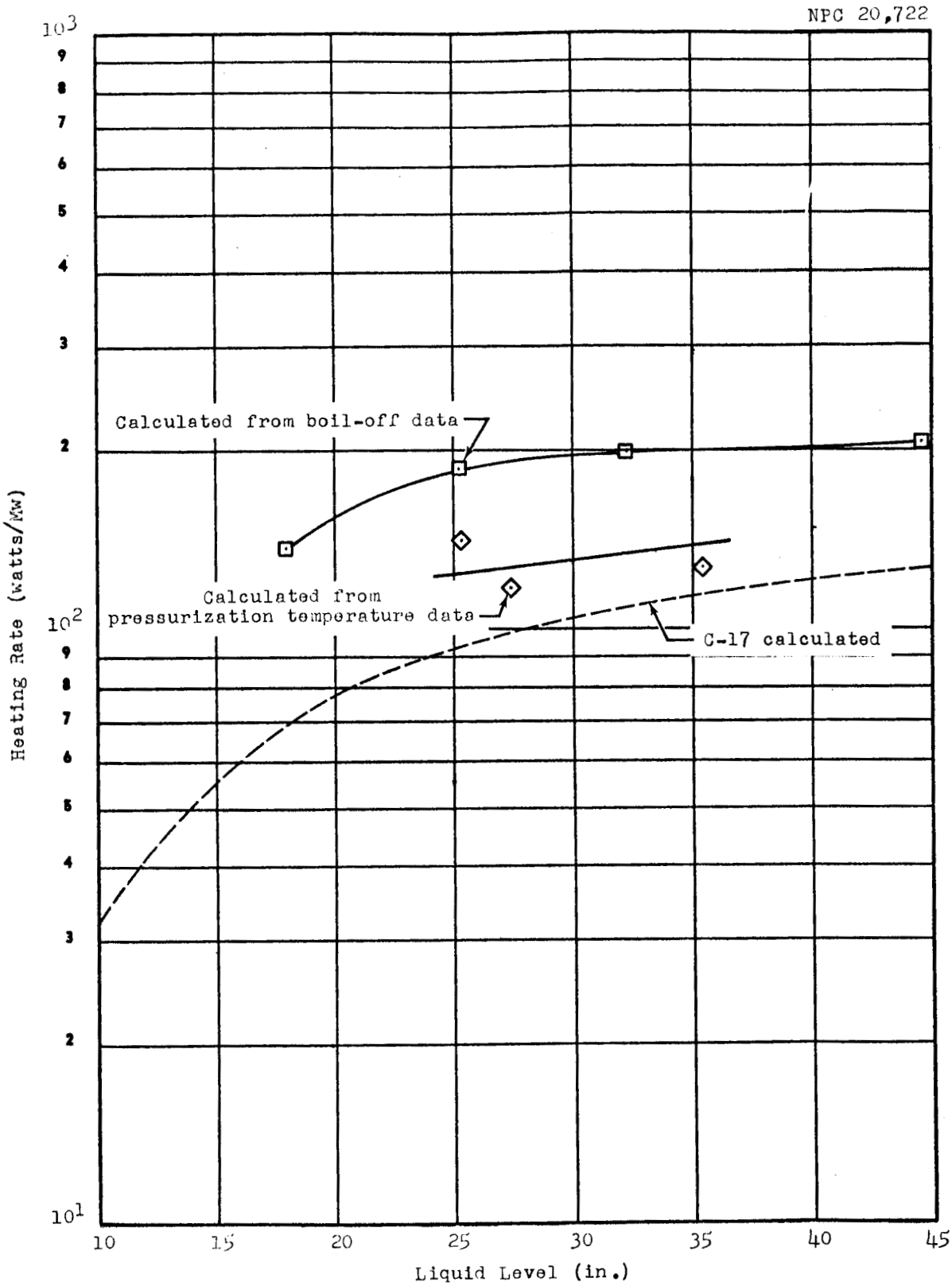

Figure 4.3-8 Comparison of Nuclear Heating Rates: Configuration 2

in the fill-drain pipe emanating from the bottom of the tank.

- The limitations of the tank-wall-heating calculations also apply to the COHORT calculated curve for Configuration 1. Although the energy cutoffs in the COHORT procedure are lower than those in C-17, part of the nuclear-radiation spectrum is neglected. The COHORT calculations also used measured nuclear-radiation intensities at the bottom of the dewar which have possible errors of 10 to 20%.

- A fairly consistent factor-of-2 difference is seen between the heating rates of Configurations 1 and 2 as determined by all methods.

4.4 Dynamic Tests (Flow Runs)

Fourteen tests, including repeats of some runs, were conducted during which the tank was pressured and liquid hydrogen was allowed to flow out of the tank to simulate the emptying of a nuclear-rocket propellant tank.

Two of the flow runs are selected for discussion here in order to illustrate the types of data obtained and the effects observed. The bulk of the data from these tests is compiled in Volume II of this report.

4.4.1 Run 18-100

The parametric conditions for this run were as follows:

Flow rate	0.039 lb(LH_2)/sec
Tank pressure	29 psia
Heating gradient	High (Config. 1)
Heating rate	Low (0.555 Mw)

The tank pressure, liquid volume, and pressurization gas utilized are shown as a function of time in Figure 4.4-1. Stable liquid flow, as shown by the liquid-volume-vs-time curve, was

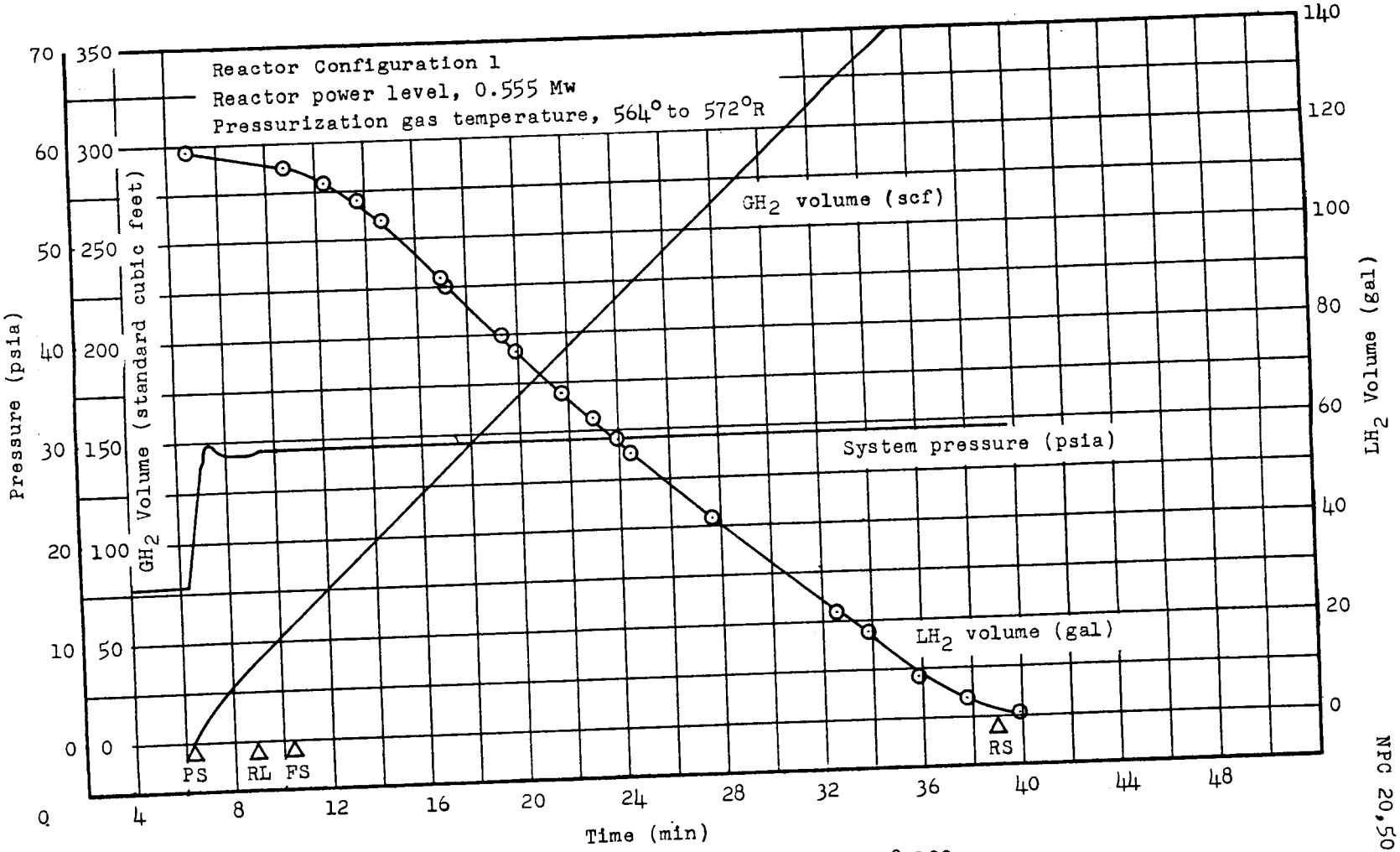

Figure 4.4-1 Pressure and Flow Data: Run 18-100

NPC 20,505

reached several minutes after start of flow (FS) as indicated by the flow meter in the system vent stack. The liquid flow rate tended to decrease just prior to the end of flow. While the pressurization-gas-utilization curve is representative, in this case part of the flow shown was vented through a maladjusted relief valve.

Temperatures in the tank are shown as a function of time in Figure 4.4-2. Thermometer numbers are noted on the curves. (Relative thermometer locations are illustrated in Figure 2.3-1 and positions relative to the tank bottom are listed in Table 2.3-1.) Ullage gas temperatures underwent sharp increases upon pressurization of the tank, as seen with Thermometers 18, 17, and 16. Some oscillations are seen in the Thermometer 15 data between start of pressurization and start of flow, indicating that it was at, or near, the liquid-gas interface.

Temperatures registered with submerged thermometers, including those nearest the tank wall (see below), fell within the $0.2^{\circ}R$- wide band shown in the figure. Saturation temperature was reached approximately one minute before reactor shutdown (RS) and two minutes before the tank was emptied, as indicated by the leveling off of the liquid temperature. The anomalies seen with Thermometers 4 and 5 at this time probably resulted from boiling of the liquid. The strip-chart recorded data from Thermometer 1, shown in Figure 4.4-3, illustrates more clearly that equilibrium conditions were reached. The temperature scales on the strip-chart records give nominal values only; the timing marks on this curve and on the one in Figure 4.4-4 occur at

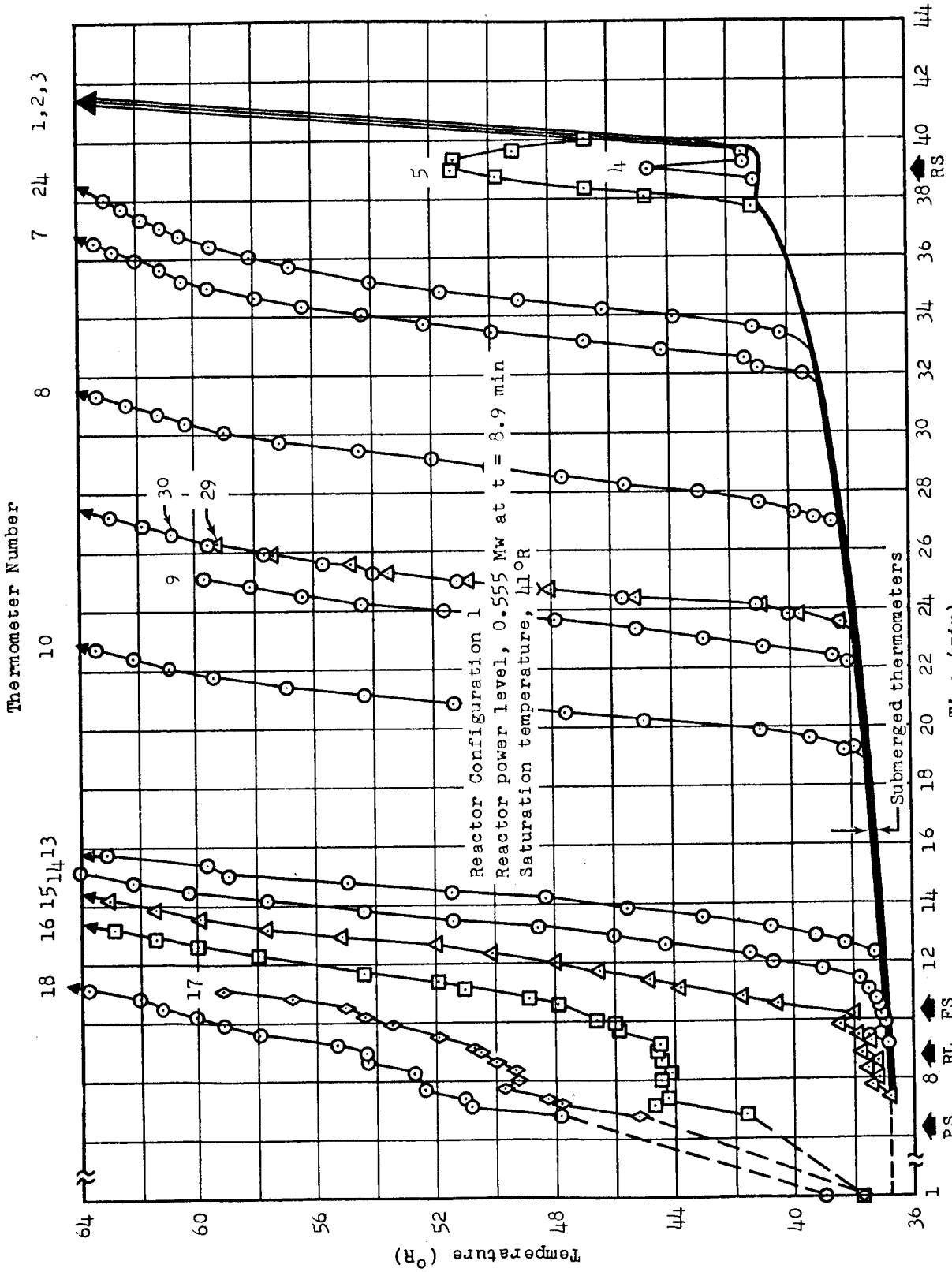

Figure 4.4-2 Temperature Rise during Flow Test: Run 18-100

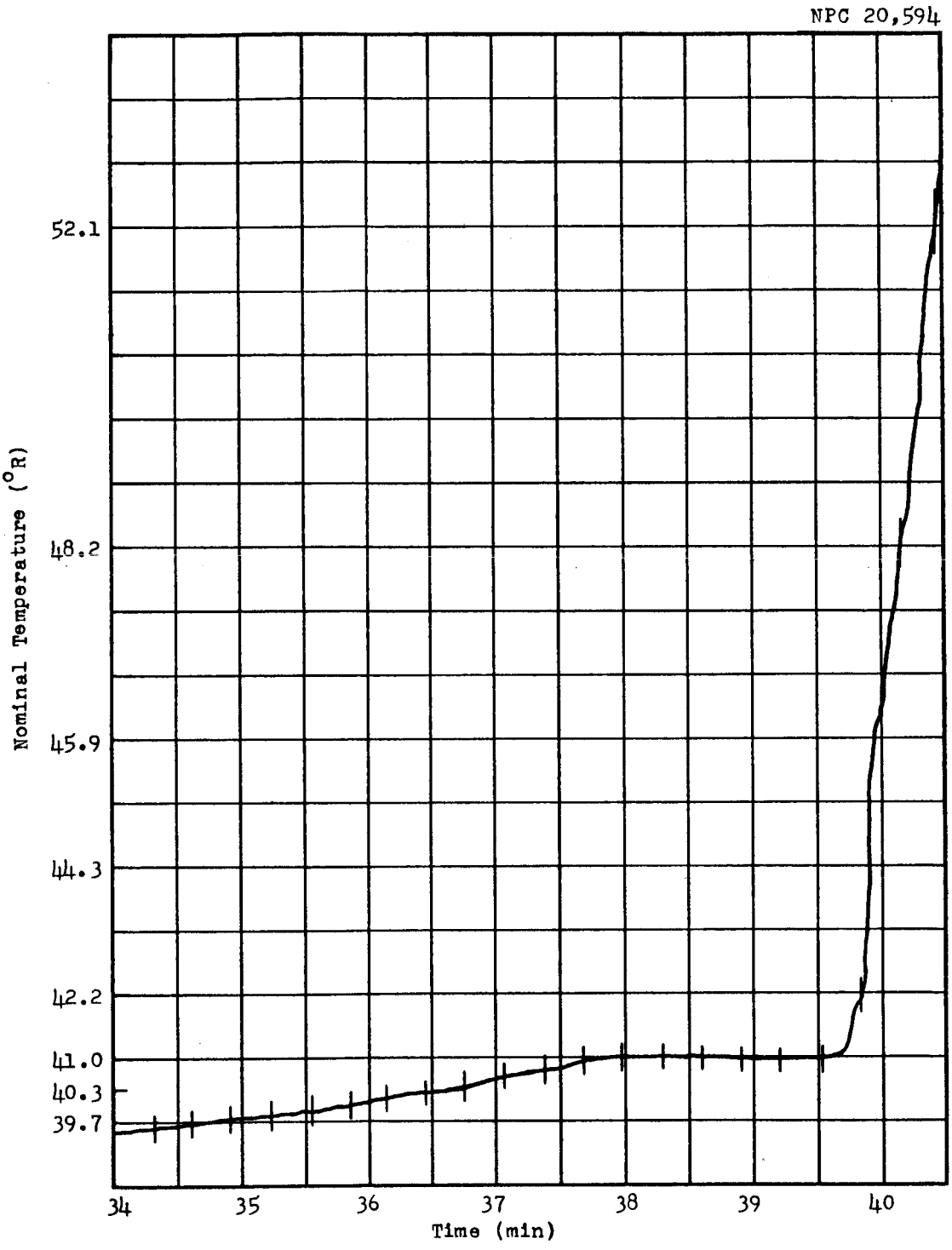

Figure 4.4-3 Strip-Chart Temperature Data: Run 18-100, Thermometer 1

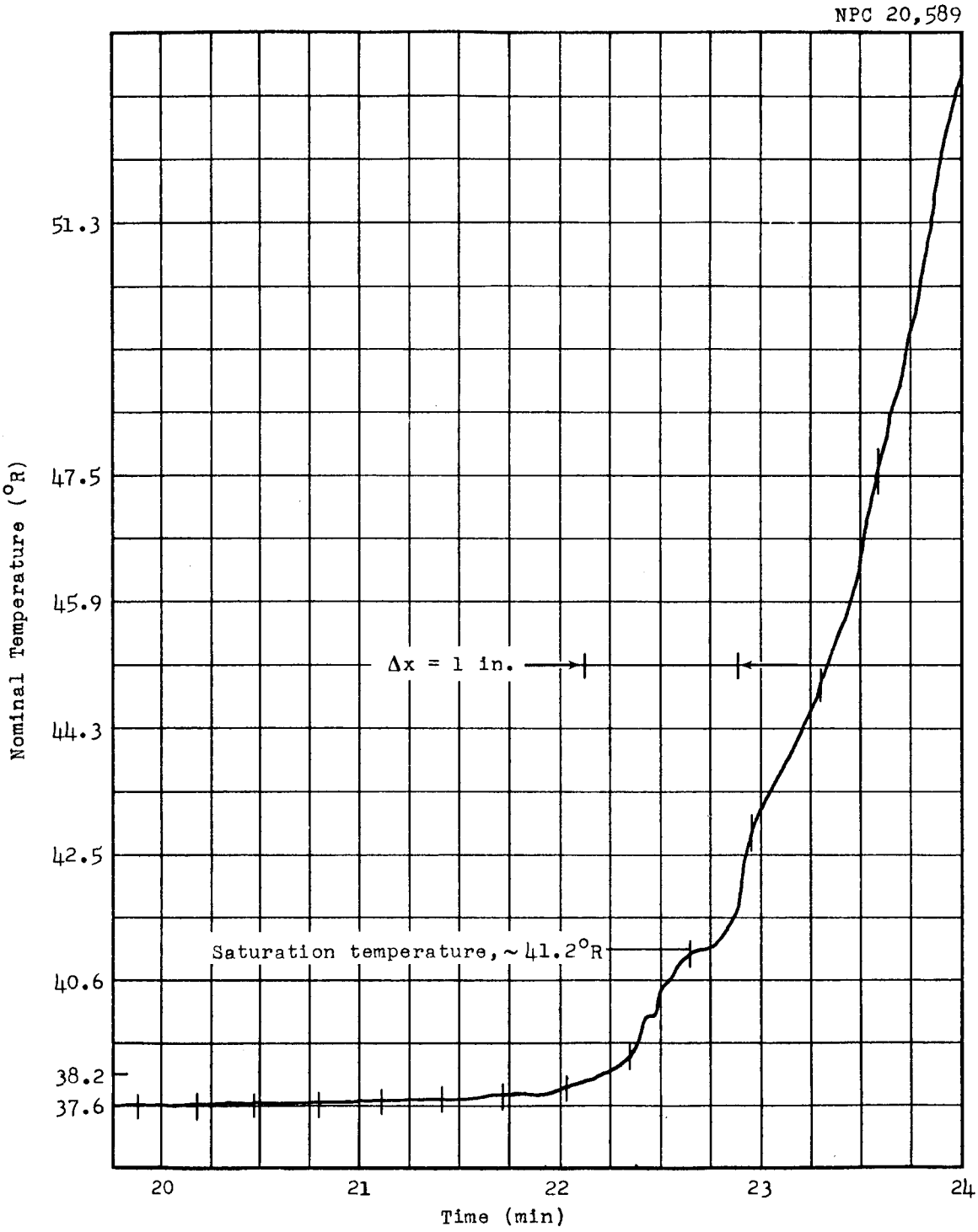

Figure 4.4-4 Strip-Chart Temperature Data: Run 18-100, Thermometer 9

0.31-min intervals.

Temperature change as the liquid level dropped past a thermometer is illustrated best by the strip-chart-recorded data in Figure 4.4-4 from Thermometer 9, which is located approximately midway on the vertical axis of the tank. The approximate saturation temperature and the time interval corresponding to a 1-in. change in liquid level are shown in this figure to illustrate the degree of continuity between bulk liquid and gas temperatures across the interface.

Temperature distributions in the tank at several times during the run are shown in Figure 4.4-5. For this and the other runs, liquid temperatures along the vertical axis of the tank did not vary with location within the limits of measurement accuracy, $\leq 0.2^{\circ}F$. No measurable deviations from the axial temperatures were recorded, either by thermometers 1/2 in. from the tank wall (Thermometers 24 and 29) or by Thermometer 30, which was nearly in contact with the wall. The data obtained with Thermometer 25, which was also near the wall, did show deviations; however, considerable drift in calibration occurred and the data are considered questionable.

4.4.2 Run 22-109

Parametric conditions for this run were as follows:

Flow rate	0.13 lb(LH_2)/sec
Tank pressure	54 psia
Heating gradient	Low (Config. 2)
Heating rate	High (5.72 Mw)

The tank pressure, liquid volume, and pressurization gas

NPC 20,728

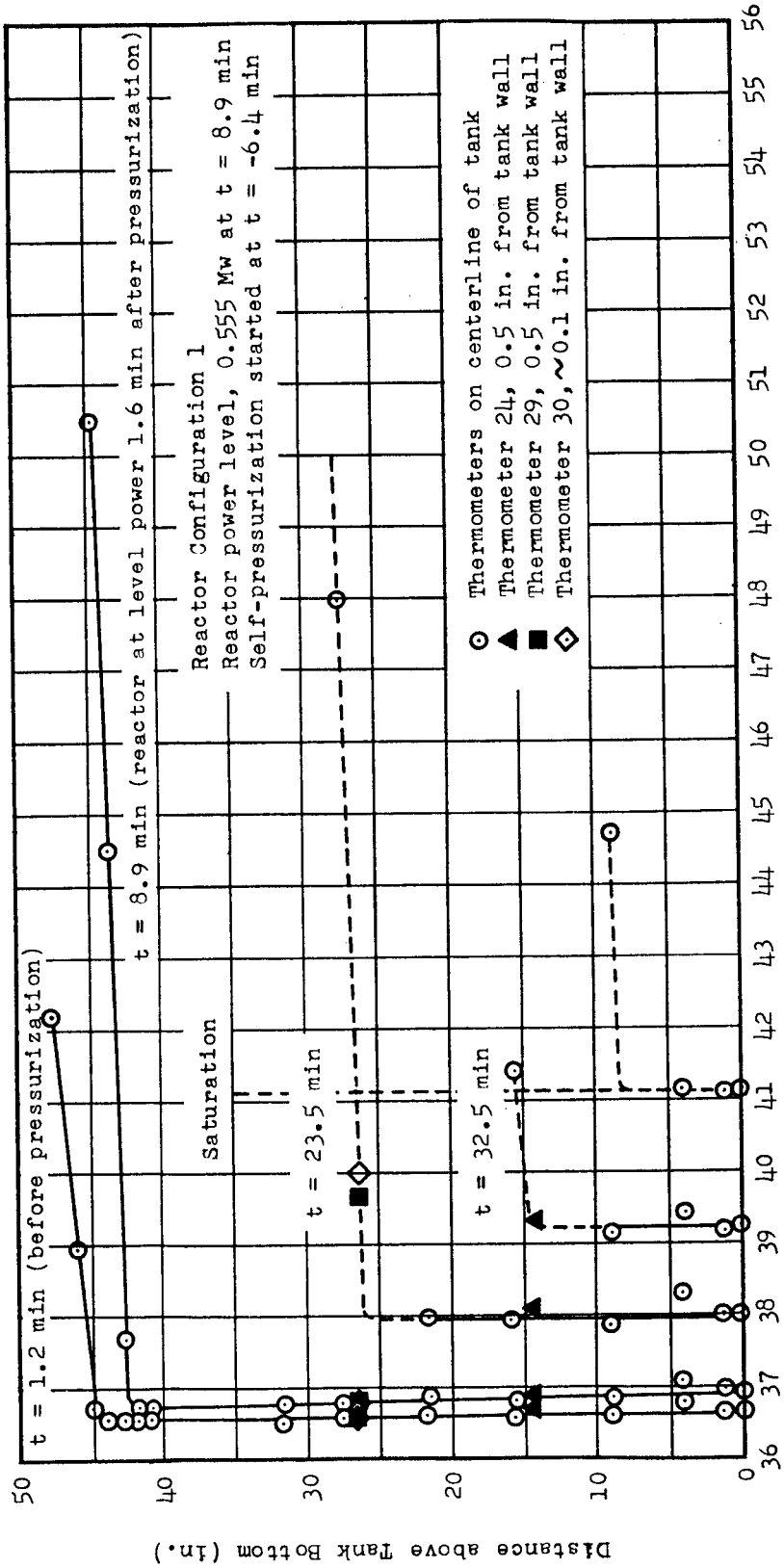

Figure 4.4-5 Temperature Profiles: Run 18-100

utilized are shown as a function of time in Figure 4.4-6. The liquid flow rate was very stable, as shown by the linearity of the liquid-volume-vs-time curve. The system pressure varied and was lower than the desired 60 psia. The pressurization-gas-utilization curve shows the high rate of flow during pressurization of the tank prior to cryogen flow and the constancy during stable cryogen flow conditions that are characteristic of this type of system.

Temperatures inside the tank are shown as a function of time in Figure 4.4-7. Temperature registered by the submerged thermometers fell within the 0.2° to 0.4°R-wide band as shown. The characteristic increase in ullage-gas temperature with time and distance above the liquid-gas interface can be seen, although the time resolution is less than for Run 18 (Figure 4.4-2) when the liquid level decreased more slowly. The anomalous behavior of Thermometer 5 near the end of the run is not understood. The bulk liquid temperature was approximately 3°R below saturation temperature when the tank was emptied.

Temperature variations across the liquid-gas interface are illustrated by the strip-chart-recorded data in Figures 4.4-8 and 4.4-9 from Thermometers 10 and 1. The time interval corresponding to a 1-in. change in liquid level in conjunction with the Figure 4.4-8 curve indicates a stratified layer of less than 1-in. thickness.

Temperature distributions in the tank at various times during the run are shown in Figure 4.4-10. Temperature variations along the tank axis and radially at the two horizontal positions, 4.2 and 26.3 in., were within the limit of measurement accuracy.

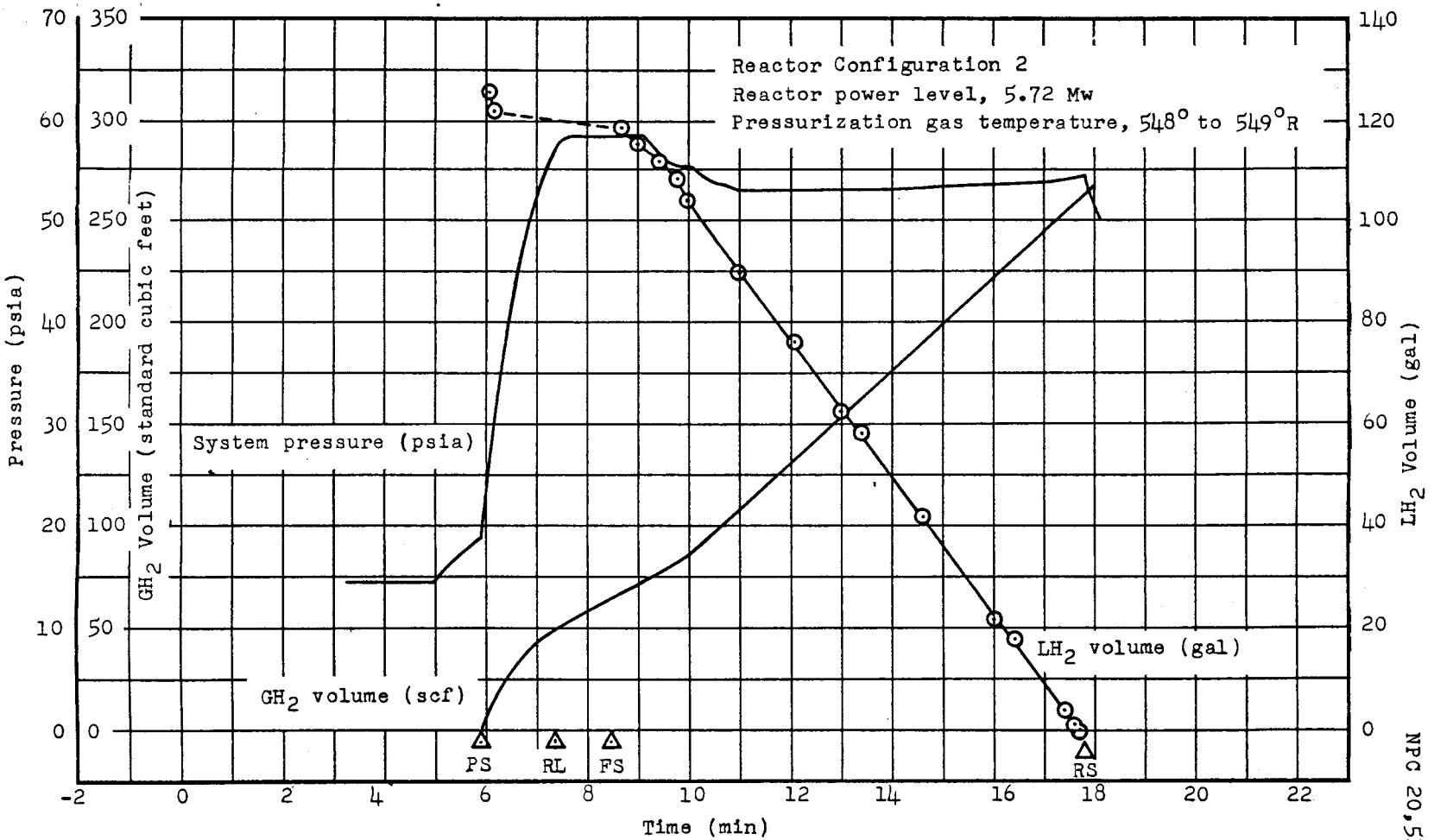

Figure 4.4-6 Pressure and Flow Data: Run 22-109

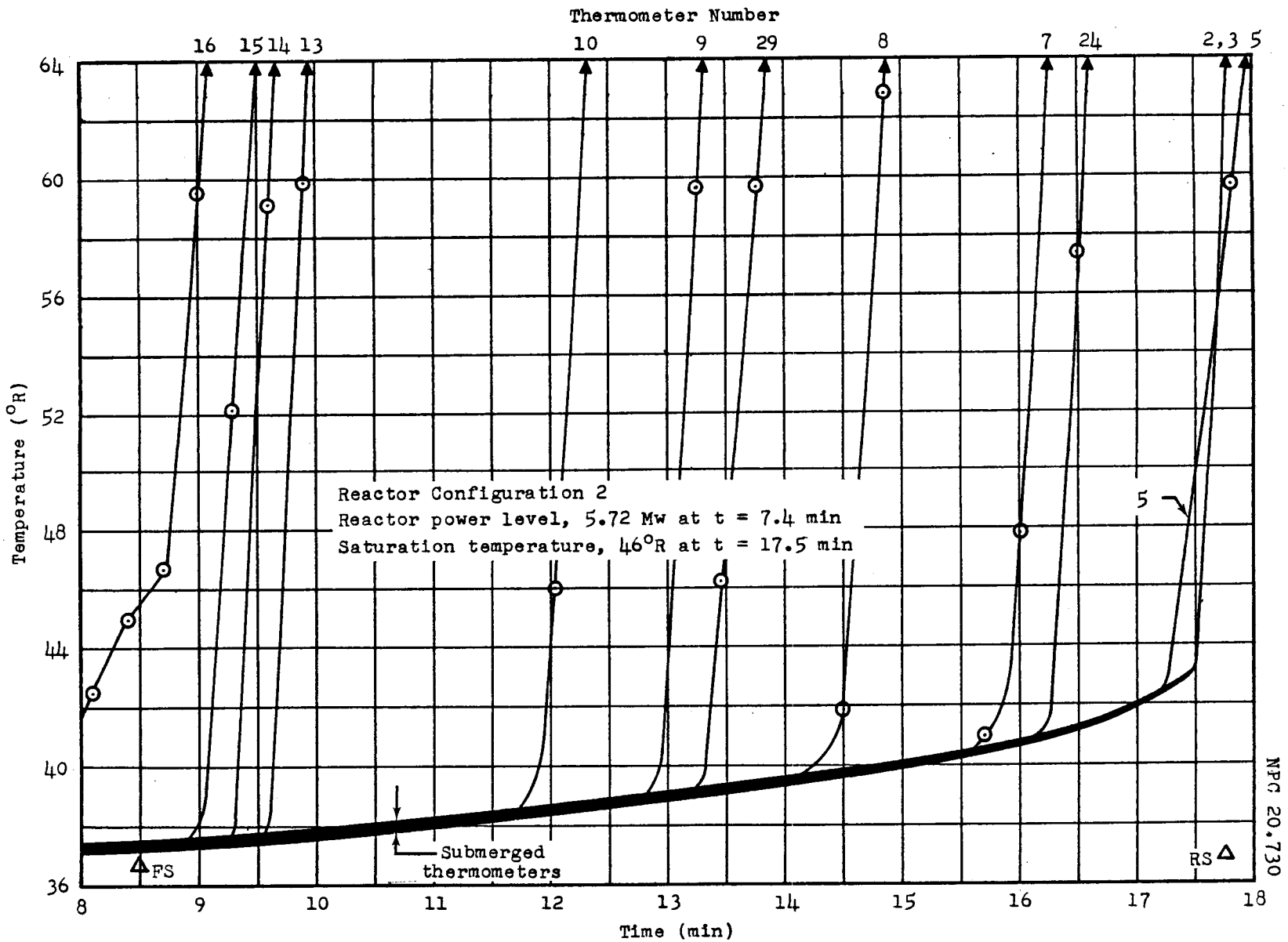

Figure 4.4-7 Temperature Rise during Flow Test: Run 22-109

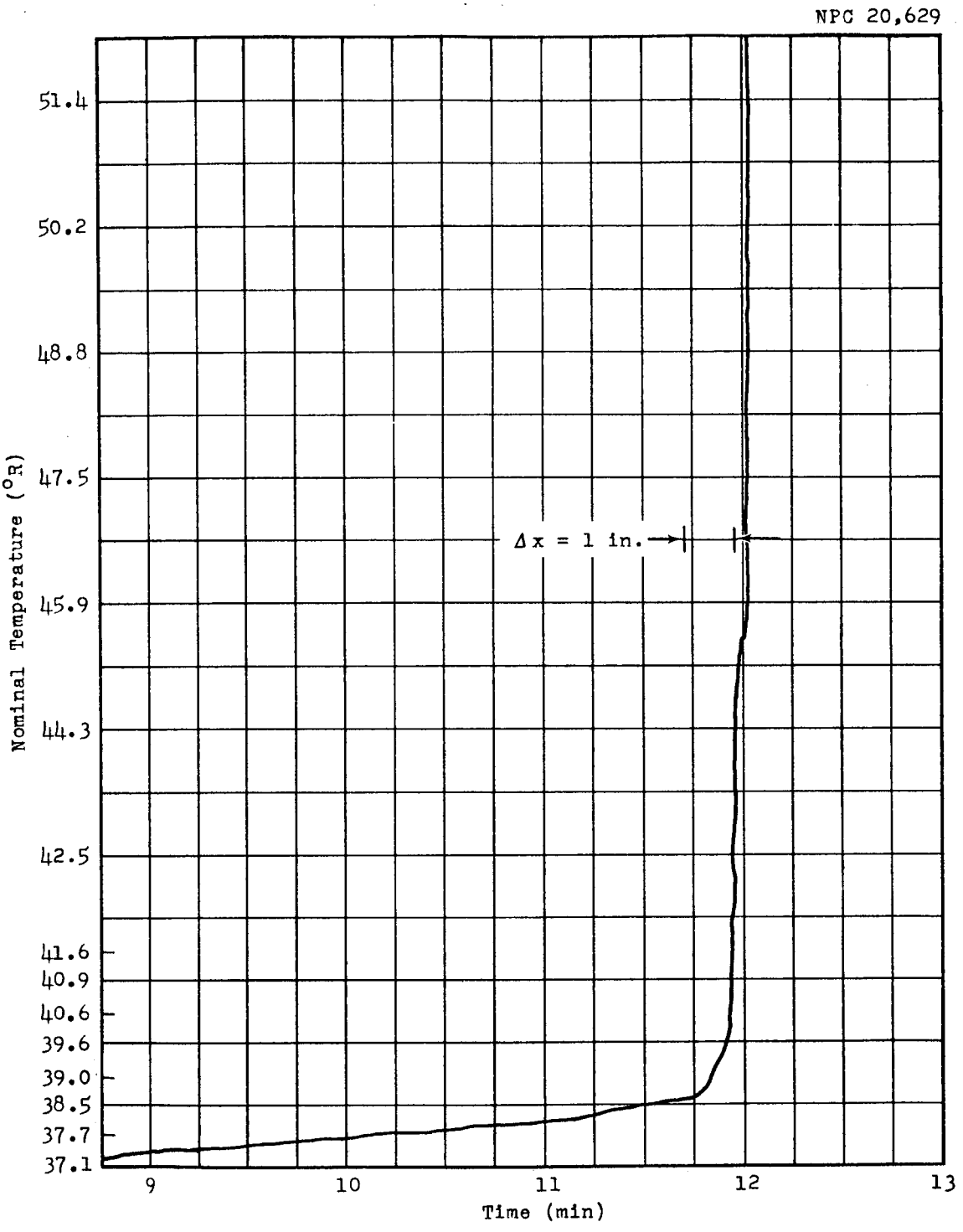

Figure 4.4-8 Strip-Chart Temperature Data: Run 22-109, Thermometer 10

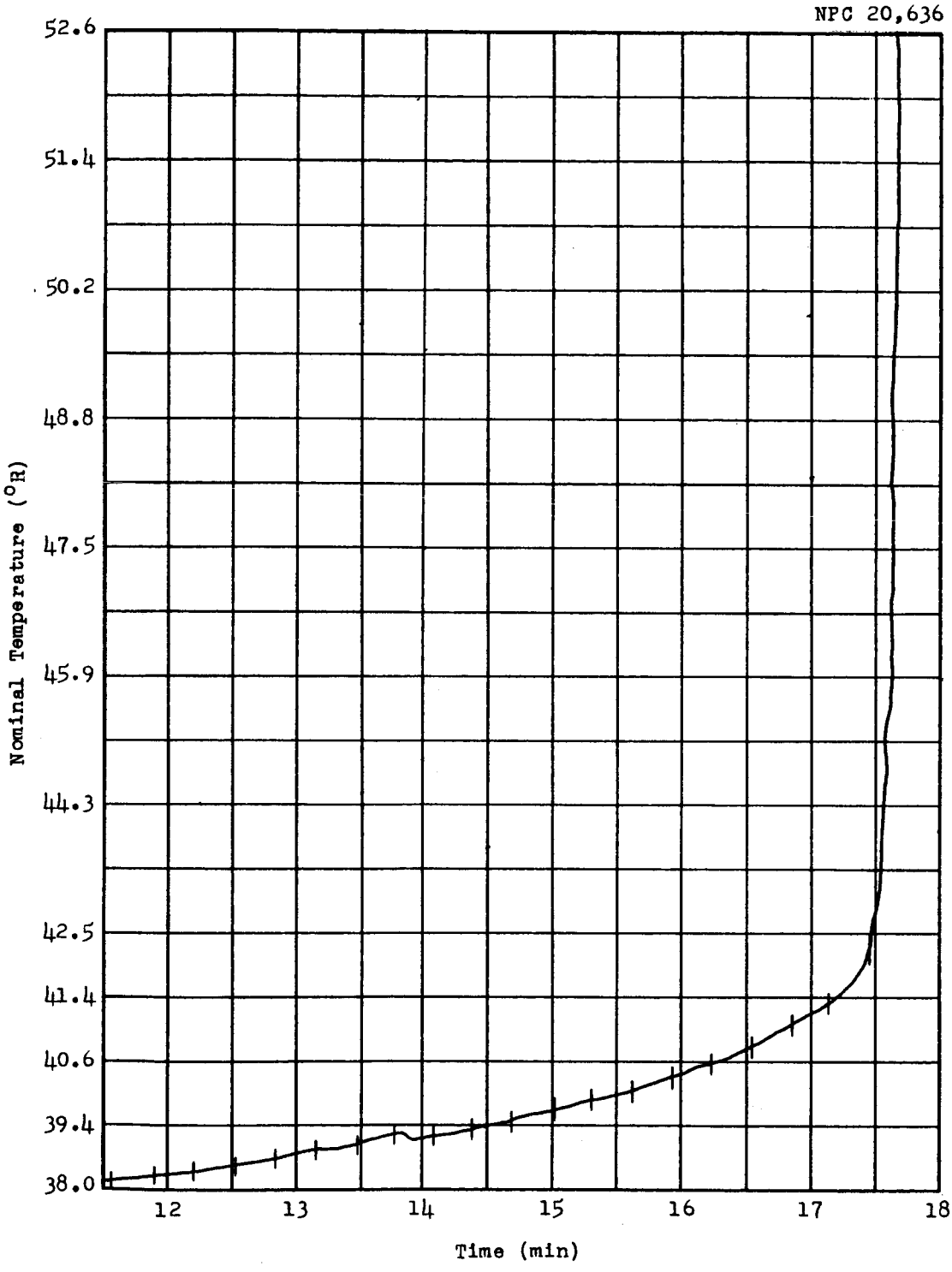

Figure 4.4-9 Strip-Chart Temperature Data: Run 22-109, Thermometer 1

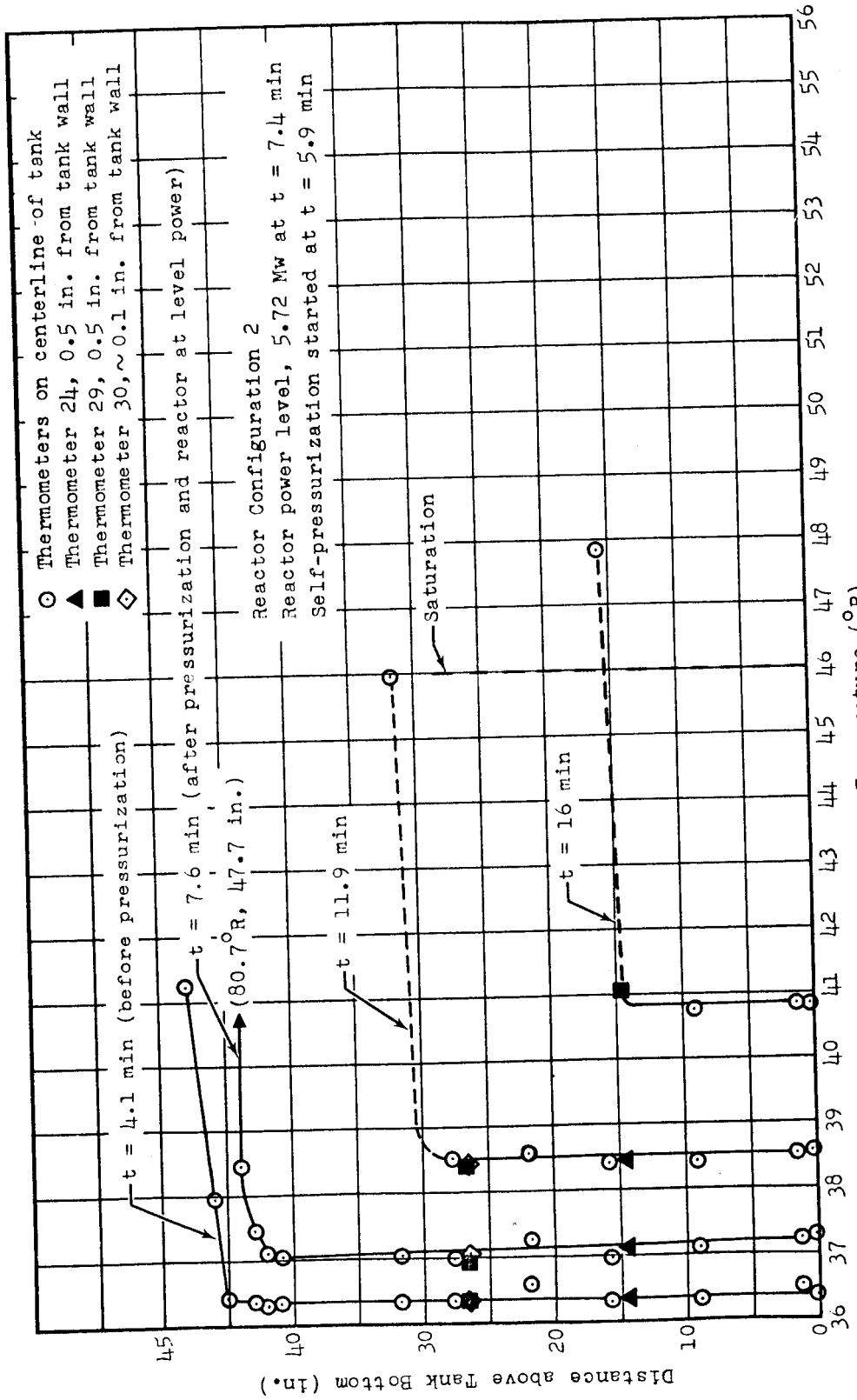

Figure 4.4-10 Temperature Profiles: Run 22-109

Table 4.1-1

Calculated Gamma Dose Rates: Configuration 1
(r/hr-w)

Detector Coordinates (in.)			Gamma Dose-Rate Components				Total Gamma Dose Rate
x	y	z	Primary Gammas	(n,γ) in LH_2	(n,γ) in Stainless-Steel Pressure Vessel	(n,n') in Iron of Pressure Vessel	
0.10	0	0	2.05(0)	7.99(-2)	1.45(0)	7.06(-2)	3.65(0)
1.08	0	0	1.88(0)	1.04(-1)	1.33(0)	6.66(-2)	3.38(0)
3.05	0	0	1.60(0)	1.33(-1)	1.04(0)	5.28(-2)	2.83(0)
5.16	0	0	1.56(0)	1.35(-1)	7.82(-1)	3.98(-2)	2.52(0)
9.84	0	0	1.15(0)	1.01(-1)	4.58(-1)	2.31(-2)	1.73(0)
14.47	0	0	8.49(-1)	6.64(-2)	2.90(-1)	1.44(-2)	1.22(0)
22.00	0	0	5.48(-1)	3.35(-2)	1.60(-1)	7.68(-3)	7.49(-1)
33.79	0	0	3.05(-1)	1.02(-2)	7.78(-2)	3.53(-3)	3.96(-1)
45.00	0	0	1.89(-1)	4.13(-3)	4.55(-2)	1.93(-3)	2.40(-1)
1.08	2.56	0	2.14(0)	8.44(-2)	1.33(0)	6.76(-2)	3.62(0)
3.05	2.56	0	1.81(0)	1.24(-1)	1.00(0)	5.11(-2)	2.99(0)
3.05	4.72	0	1.85(0)	7.45(-2)	9.17(-1)	4.66(-2)	2.89(0)
5.16	2.56	0	1.56(0)	1.32(-1)	7.62(-1)	3.87(-2)	2.49(0)
5.16	4.72	0	1.56(0)	9.27(-2)	7.11(-1)	3.61(-2)	2.40(0)
5.16	6.89	0	1.49(0)	6.38(-2)	6.08(-1)	3.07(-2)	2.19(0)
9.84	4.72	0	1.12(0)	8.38(-2)	4.26(-1)	2.15(-2)	1.65(0)
9.84	6.89	0	1.07(0)	7.15(-2)	3.96(-1)	1.99(-2)	1.56(0)
9.84	9.05	0	1.02(0)	5.49(-2)	3.56(-1)	1.79(-2)	1.45(0)
9.84	11.42	0	9.51(-1)	3.87(-2)	2.97(-1)	1.48(-2)	1.30(0)
14.47	4.72	0	8.21(-1)	5.89(-2)	2.77(-1)	1.38(-2)	1.17(0)
22.00	5.31	0	5.24(-1)	2.96(-2)	1.53(-1)	7.35(-3)	7.14(-1)
22.00	10.63	0	4.88(-1)	2.24(-2)	1.39(-1)	6.64(-3)	6.56(-1)
22.00	15.90	0	4.34(-1)	1.42(-2)	1.17(-1)	5.59(-3)	5.71(-1)
33.79	5.31	0	2.93(-1)	9.58(-3)	7.63(-2)	3.45(-3)	3.82(-1)
33.79	10.63	0	2.77(-1)	8.09(-3)	7.20(-2)	3.24(-3)	3.60(-1)
33.79	15.90	0	2.58(-1)	6.25(-3)	6.56(-2)	2.67(-3)	3.32(-1)

Table 4.1-2

Calculated Gamma Dose Rates: Configuration 2
(r/hr-w)

Detector Coordinates (in.)			Gamma Dose-Rate Components					Total Gamma Dose Rate
x	y	z	Primary Gammas	(n,γ) in LH_2	(n,γ) in Stainless-Steel Pressure Vessel	(n,n') in Iron of Pressure Vessel	(n,γ) in 4" H_2O Shield	
0.10	0	0	1.08(-0)	1.02(-2)	6.40(-1)	2.63(-2)	4.37(-1)	2.19(0)
5.16	0	0	7.76(-1)	1.75(-2)	3.94(-1)	1.70(-2)	2.44(-1)	1.45(0)
14.47	0	0	4.97(-1)	9.69(-3)	1.71(-1)	7.26(-3)	9.56(-2)	7.80(-1)
22.00	0	0	3.31(-1)	5.55(-3)	1.02(-1)	4.21(-3)	5.33(-2)	4.96(-1)
33.79	0	0	1.91(-1)	1.91(-3)	5.32(-2)	2.05(-3)	2.59(-2)	2.74(-1)
45.00	0	0	1.21(-1)	7.45(-4)	3.23(-2)	1.16(-3)	1.48(-2)	1.70(-1)
22.00	5.31	0	3.19(-1)	4.86(-3)	9.92(-2)	4.07(-3)	5.16(-2)	4.79(-1)
22.00	10.63	0	3.02(-1)	3.62(-3)	9.05(-2)	3.69(-3)	4.70(-2)	4.47(-1)
22.00	15.90	0	2.74(-1)	2.25(-3)	7.85(-2)	3.18(-3)	4.08(-2)	3.99(-1)
33.79	5.93	0	1.84(-1)	1.76(-3)	5.23(-2)	2.01(-3)	2.53(-2)	2.65(-1)
33.79	10.63	0	1.77(-1)	1.44(-3)	4.94(-2)	1.89(-3)	2.41(-2)	2.54(-1
33.79	15.90	0	1.67(-1)	1.06(-3)	4.57(-2)	1.74(-3)	2.21(-2)	2.38(-1)

Table 4.1-3

Calculated Fast-Neutron Spectra: Configuration 1

Detector Coordinates (in.)			Fast-Neutron-Flux Spectra (n/cm^2-sec-Mev-w)										Fast-Neutron Flux > 2.9 Mev $\left(\frac{n}{cm^2\text{-sec-w}}\right)$
x	y	z	0.33 Mev	1.0 Mev	2.0 Mev	3.0 Mev	4.0 Mev	6.0 Mev	8.0 Mev	10.0 Mev	14.0 Mev	18.0 Mev	
0.10	0	0	4.20(4)	2.50(4)	1.69(4)	1.13(4)	7.19(3)	2.51(3)	6.78(2)	1.54(2)	6.90(0)	1.76(-1)	2.48(4)
5.16	0	0	1.52(4)	8.73(3)	6.19(3)	4.34(3)	2.89(3)	1.08(3)	3.01(2)	6.91(1)	3.60(0)	8.32(-2)	9.68(3)
14.47	0	0	2.48(3)	1.05(3)	8.39(2)	6.57(2)	4.95(2)	2.15(2)	6.78(1)	1.62(1)	1.34(0)	2.79(-2)	1.69(3)
22.00	0	0	7.55(2)	2.39(2)	1.96(2)	1.62(2)	1.33(2)	6.44(1)	2.26(1)	5.63(0)	5.88(-1)	1.19(-2)	4.76(2)
33.79	0	0	9.18(1)	2.93(1)	2.24(1)	2.03(1)	1.83(1)	1.05(1)	4.30(0)	1.16(0)	8.58(-2)	1.63(-3)	7.11(1)
45.00	0	0	8.68(0)	4.48(0)	3.29(0)	3.13(0)	2.93(0)	2.02(0)	9.29(-1)	2.64(-1)	7.90(-3)	1.28(-4)	1.28(1)
22.00	5.31	0	7.47(2)	2.45(2)	2.00(2)	1.65(2)	1.35(2)	6.48(1)	2.26(1)	5.61(0)	5.59(-1)	1.13(-2)	4.95(2)
22.00	10.63	0	8.46(2)	2.93(2)	2.39(2)	1.95(2)	1.56(2)	7.33(1)	2.50(1)	6.15(0)	5.97(-1)	1.21(-2)	5.68(2)
22.00	15.90	0	1.09(3)	4.18(2)	3.36(2)	2.68(2)	2.08(2)	9.37(1)	3.07(1)	7.42(0)	6.87(-1)	1.42(-2)	7.47(2)
33.79	5.31	0	9.32(1)	2.90(1)	2.23(1)	2.01(1)	1.81(1)	1.04(1)	4.22(0)	1.14(0)	8.82(-2)	1.68(-3)	7.22(1)
33.79	10.63	0	1.02(2)	3.07(1)	2.37(1)	2.12(1)	1.90(1)	1.08(1)	4.37(0)	1.17(0)	9.71(-2)	1.87(-3)	7.55(1)
33.79	15.90	0	1.17(2)	3.42(1)	2.67(1)	2.36(1)	2.10(1)	1.16(1)	4.65(0)	1.23(0)	1.12(-1)	2.19(-3)	8.23(1)

Table 4.1-4

Calculated Fast-Neutron Spectra: Configuration 2

Detector Coordinates (in.)			Fast-Neutron-Flux Spectra (n/cm^2-sec-Mev-w)										Fast-Neutron Flux > 2.9 Mev $\left(\frac{n}{cm^2\text{-sec-w}}\right)$
x	y	z	0.33 Mev	1.0 Mev	2.0 Mev	3.0 Mev	4.0 Mev	6.0 Mev	8.0 Mev	10.0 Mev	14.0 Mev	18.0 Mev	
0.10	0	0	7.34(3)	3.57(3)	2.76(3)	2.09(3)	1.51(3)	6.25(2)	1.88(2)	4.40(1)	3.09(0)	6.56(-2)	5.11(3)
5.16	0	0	3.00(3)	1.19(3)	9.62(2)	7.63(2)	5.86(2)	2.60(2)	8.35(1)	2.00(1)	1.76(0)	3.64(-2)	2.01(3)
14.47	0	0	7.13(2)	2.13(2)	1.74(2)	1.46(2)	1.22(2)	6.08(1)	2.21(1)	5.56(0)	5.9 (-1)	1.20(-2)	4.41(2)
22.00	0	0	1.88(2)	5.49(1)	4.28(1)	3.79(1)	3.37(1)	1.87(1)	7.45(0)	1.98(0)	1.78(-1)	3.45(-3)	1.28(2)
33.79	0	0	1.44(1)	7.31(0)	5.36(0)	5.11(0)	4.77(0)	3.19(0)	1.43(0)	4.06(-1)	1.22(-2)	1.97(-4)	2.06(1)
45.00	0	0	2.32(0)	1.27(0)	9.36(-1)	8.87(-1)	8.41(-1)	6.37(-1)	3.24(-1)	9.50(-2)	2.77(-3)	4.68(-5)	4.52(0)
22.00	5.31	0	2.01(2)	5.81(1)	4.57(1)	4.01(1)	3.54(1)	1.94(1)	7.66(0)	2.02(0)	1.91(-1)	3.76(-3)	1.38(2)
22.00	10.63	0	2.61(2)	7.52(1)	6.00(1)	5.18(1)	4.51(1)	2.39(1)	9.17(0)	2.38(0)	2.41(-1)	4.81(-3)	1.73(2)
22.00	15.90	0	3.97(2)	1.23(2)	9.98(1)	8.40(1)	7.04(1)	3.52(1)	1.28(1)	3.23(0)	3.22(-1)	6.46(-3)	2.63(2)
33.79	5.31	0	1.46(1)	7.37(0)	5.40(0)	5.15(0)	4.80(0)	3.19(0)	1.42(0)	4.04(-1)	1.22(-2)	1.96(-4)	2.08(1)
33.79	10.63	0	1.77(1)	8.31(0)	6.12(0)	5.79(0)	5.38(0)	3.51(0)	1.55(0)	4.37(-1)	1.48(-2)	2.41(-4)	2.30(1)
33.79	15.90	0	2.38(1)	1.01(1)	7.45(0)	7.00(0)	6.46(0)	4.09(0)	1.77(0)	4.95(-1)	2.02(-2)	3.42(-4)	2.72(1)

Table 4.1-5

Radiation Measurements Inside Empty Tank

For Positions where All Detectors Were Used

Detector Coordinates (in.)			Gamma Dose Rate (r/hr-w)	Neutron Flux Data (n/cm²-sec-w)				Cd Ratio
				S	Mg	Al	Au	
x	y	z	Co Glass	>2.9 Mev	>7.5 Mev	>8.1 Mev	Thermal	
				Configuration 1				
0	0	0	2.82(0)	-	3.54(3)	9.45(2)	5.48(3)	1.12
1.4	0	0	3.34(0)	9.34(3)	3.09(3)	8.01(2)	-	-
8.4	0	0	2.04(0)	1.66(4)	1.80(3)	5.02(2)	2.59(3)	1.10
20.4	0	0	1.14(0)	7.99(3)	1.05(3)	2.47(2)	5.08(3)	1.47
				Configuration 2				
0	0	0	1.50(0)	1.82(3)	6.73(2)	2.19(2)	3.04(1)	1.01
1.4	0	0	1.63(0)	4.79(3)	6.73(2)	2.09(2)	-	-
8.4	0	0	1.11(0)	3.12(3)	4.05(2)	1.32(2)	1.66(2)	1.06
20.4	0	0	6.19(-1)	1.66(3)	2.43(2)	7.10(1)	3.42(2)	1.21

For Positions Where Cobalt Glass and Sulfur Were Used

Detector Coordinates (in.)			Configuration 1		Configuration 2	
			Co Glass (r/hr-w)	S (n/cm²-sec-w)	Co Glass (r/hr-w)	S (n/cm²-sec-w)
x	y	z				
4.4	0	0	2.62(0)	2.36(4)	1.37(0)	4.06(3)
14.4	0	0	1.51(0)	1.07(4)	-	2.34(3)
27.4	0	0	8.62(-1)	-	4.88(-1)	1.18(3)
39.4	0	0	5.96(-1)	3.40(3)	3.34(-1)	7.82(2)
56.0	0	0	3.84(-1)	2.24(3)	2.25(-1)	5.18(2)
1.4	3	0	3.42(0)	3.23(4)	-	5.58(3)
9.4	4	0	1.83(0)	1.43(4)	1.01(0)	2.92(3)
9.4	10	0	1.71(0)	1.24(4)	9.76(-1)	2.72(3)
21.4	4	0	1.05(0)	7.37(3)	-	1.50(3)
21.4	8	0	9.96(-1)	6.88(3)	3.64(-1)	1.57(3)
21.4	12	0	1.00(0)	6.80(3)	5.70(-1)	1.48(3)
21.4	16	0	9.25(-1)	-	-	1.40(3)
33.4	4	0	6.74(-1)	4.37(3)	3.90(-1)	9.92(2)
33.4	8	0	5.76(-1)	4.35(3)	3.86(-1)	9.54(2)
33.4	12	0	6.66(-1)	3.98(3)	3.75(-1)	8.94(2)
33.4	16	0	6.66(-1)	3.99(3)	3.90(-1)	9.69(2)
1.4	0	3	3.21(0)	3.18(4)	1.71(0)	5.63(3)
9.4	0	4	1.80(0)	1.48(4)	9.87(-1)	2.88(3)
9.4	0	10	1.71(0)	1.17(4)	9.00(-1)	2.39(3)
21.4	0	4	1.07(0)	7.45(3)	6.15(-1)	1.63(3)
21.4	0	8	1.04(0)	6.66(3)	-	1.50(3)
21.4	0	12	9.02(-1)	6.17(3)	5.48(-1)	1.37(3)
21.4	0	16	9.02(-1)	5.66(3)	5.18(-1)	1.14(3)
33.4	0	4	6.82(-1)	4.28(3)	3.71(-1)	9.59(2)
33.4	0	8	6.98(-1)	4.33(3)	3.75(-1)	9.78(2)
33.4	0	12	6.70(-1)	3.97(3)	-	9.26(2)
33.4	0	16	6.51(-1)	3.77(3)	3.23(-1)	8.41(2)

Table 4.1-6
Radiation Measurements Inside LH_2-Filled Tank

For Positions Where All Detectors Were Used

Detector Coordinates (in.)			Gamma Dose Rate (r/hr-w)	Neutron-Flux Data (n/cm^2-sec-w)				Cd Ratio
				S	Mg	Al	Au	
x	y	z	Co Glass	>2.9 Mev	>7.5 Mev	>8.1 Mev	Thermal	
				Configuration 1				
0	0	0	3.08(0)	2.47(4)	-	8.90(2)	1.56(5)	3.24
1.4	0	0	2.70(0)	1.82(4)	-	6.51(2)	1.94(5)	4.94
8.4	0	0	1.82(0)	4.58(3)	3.89(2)	2.07(2)	1.01(5)	12.6
20.4	0	0	8.24(-1)	-	5.39(1)	3.36(1)	1.29(4)	21.7
				Configuration 2				
0	0	0	1.49(0)	4.45(3)	3.82(2)	2.12(2)	1.75(4)	3.59
1.4	0	0	1.34(0)	3.25(3)	2.93(2)	1.64(2)	2.40(4)	26.3
8.4	0	0	9.43(-1)	9.18(2)	9.91(1)	5.89(1)	1.34(4)	10.6
20.4	0	0	5.09(-1)	1.28(2)	2.00(1)	8.86(0)	2.40(3)	19.8

For Positions Where Cobalt Glass and Sulfur Were Used

Detector Coordinates (in.)			Configuration 1		Configuration 2	
			Co Glass (r/hr-w)	S (n/cm^2-sec-w)	Co Glass (r/hr-w)	S (n/cm^2-sec-w)
x	y	z				
4.4	0	0	2.36(0)	1.06(4)	1.15(0)	1.95(3)
14.4	0	0	1.25(0)	-	6.60(-1)	3.42(2)
27.4	0	0	6.01(-1)	2.35(2)	3.58(-1)	4.55(1)
39.4	0	0	3.64(-1)	4.05(1)	2.26(-1)	1.27(1)
56.0	0	0	2.24(-1)	4.61(1)	1.32(-1)	1.42(1)
1.4	3	0	3.05(0)	2.65(4)	1.51(0)	-
9.4	4	0	1.24(0)	1.54(3)	8.49(-1)	8.42(2)
9.4	10	0	9.12(-1)	5.97(2)	8.49(-1)	1.65(3)
21.4	4	0	8.05(-1)	4.47(2)	4.34(-1)	1.08(2)
21.4	8	0	7.78(-1)	5.19(2)	4.53(-1)	1.19(2)
21.4	12	0	8.24(-1)	6.46(2)	4.34(-1)	1.55(2)
21.4	16	0	8.24(-1)	-	4.15(-1)	2.15(2)
33.4	4	0	4.87(-1)	7.56(1)	2.64(-1)	2.12(1)
33.4	8	0	4.41(-1)	8.50(1)	2.64(-1)	2.31(1)
33.4	12	0	4.67(-1)	1.07(2)	2.64(-1)	3.25(1)
33.4	16	0	4.60(-1)	-	2.45(-1)	4.96(1)
1.4	0	3	2.97(0)	2.41(4)	1.55(0)	4.32(3)
9.4	0	4	1.72(0)	4.19(3)	8.49(-1)	7.86(2)
9.4	0	10	1.53(0)	6.58(3)	8.11(-1)	-
21.4	0	4	8.05(-1)	4.58(2)	4.53(-1)	1.06(2)
21.4	0	8	8.43(-1)	5.05(2)	-	1.12(2)
21.4	0	12	8.05(-1)	5.77(2)	4.34(-1)	1.30(2)
21.4	0	16	8.05(-1)	6.11(2)	4.15(-1)	1.40(2)
33.4	0	4	4.75(-1)	7.42(1)	2.64(-1)	2.18(1)
33.4	0	8	4.60(-1)	7.99(1)	2.64(-1)	2.28(1)
33.4	0	12	4.60(-1)	9.69(1)	2.64(-1)	2.77(1)
33.4	0	16	4.48(-1)	1.40(2)	2.64(-1)	3.89(1)

Table 4.1-7
Radiation Measurements on Outside Surface of Empty Tank

Detector Position	Gamma Dose Rate (r/hr-w)	Neutron Flux Data (n/cm²-sec-w)				Cd Ratio
		S	Mg	Al	Au	
	Co Glass	> 2.9 Mev	> 7.5 Mev	> 8.1 Mev	Thermal	
		Configuration 1				
x,z - Plane						
1	6.12(0)	-	4.84(3)	1.72(3)	9.66(3)	1.20
2	3.14(0)	1.79(4)	2.34(3)	6.00(2)	4.37(3)	1.21
3	1.65(0)	7.55(3)	1.17(3)	2.50(2)	1.07(3)	1.11
4	8.78(-1)	5.22(3)	7.39(2)	1.63(2)	-	-
5	3.53(-1)	2.24(3)	3.52(2)	6.77(1)	1.15(3)	1.25
6	2.35(-1)	1.50(3)	2.26(2)	4.40(1)	4.16(3)	2.17
7	3.18(-1)	2.10(3)	2.64(2)	6.23(1)	2.59(3)	1.69
8	3.14(-1)	2.08(3)	2.27(2)	6.32(1)	2.38(3)	1.56
x,y - Plane						
1	7.76(0)	-	-	1.85(3)	-	-
2	4.36(0)	2.71(4)	2.88(3)	7.80(2)	5.54(3)	1.20
3	-	1.45(4)	1.61(3)	4.14(2)	1.52(3)	1.08
4	1.10(0)	7.54(3)	8.95(2)	2.36(2)	-	-
5	3.22(-1)	2.48(3)	3.52(2)	7.39(1)	9.19(2)	1.21
6	2.43(-1)	1.67(3)	1.98(2)	5.09(1)	3.61(3)	1.95
7	3.41(-1)	2.21(3)	2.49(2)	6.27(1)	2.35(3)	1.54
8	2.71(-1)	2.04(3)	2.77(2)	6.07(1)	2.10(3)	1.60
		Configuration 2				
x,z - Plane						
1	3.04(0)	9.05(3)	1.08(3)	3.48(2)	-	-
2	1.69(0)	3.26(3)	4.62(2)	1.52(2)	3.34(2)	1.16
3	9.38(-1)	1.50(3)	2.56(2)	7.18(1)	2.61(2)	1.24
4	4.50(-1)	1.01(3)	1.60(2)	4.76(1)	1.32(2)	1.13
5	1.84(-1)	4.54(2)	7.90(1)	2.05(1)	2.16(2)	1.39
6	1.46(-1)	4.00(2)	6.05(1)	1.53(1)	4.67(2)	2.07
7	-	3.98(2)	-	1.72(1)	4.16(2)	2.08
8	-	4.69(2)	6.85(1)	1.90(1)	3.01(2)	1.51
x,y - Plane						
1	3.36(0)	9.92(3)	1.48(3)	4.24(2)	-	-
2	2.29(0)	5.54(3)	7.39(2)	2.32(2)	1.47(3)	1.46
3	-	3.01(3)	1.38(2)	1.31(2)	5.36(2)	1.30
4	-	1.56(3)	2.24(2)	6.94(1)	-	-
5	-	5.13(2)	7.83(1)	2.17(1)	1.53(2)	1.30
6	1.50(-1)	4.53(2)	6.41(1)	1.70(1)	4.92(2)	2.04
7	1.61(-1)	4.10(2)	-	1.80(1)	4.18(2)	2.11
8	3.64(-1)	4.91(2)	6.87(1)	1.96(1)	2.37(2)	1.42

Table 4.1-8

Radiation Measurements on Outside Surface of LH_2-Filled Tank

Detector Position	Gamma Dose Rate (r/hr-w)	Neutron Flux Data (n/cm^2-sec-w)				Cd Ratio
		S	Mg	Al	Au	
	Co Glass	>2.9 Mev	>7.5 Mev	>8.1 Mev	Thermal	
		Configuration 1				
x,z - Plane						
1	6.51(0)	-	-	1.77(3)	-	
2	2.78(0)	1.68(4)	9.02(2)	5.15(2)	2.05(4)	3.63
3	1.55(0)	7.47(3)	5.16(2)	2.45(2)	-	-
4	8.05(-1)	5.16(3)	3.18(2)	1.72(2)	-	
5	2.38(-1)	2.14(2)	2.00(1)	7.01(0)	1.20(3)	8.39
6	1.42(-1)	8.13(1)	8.85(0)	1.69(0)	6.29(1)	2.02
7	1.92(-1)	4.78(1)	6.66(0)	3.15(0)	6.24(2)	16.5
8	1.34(-1)	3.90(1)	6.67(0)	6.14(-1)	5.12(2)	18.1
x,y - Plane						
1	5.94(0)	-	2.72(3)	1.48(3)	1.03(4)	1.12
2	3.49(0)	2.47(4)	1.33(3)	7.27(2)	-	
3	1.65(0)	8.98(3)	5.65(2)	3.09(2)	-	
4	9.00(-1)	5.58(3)	3.79(2)	1.99(2)	2.75(3)	1.42
5	2.34(-1)	2.51(2)	2.09(1)	4.02(0)	-	
6	1.61(-1)	8.45(1)	9.11(0)	4.18(0)	-	
7	2.11(-1)	5.02(1)	6.80(0)	1.16(0)	1.01(2)	11.8
8	1.28(-1)	4.20(1)	-	8.37(-1)	-	
		Configuration 2				
x,z - Plane						
1	2.64(0)	8.45(3)	5.53(2)	3.35(2)	6.06(2)	1.12
2	1.53(0)	2.94(3)	2.32(2)	1.44(2)	8.66(2)	1.51
3	9.06(-1)	1.46(3)	1.22(2)	6.96(1)	5.77(2)	1.48
4	4.53(-1)	9.24(2)	8.41(1)	4.81(1)	4.12(2)	1.50
5	1.40(-1)	6.09(0)	6.41(0)	2.59(0)	7.03(1)	1.72
6	8.49(-2)	2.28(1)	2.13(0)	-	1.16(2)	3.28
7	1.15(-1)	1.28(1)	-	-	5.86(1)	2.62
8	7.36(-2)	7.75(0)	-	1.13(0)	-	-
x,y - Plane						
1	2.45(0)	8.14(3)	5.09(2)	3.09(2)	-	-
2	-	1.08(3)	3.67(2)	2.22(2)	-	-
3	1.00(0)	2.42(3)	2.03(2)	1.23(2)	-	-
4	5.28(-1)	1.32(3)	1.10(2)	6.64(1)	4.03(2)	1.58
5	1.28(-1)	5.81(1)	6.80(0)	-	1.64(2)	1.44
6	1.02(-1)	2.20(1)	2.85(0)	-	6.85(1)	2.32
7	1.15(-1)	1.55(1)	-	1.02(0)	8.81(1)	11.5
8	7.36(-2)	1.23(1)	1.40(0)	7.96(-1)	4.54(1)	2.30

Table 4.3-1

Heating Rates Calculated from Boil-Off Data

Liquid Level (in.)	Liquid Volume (gal)	Reactor Power (Mw)	Heat Input				Run Number
			Ambient Heat Leak (watts)	Total Input (watts)	Total Less Amb. (watts)	Heating Rate (watts/Mw)	
24.5	52.0	0	23.3	-	-	-	13-96
27.4	62.2	0	22.3	-	-	-	11-95
28.8	67.0	0	22.0	-	-	-	9
44.1	120.3	0	23.8	-	-	-	10-94
45.7	125.5	0	26.0	-	-	-	8
			Configuration 1				
18.0	29.7	1.964	21.4[a]	554	532	271	10(7-1)-106
27.4	62.2	2.0	22.6[a]	685	662	331	10(3-1)-105
32.3	79.4	1.56	23.3[a]	594	571	366	10(5-1)-105
43.7	118.5	1.0	24.8[a]	428	403	403	10(8-1)-105
			Configuration 2				
18.0	29.7	2.07	21.4[a]	302	281	136	10(7-2)-105
25.3	55.0	2.05	22.4[a]	403	381	186	10(3-2)-105
32.3	79.4	1.54	23.3[a]	327	304	197	10(5-2)-105
44.7	122	5.725	24.9[a]	1192	1167	204	12-103

[a]Interpolated value from plot of ambient-heat-leak data.

Table 4.3-2

Heating Rates Calculated from Pressurization-Temperature Data

Liquid Level (in.)	Liquid Weight (lb)	Δt (min)	ΔT (°R)	C_s $\left(\frac{\text{Btu}}{\text{lb-°R}}\right)$	Ambient Heat Leak (watts)	Heating Rate (watts/Mw)	Run No.
26.2	33.8	59.0	1.14	2.43	27.9	-	9
40.7	63.4	50.0	0.7	2.40	37.4	-	8
			Configuration 1				
16.4	14.3	19.01	5.72	2.58	22.8[a]	128	11-92
40.7	61.5	26.93	3.86	2.71	37.4	273	10-89
43.7	69.5	4.94	0.64	2.38	39.8[a]	338[b]	10(8-1)-105
43.7	69.1	10.2	2.45	2.55	39.8[a]	335[c]	10(8-1)-105
			Configuration 2				
25.3	32.2	8.33	1.9	2.44	27.4[a]	141	10(3-2)-105
27.4	36.5	39.09	7.25	2.74	28.5[a]	117	13-93
35.4	52.2	44.02	7.03	2.66	33.6[a]	127	12-90

[a]Estimated from Runs 8 and 9

[b]Reactor power level = 1.0 Mw

[c]Reactor power level = 2.1 Mw

5. CONCLUSIONS

This report, in conjunction with Volume II, presents a comprehensive collection of data that should prove valuable in evaluating methods for calculating nuclear-radiation-energy deposition rates and the resultant temperature distributions in liquid hydrogen in a pressurized tank. Data in some categories, the first of their kind, will have some limitations in applicability, as noted in Section 4. No major difficulties were encountered in the performance of the experiment, although minor problems occasionally prevented acquisition of data with the desired precision.

The nuclear measurements and calculations provided data to determine heating gradients in the liquid hydrogen and to determine the contributions of neutron interactions and gamma interactions to the total heating rates. The C-17 calculations, which were originally performed to plan reactor power levels for the various data runs, agreed well with the measured data. The calculations performed with COHORT, using Monte Carlo techniques, were performed as a rough evaluation of the code and the results of these calculations were encouraging.

The results of these nuclear calculations give a measure of confidence to previously performed calculations with regard to nuclear-rocket-system design studies. However, the question of how well these methods can be applied to a full-scale system, where calculation of deep-penetration by nuclear radiation is required, have not been completely answered. Small discrepancies

in the calculations performed here can become rather large in deep-penetration calculations.

The presence and quantity of energy-storage mechanisms could not be determined from the attempted measurements. The energy stored by such phenomena was less than the error involved in the attempted measurements. A specially designed, laboratory-type experiment will probably be required to determine what fraction of the energy deposited by nuclear radiation in liquid hydrogen is stored temporarily through the disassociation and excitation of H_2 molecules.

No analysis of the resultant temperature distributions in the liquid hydrogen was performed. However, background information and accuracy of the data required to perform and evaluate an analysis of the self-pressurization and flow runs have been provided.

APPENDIX A

EXPERIMENTAL EQUIPMENT

The experimental equipment was designed to facilitate quick access to the ASTR in the event repairs became necessary. Quick disconnects on all pipes and wiring going to the dewar and liner tank made it possible to remove them as one unit. The test area was shielded from radiation by portable shields that could be easily removed. Removal of this shielding was necessary when access to the dewar was required for changing radiation detectors and temperature thermometers inside the dewar.

Data readout systems and control instrumentation were installed in portable racks and checked out in the Nuclear Instrumentation Laboratory. This method made it possible to check calibrations and operational functions of this equipment prior to installation in the control room.

By using these methods, a minimum time in the test area was required for setup and checkout of equipment, and more efficient utilization of the test area was obtained.

The experimental hardware and safety equipment were manufactured and/or purchased by GD/FW. The cryogenic system was designed and manufactured by Cryogenic Engineering Company of Denver, Colorado, to specifications furnished by GD/FW.

A-1 Facility Equipment

To adapt the basic configuration of the ASTR system to the experiment, some additional hardware was required. This consisted of a spacer tank, liner tank, and shielding; these

were integrated into the existing ASTR system. This equipment has been pointed out in Figure 2.1-1.

A-1.1 ASTR

Briefly, the 10-Mw ASTR is a heterogeneous, light-water-moderated and -cooled reactor containing MTR-type fuel elements. Each element contains 150 gm of U-235. Further details of the ASTR are given in Reference 7.

A-1.2 Spacer Tank

The spacer tank was designed to deepen the ASTR pit to provide two feet of water shielding between the reactor pressure vessel and the bottom of the liner tank with the ASTR in its completely lowered position. This water shielding was particularly necessary in that it allowed work, such as the positioning and retrieval of radiation detectors and the positioning of thermometers in the dewar, to be performed above the dewar.

Two 12-in. I-beams built into this tank extended through the walls and rested on four screw jacks that transferred the load to the concrete ramp. The liner tank and additional shielding were supported by the two I-beams.

A-1.3 Liner Tank

The liner tank in the water-filled ASTR pit proveded space in which the dewar could be positioned directly over the reactor. The liner tank also supported and aligned the dewar in the proper position. This method of supporting the dewar provided sufficient space between the wall of the dewar and liner tank for positioning and removing radiation detec-

tion foils on the outside wall of the dewar. Figure A-1 shows the top of the liner tank with the dewar and work platform in position and the shielding removed. During the test operations, the liner tank was sealed, thus allowing the space around the dewar to be purged with gaseous nitrogen. The tank was constructed of 1/4-in. aluminum and was 44 in. in diameter. The inside surface of the tank was coated with a 1/16-in.-thick mixture of epoxy and boron carbide. The boron in this coating absorbed slow neutrons and thus reduced the activation of the dewar.

A-1.4 Shielding

In addition to the water around the liner tank, neutron and gamma shielding were required above the liner tank and dewar during reactor operation to maintain tolerable radiation levels in the surrounding areas. This shielding was removable to allow easy access to the hydrogen tank and reactor. An exploded view of this shield arrangement is shown in Figure A-2. A gamma shield of 1- to 2-in.-thick steel was placed on the I-beams of the spacer tank. The bottom of the steel slab was coated with 1/16 in. of the same epoxy and boron-carbide mixture used in the liner tank to reduce the thermal neutrons and activation of this shield. The neutron shield was a 9-ft-diam water-filled steel tank positioned on top of the gamma shield. The tank was filled to about the 8-ft level during reactor operations.

A-2 Cryogenic System

This system consisted of the dewar, liquid-flow system,

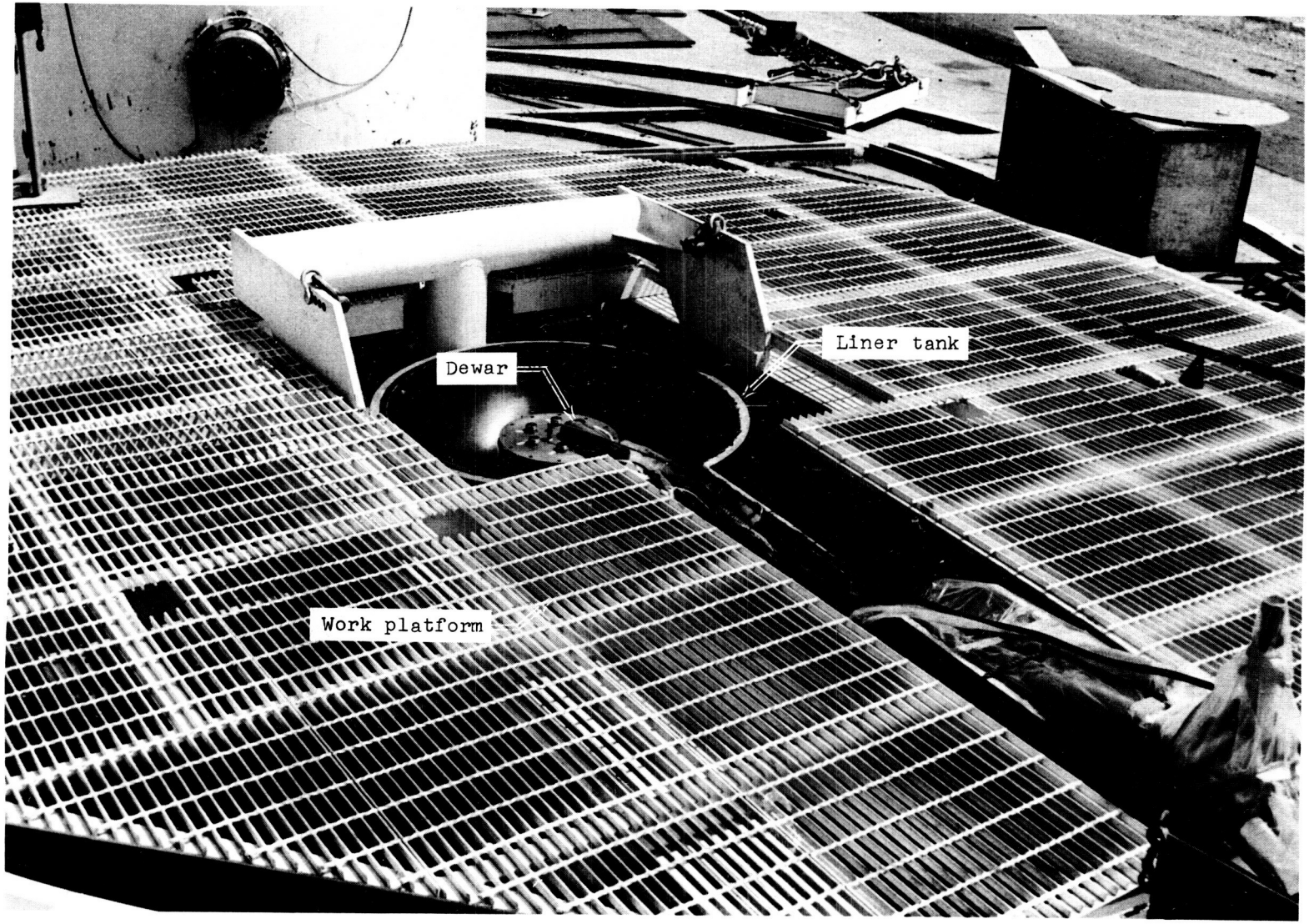

NPC 20,710
31-7337

Figure A-1 Dewar and Liner Tank Installation

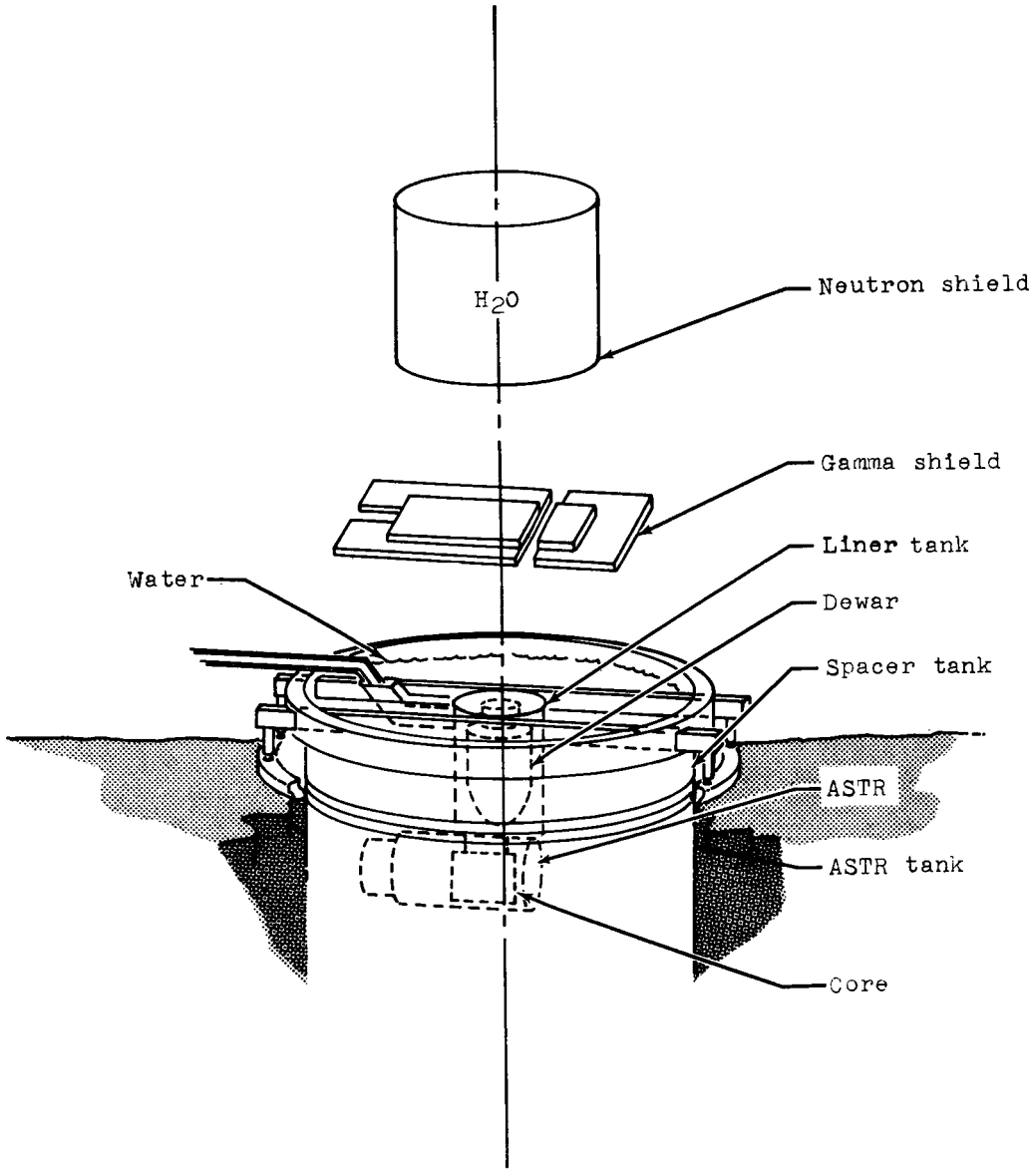

Figure A-2 ASTR Shielding Geometry

gas-flow system, and all the plumbing, valves, regulators, safety devices, and gages necessary to operate, control, protect, and monitor the dewar during the experiment. Figure A-3 is a more detailed diagram of the system than that shown in Figure 2.2-1. Only the most pertinent parts, however, are discussed below.

A-2.1 Dewar or Hydrogen Tank

The dewar was manufactured of 304 stainless steel and had the capacity of a 125-gal tank with a 10% ullage, or vapor space. The shape, size, and thickness of material for various sections of the dewar and dewar-reactor geometry are shown in Figures A-4 and A-5. A photograph of the tank as it appeared after the experiment is shown in Figure A-6. One inch of super insulation was used between the inner and outer walls. This insulation consisted of alternate layers of glass paper and aluminum foil. The space between the dewar walls was evacuated to 10^{-4} mm Hg, and the vacuum connection was sealed off. A vacuum gage was mounted on the neck of the dewar at a penetration of the outer wall. This gage was monitored during the experiment to ensure that the vacuum was maintained.

The dewar neck had a 12-in. inside diameter for installation and removal of radiation detectors and temperature-measuring devices. The opening was covered with a 3/4-in.-thick stainless-steel lid which sealed with a Buna N O-Ring. Lead-throughs were provided in the lid to accommodate 120 wires for platinum-resistance thermometers, 10 leads for thermocouples, and 20 leads for hydrogen-level indicators. Also, a lead-

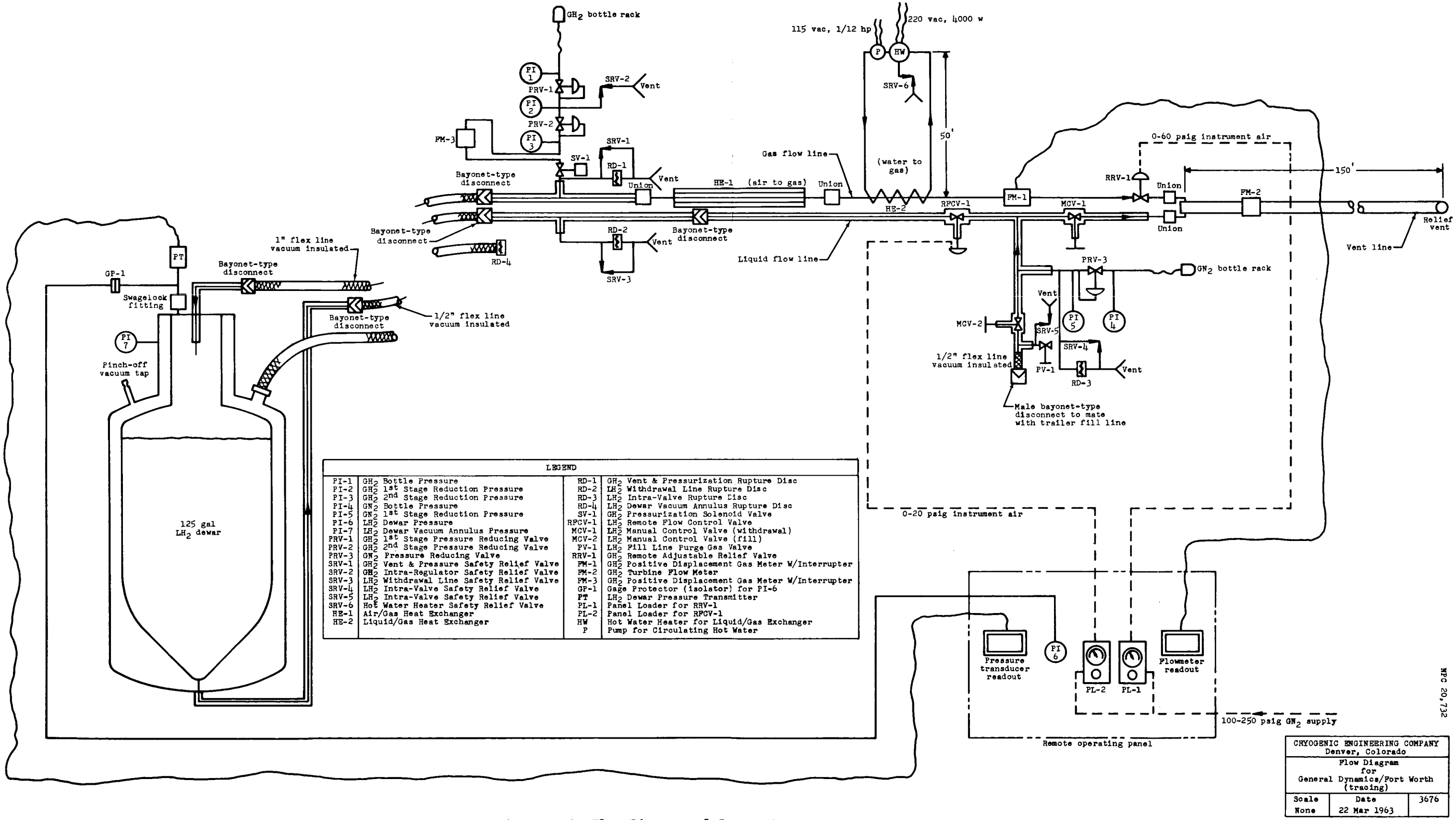

LEGEND			
PI-1	GH_2 Bottle Pressure	RD-1	GH_2 Vent & Pressurization Rupture Disc
PI-2	GH_2 1st Stage Reduction Pressure	RD-2	LH_2 Withdrawal Line Rupture Disc
PI-3	GH_2 2nd Stage Reduction Pressure	RD-3	LH_2 Intra-Valve Rupture Disc
PI-4	GN_2 Bottle Pressure	RD-4	LH_2 Dewar Vacuum Annulus Rupture Disc
PI-5	GN_2 1st Stage Reduction Pressure	SV-1	GH_2 Pressurization Solenoid Valve
PI-6	LH_2 Dewar Pressure	RPCV-1	LH_2 Remote Flow Control Valve
PI-7	LH_2 Dewar Vacuum Annulus Pressure	MCV-1	LH_2 Manual Control Valve (withdrawal)
PRV-1	GH_2 1st Stage Pressure Reducing Valve	MCV-2	LH_2 Manual Control Valve (fill)
PRV-2	GH_2 2nd Stage Pressure Reducing Valve	PV-1	LH_2 Fill Line Purge Gas Valve
PRV-3	GN_2 Pressure Reducing Valve	RRV-1	GH_2 Remote Adjustable Relief Valve
SRV-1	GH_2 Vent & Pressure Safety Relief Valve	FM-1	GH_2 Positive Displacement Gas Meter W/Interrupter
SRV-2	GH_2 Intra-Regulator Safety Relief Valve	FM-2	GH_2 Turbine Flow Meter
SRV-3	LH_2 Withdrawal Line Safety Relief Valve	FM-3	GH_2 Positive Displacement Gas Meter W/Interrupter
SRV-4	LH_2 Intra-Valve Safety Relief Valve	GP-1	Gage Protector (isolator) for PI-6
SRV-5	LH_2 Intra-Valve Safety Relief Valve	PT	LH_2 Dewar Pressure Transmitter
SRV-6	Hot Water Heater Safety Relief Valve	PL-1	Panel Loader for RRV-1
HE-1	Air/Gas Heat Exchanger	PL-2	Panel Loader for RPCV-1
HE-2	Liquid/Gas Heat Exchanger	HW	Hot Water Heater for Liquid/Gas Exchanger
		P	Pump for Circulating Hot Water

CRYOGENIC ENGINEERING COMPANY Denver, Colorado		
Flow Diagram for General Dynamics/Fort Worth (tracing)		
Scale	Date	3676
None	22 Mar 1963	

Figure A-3 Flow Diagram of Cryogenic System

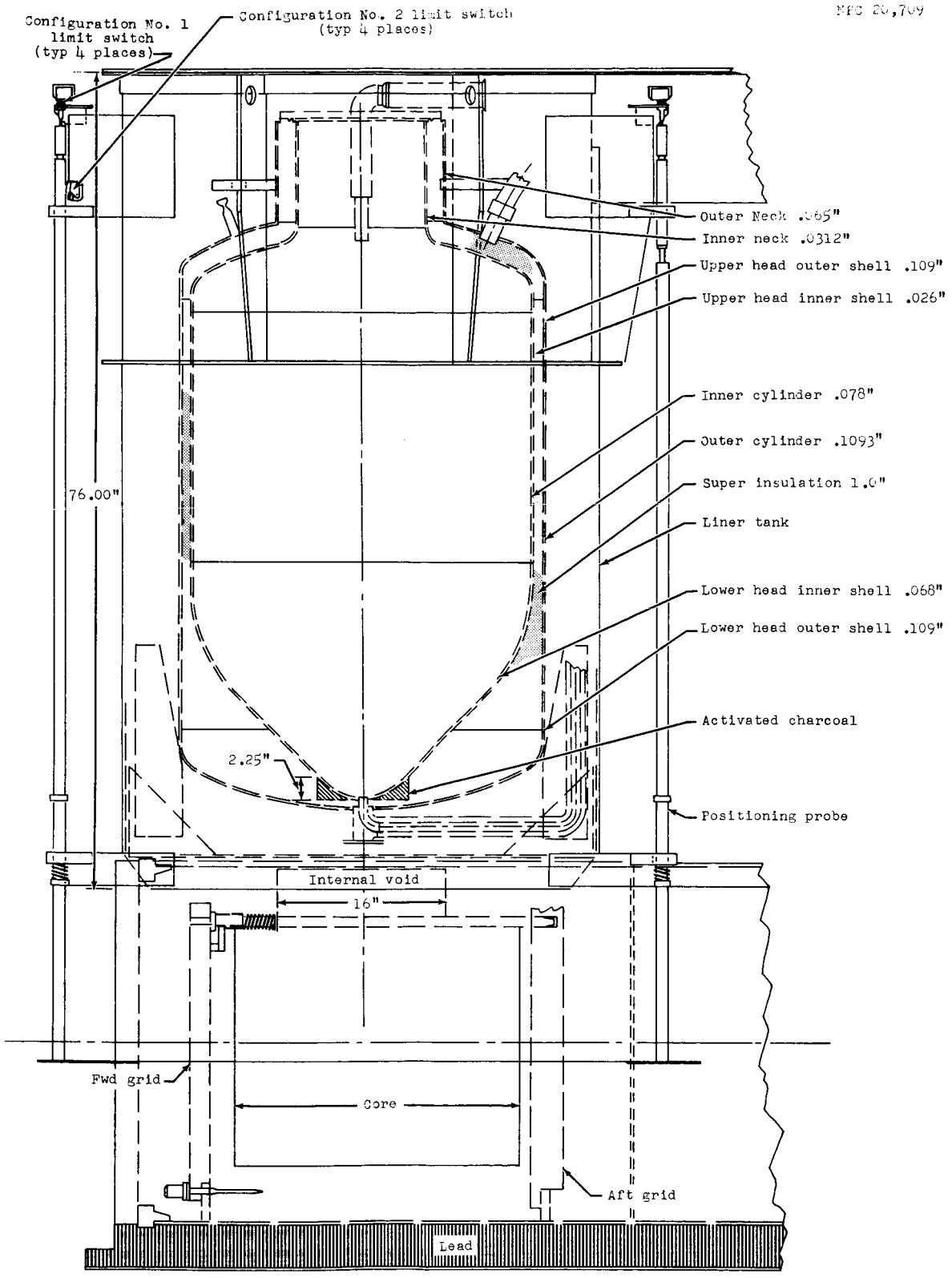

Figure A-4 Dewar Dimensional Data

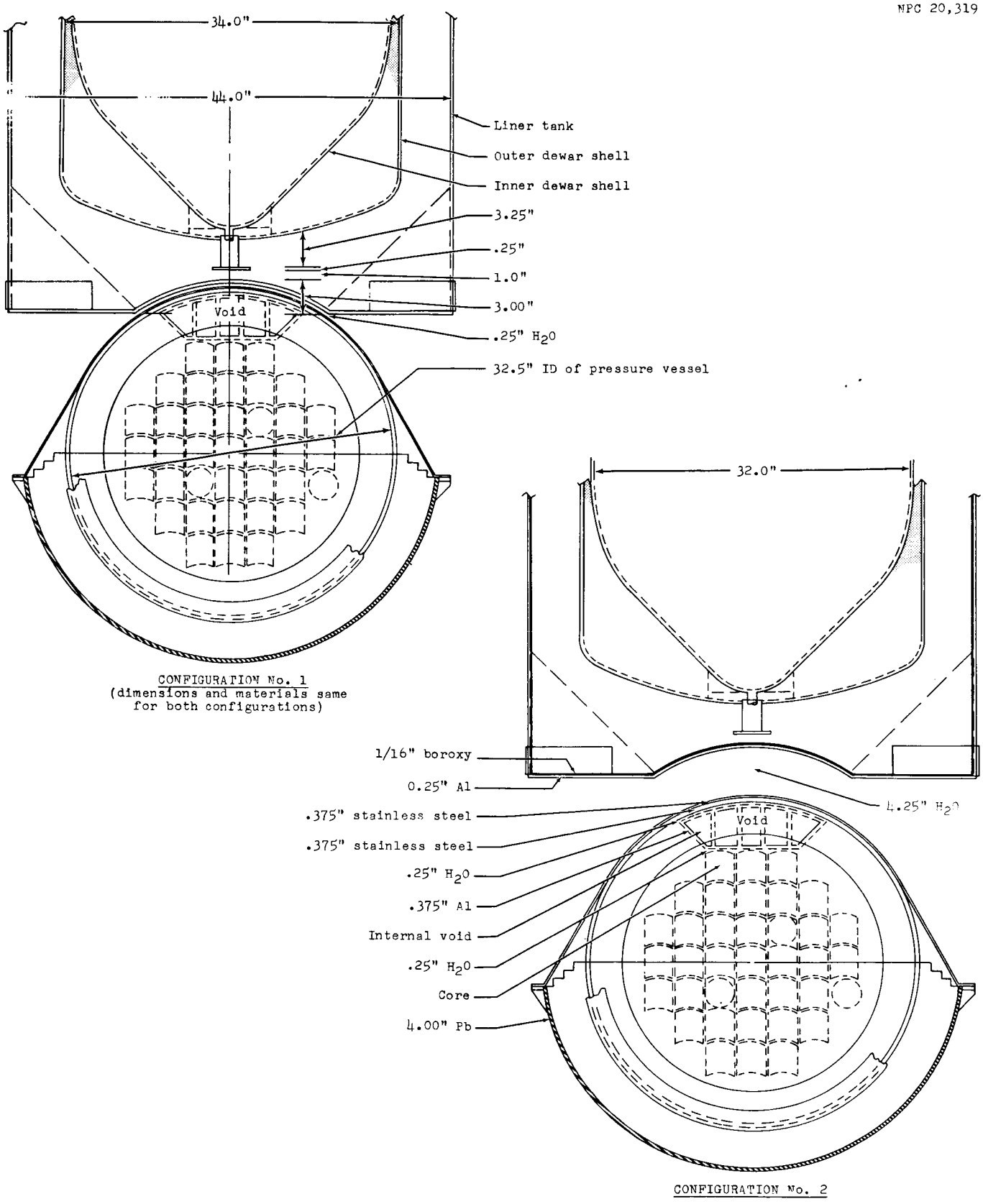

Figure A-5 Dewar-Reactor Dimensional Data

NPC 20,711
31-7380

Figure A-6 Hydrogen Heating Experiment Dewar

through was provided in the lid for connecting a pressure transducer.

A-2.2 Liquid-Flow System

The main components of the liquid-flow system were the main flow line, the system fill line, the purge system, and the valves. The main flow line was a 1/2-in. vacuum-jacketed line. This line entered the dewar from the bottom and terminated flush with the inner wall. From the bottom of the dewar it extended up the outside of the dewar for six feet and connected with a bayonet fitting to a section of 1/2-in. flex line. The flex line exited through the liner-tank duct and connected to a 50-ft section of structural vacuum-jacketed line. A remotely controlled flow-control valve (RFCV-1) was installed 18 in. from the end of this line. This valve controlled the flow of liquid hydrogen during filling and emptying of the dewar. The valve operator was a spring-to-close, air-to-open type and was positioned by means of a remotely located, panel-mounted hand loader with pressure gage.

The system fill line tied into the main flow line nine inches from the upstream end with a rigid section of 1/2-in. vacuum-jacketed line followed by a 5-ft section of vacuum-jacketed flex line. The flex line was terminated with a female section of a 2.0-in. bayonet-type disconnect which connected the LH_2 supply trailer to the experimental system. The rigid section of this line had an insulated hand-operated valve installed 16 in. from the liquid-hydrogen line to facilitate filling of the dewar.

A helium purge system was tied into the liquid-hydrogen fill line between the hand valve and the supply dewar. This system was used to purge the liquid-hydrogen fill line back through the supply-trailer vent.

A nitrogen purge system tied into the hydrogen fill line between the hand valve and the liquid-hydrogen line. The N_2 purge gas was supplied from a bank of compressed-gas bottles. The regulation of the GN_2 purge was accomplished by a single-stage pressure-reducer valve (PRV-3) having an adjustable outlet range of from 10 to 75 psig.

The manual-control valves (MCV-1 and MCV-2) were used in routing the liquid hydrogen during filling and emptying operations.

Rupture discs and safety relieve valves were used in all sections of the system to guard against overpressures.

A-2.3 Gas-Flow System

The gas-flow system consisted chiefly of sections of vacuum-jacketed line, a pressurization system, heat exchangers, flow-meters, and a remotely controlled relief valve. A 1-in. vacuum-jacketed line entered the dewar through the lid and extended into the dewar to within six inches of the 125-gas liquid level. The line was terminated inside the dewar with a gas diffuser to obtain even distribution of the pressurization gas. External to the dewar, this line connected to an 8-ft section of vacuum-jacketed flex line which connected to a 10-ft section of standard 1-in. vacuum-jacketed line.

Two heat exchangers were installed in series at the end

of the vacuum-jacketed piping to warm up the boil-off gas before it entered the gas meter.

The first heater was an air/gas heater consisting of a 14-in.-diam coil of 1-in. insulated copper tubing. This heater raised the temperature of the boil-off gas to about -317°F.

The second heater was a liquid/gas heater consisting of a 1-in.-diam copper pipe with a 2-in.-diam water jacket outside. Water at ambient temperaturature (hot water) was flowed through this jacket against the gas flow in the inner pipe. This heater raised the gas temperature to above 20°F.

The gas meter (FM-1), which followed the heat exchangers in the gas flow line and which was used to measure the boil-off gas, is described in Appendix B.

Following the flowmeter and at the end of the gas line was a remotely controlled relief valve (RRV-1). This valve was used to control the pressure on the entire system from atmospheric to about 60 psia. The valve relieved into the vent system. The valve was controlled by means of a remotely located, panel-mounted hand-loader provided with pressure gage.

The hydrogen pressurization system used to maintain pressure in the dewar during the flow runs was tapped into the gas-flow line with a 1/4-in. stainless-steel tube which in turn connected to the outlet side of a gas meter (FM-3). The gas-meter inlet was attached to the pressure-reducing system, which was adapted to a bank of GH_2 supply bottles.

The pressure-reducing system consisted of a series of

gages and pressure-reducing valves. The regulation was accomplished in two stages to reduce the regulator lag associated with a variable inlet pressure, thus ensuring good pressure control. The first-stage regulator (PRV-1) was a pressure-reducing valve[i] with an adjustable outlet range of 100-225 psig. The second-stage regulator (PRV-2) had an adjustable outlet range of from atmospheric to 60 psia.

A-2.4 Vent Line

The liquid- and gas-flow systems were connected to a 4-in.-diam vent line. This line extended an additional 150 ft from the test facility so that the GH_2 would be vented to the atmosphere at a safe distance from the facility. A vent stack, which rose to 30 ft above the ground, was installed on the end of this line to further meet safety requirements for venting GH_2 to the atmosphere. A poppet valve was installed on the top of the vent stack. This valve was designed to maintain about 0.5 psi on the system at all times and to prevent rain from entering the vent stack. A turbine-type meter was installed in the 4-in. vent line 90 ft from the end of the vacuum-jacketed liquid flow line. This gas meter monitored total flow of gas from the system during LH_2 flow runs.

APPENDIX B

INSTRUMENTATION

Descriptions of the instrumentation systems and techniques used to obtain the required data for the experiment are presented in this appendix. The order of the presentation is listed below with the appropriate section noted.

B-1 Cryogenic-Temperature Measurement

B-2 Ambient-Temperature Measurement

B-3 Pressure Measurement

B-4 Flow Measurement

B-5 Liquid-Level Measurement

B-6 Radiation-Intensity Measurement

Measurement accuracy is discussed within each section under a subsection entitled "Performance," with the exception of Section B-6, where the discussion on this topic is integrated with the descriptive information.

In addition to the equipment needed to obtain data, other equipment was utilized to facilitate performance of the test and to meet safety requirements. A dual-camera, dual-monitor, closed-circuit television system was used for visual observation of the test apparatus. Five channels of a hydrogen detection system were used to monitor for hydrogen leaks. A float-operated, switch-type circuit was used to detect leakage of water into the liner tank around the dewar. With the exception of the television system, all electrical power to systems furnishing power or deriving signals from the test setup was routed through a contactor unit actuated by a switch on the

test control panel. A CO_2 system with exhausts at critical locations was controlled from the test control panel.

Simplified diagrams of the various systems are shown in Figures B-1 and B-2.

Signal and excitation leads were 20AWG, 2-conductor-shielded, insulated wires grouped into four bundles. The thermocouple extension harness was a 24-pair, 22AWG, shielded, insulated cable. Lead-wire lengths were approximately 350 ft.

In order to minimize noise, shields on all low-level circuits were earth-grounded at the dewar location and were floated elsewhere.

AC power to the pressure transducer and a solenoid valve was supplied through dc-actuated contactors located in the vicinity of the test setup.

Harnesses for circuits into the dewar were terminated with 24-pin connectors which mated with bulkhead connectors in the dewar lid.

B-1 Cryogenic-Temperature Measurement

B-1.1 Sensors

Thirty platinum-resistance thermometers were used in measuring temperatures in the liquid-hydrogen range. These thermometers, Rosemount Engineering Company (REC) Model 146AF, have an R_o (ice-point resistance) of 1000 $\pm$ 1 ohms and a re-

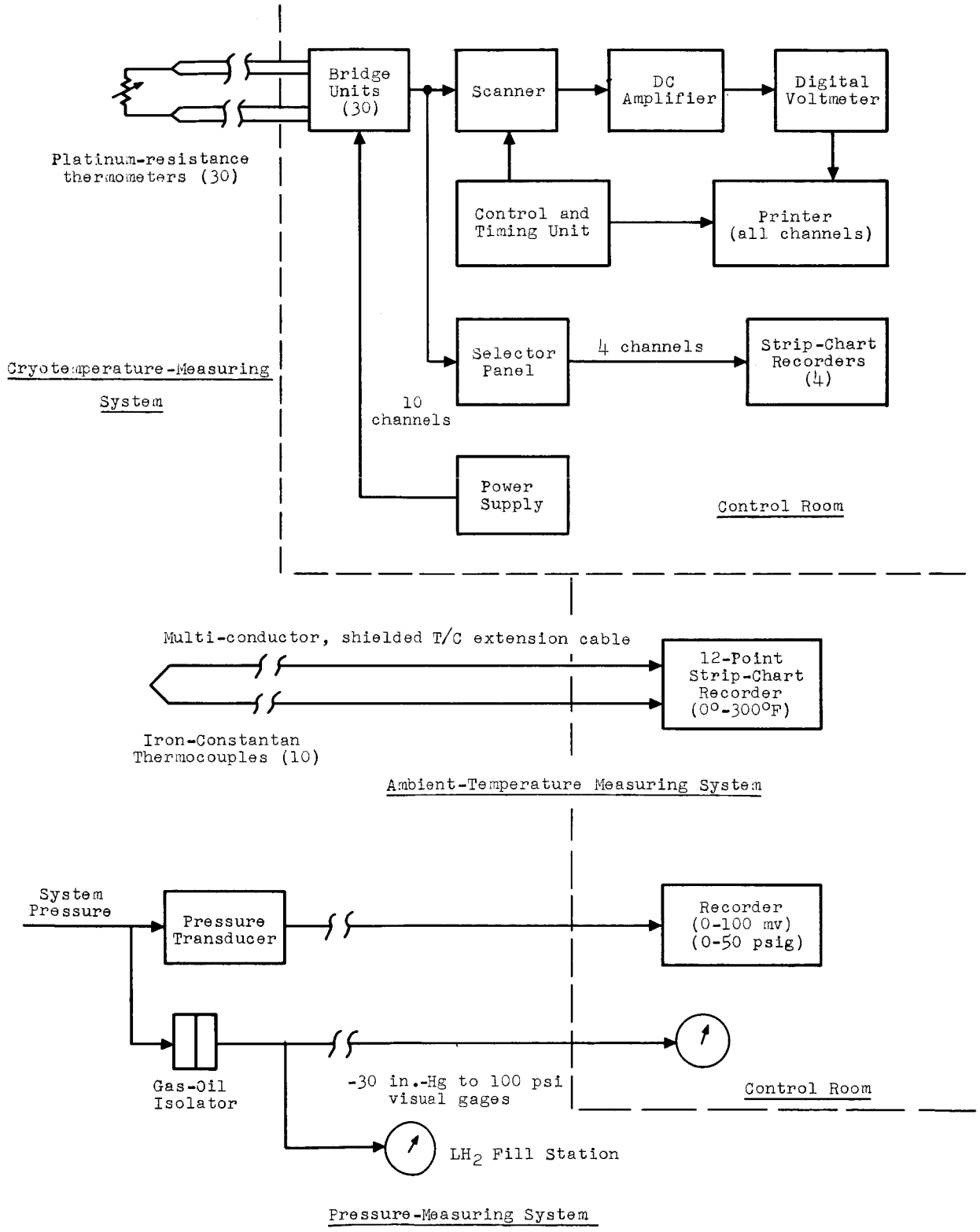

Figure B-1 Temperature- and Pressure-Measuring Systems

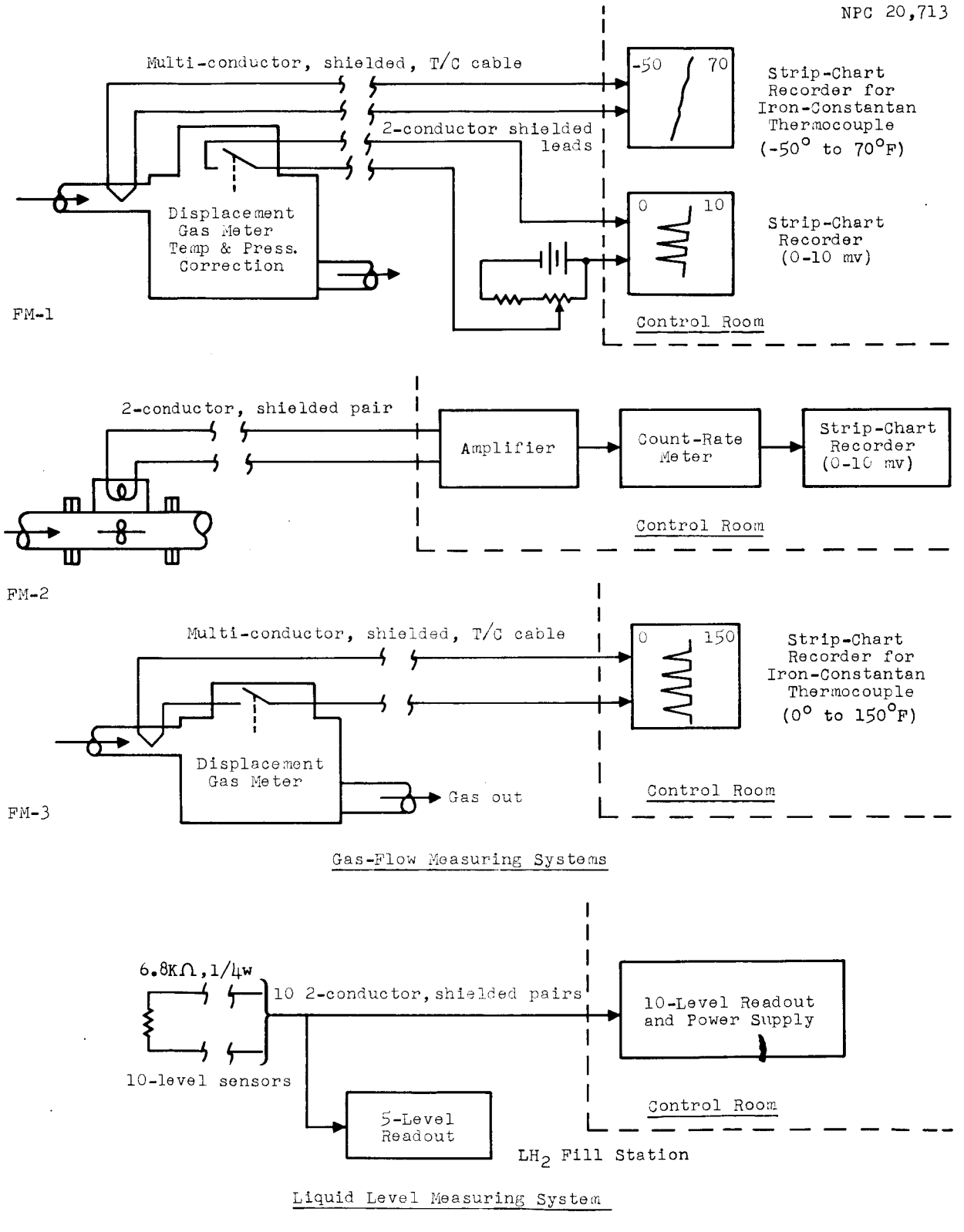

Figure B-2 Gas-Flow and Liquid-Level Measuring Systems

sistance of~5.4 ohms at -423°F. Given below are pertinent specifications quoted from Rosemount Engineering Company Specification DWG 146AF (Instruction Manual: Triple-Bridge Multi-Channel Temperature Measurement System; REC Document 56329A, 29 May 1963).

2.0 DESIGN AND PERFORMANCE

2.1 Temperature Range: -435°F to +700°F.

2.2 Resistance-Temperature Relationship: The nominal resistance vs temperature shall be as tabulated below.

2.3 Accuracy: Each sensor shall be accurate to within ± 0.10°F in the range -435°F to +32°F and accurate to within ± 0.5°F in the range +32°F to +700°F.

2.4 Stability: Each sensor shall be repeatible to within ± 0.10°F in the range -435°F to 32°F and repeatible to within ± 0.5°F in the range +32°F to +700°F.

2.5 Calibration: Each sensor shall be calibrated at +32°F, LN_2, LHe, and 212°F. These values shall be used to calculate the sensor resistance at each of the other points tabulated, below, using the "Corruccini 3-point" method.

2.6 Time Constant: Less than 4.0 seconds for 63.2 percent of the total response to a step function of temperature in agitated LN_2.

2.7 Self-Heating: In agitated LN_2, an I^2R power of 5.0 milliwatts shall cause a sensing element error of not more than 1.0°F.

2.8 Materials: The sensor is composed of platinum, platinum-rhodium, and a ceramic composed of metal oxides.

3.0 INDIVIDUAL TESTS: Each sensor shall be examined

for good workmanship, conformance to this drawing, and calibrations as defined in Spec. 2.5 above.

Temperature (°F)	Resistance (ohms)	Interchangeability Tolerance (± ohms)
(data omitted for temperatures above 32°F)		
+32	1000.0	1.0
0	929.09	-
-100	704.84	-
-200	475.39	-
-300	238.43	-
-400	24.690	-
-410	13.920	-
-420	6.870	-
-435	2.233	-

The thermometers were installed on a positioning rig as shown in Figure B-3. Details of individual installations are shown in Figures B-4 and B-5. Dual leads were used between the bulkhead connector in the dewar lid and each of the thermometers. Four lead wires for each thermometer were used from the connector to the control room. Lead wires inside the dewar were bundled on the positioning rig and routed through one of two 60-pin connectors and thence to the bulkhead connectors. Lead wire used in the dewar was ceramic-insulated (Ceramatemp, AWG 24, code 675, Grade C), made by Hitemp Wires Inc., of Westbury, N. Y. Insulation resistance between individual wires in the bundle ranged from 5 to 10 megohms. (Measurements were made in air at 75°F, with 35% relative humidity.) Conductor resistance measured at 75°F was 0.042

NPC 20,971
31-7544

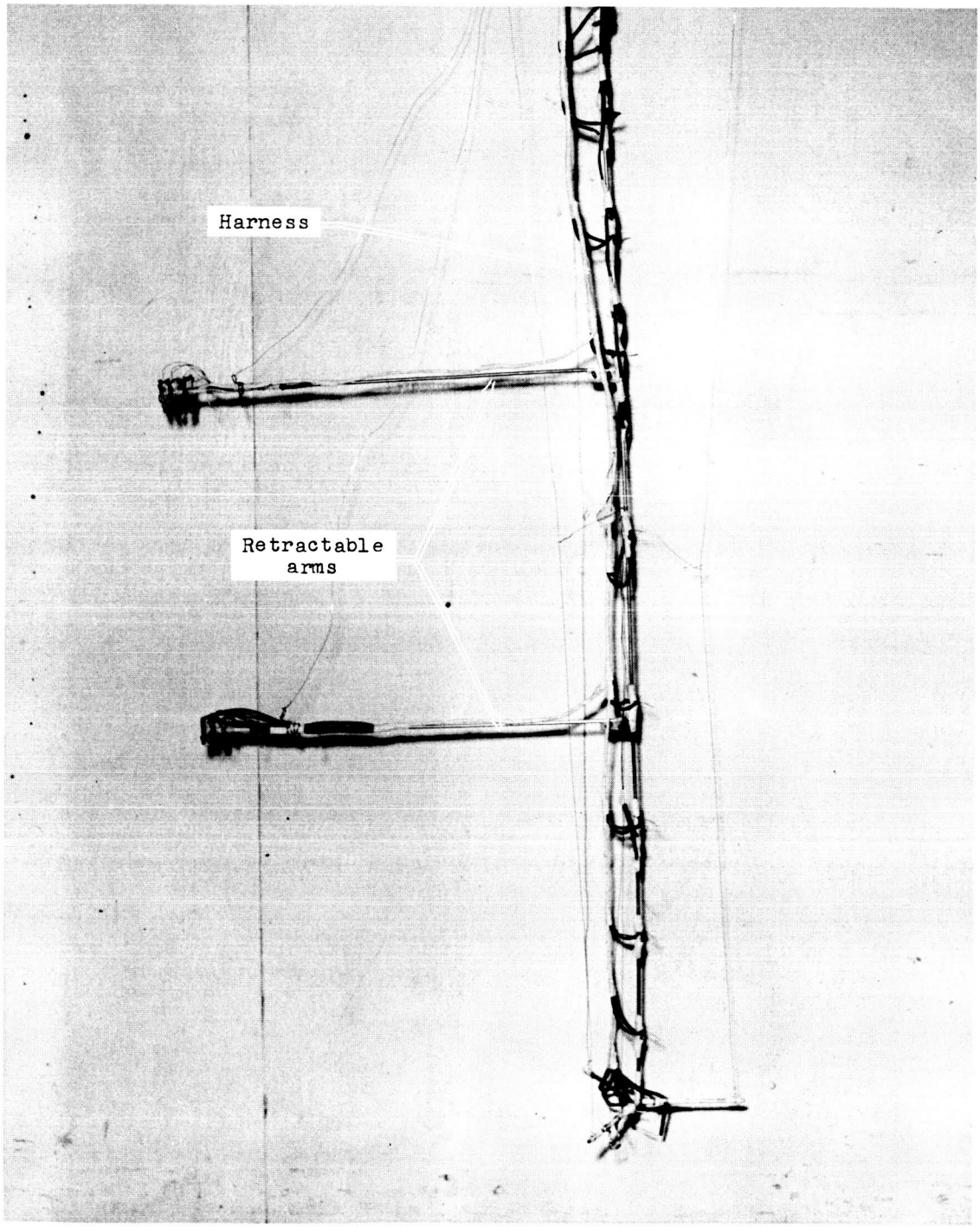

Figure B-3 Thermometer Positioning Rig

NPC 20,969
31-7543

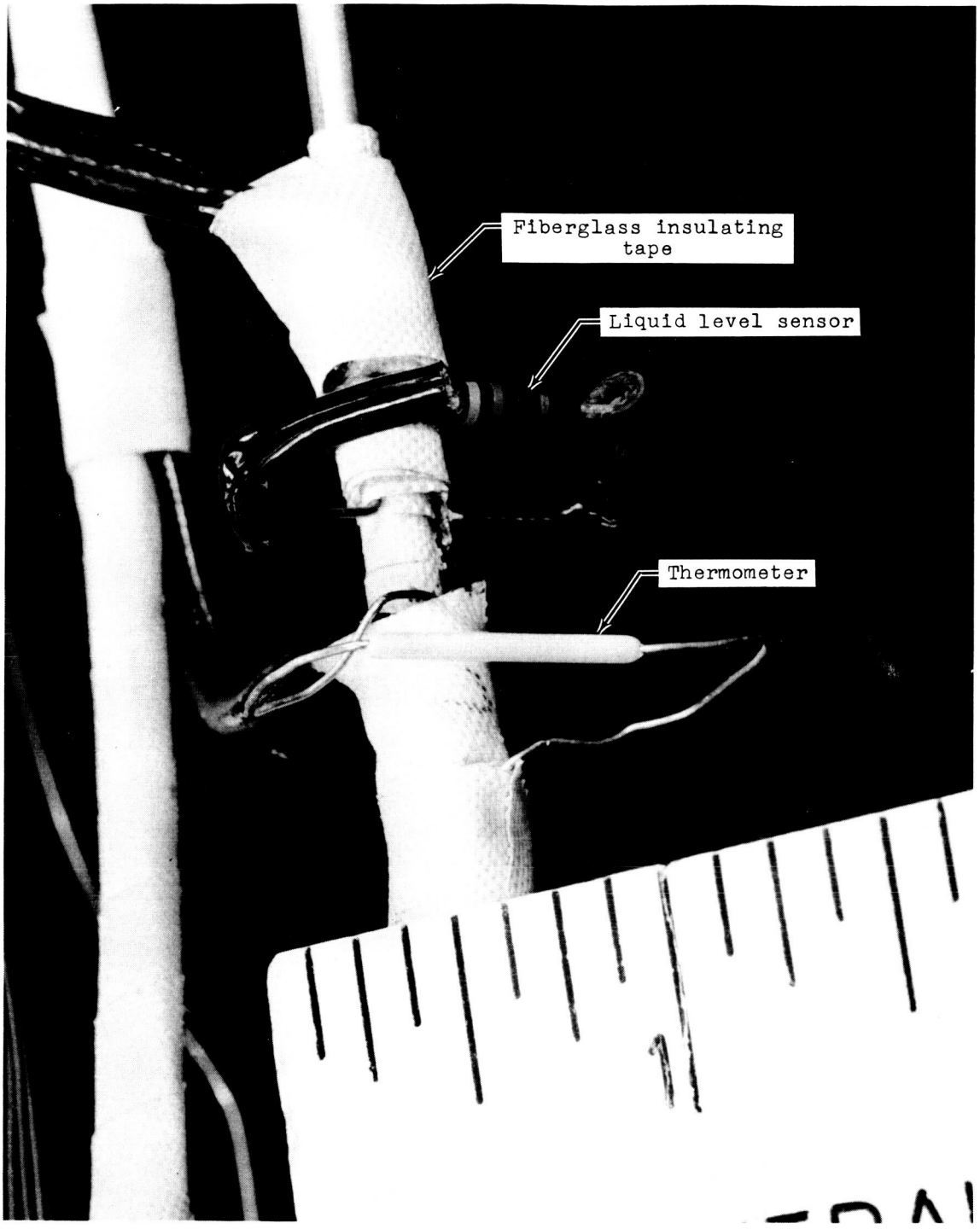

Figure B-4 Individual Thermometer and Liquid-Level-Sensor Installations

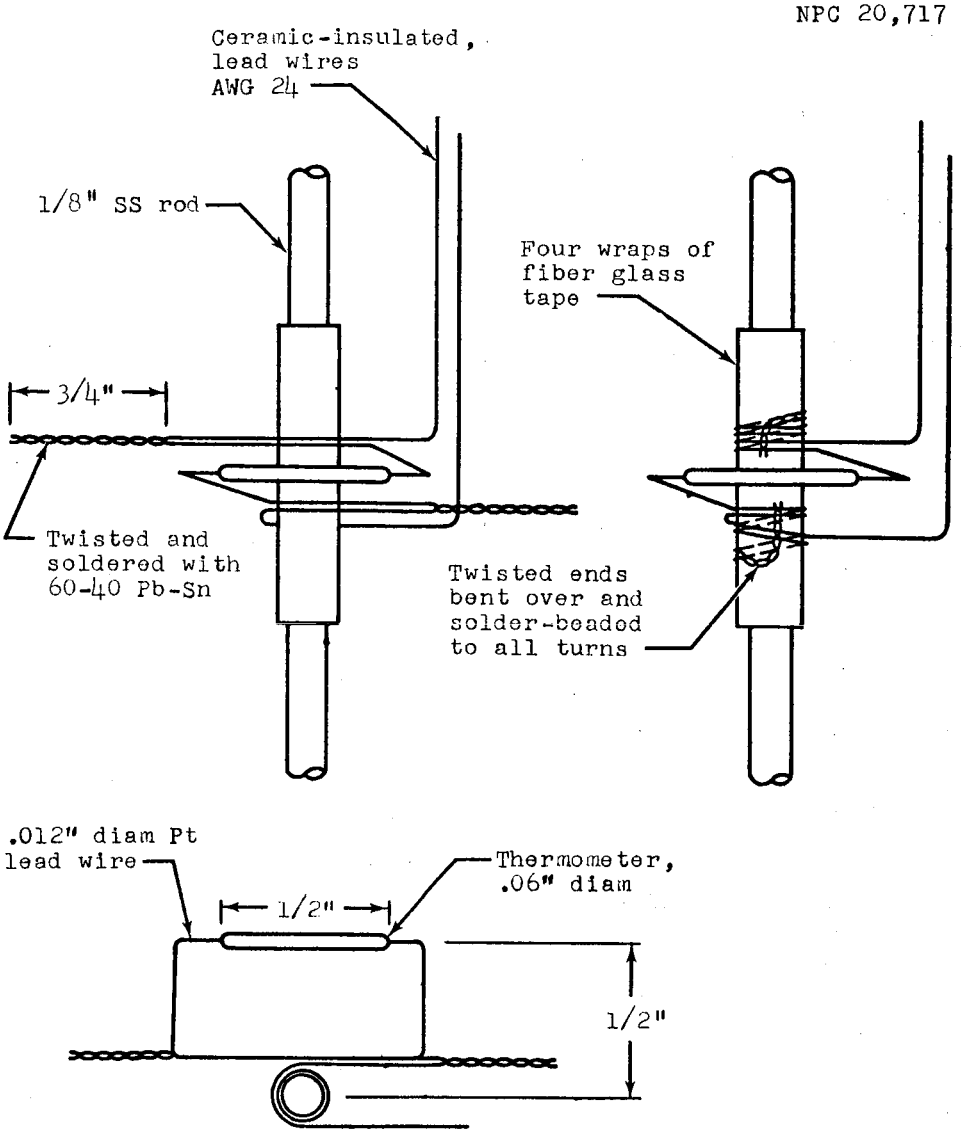

Figure B-5 Thermometer Mounting Procedure

ohm/ft. Resistance at LH_2 temperatures was estimated to be of the order of 0.00042 ohm/ft, since the resistivity of copper decreases by approximately a factor of 100 between the two temperatures.

B-1.2 System

Bridge circuits used with the thermometers were REC Model 551B mounted in REC's Multiple Triple Bridge Unit, 550AC. These adjustable bridges were designed to yield outputs ranging from 60 mv at -425°F to zero milivolts at -400°F when used with the Model 146AF thermometers. These bridges were also designed to compensate for lead-wire resistances of the order of 5 ohms per lead (see Sec. B-1.4).

Excitation voltage of 30.00 ± .01 volt was supplied to the bridges by a Harrison Model 6226A power supply.

Outputs from the bridges were routed through a GD/FW-designed coaxial relay scanner which selectively fed the signals through a guarded-ground dc amplifier (Dana Laboratories Model 2200) adjusted for a gain of 100 to a digital voltmeter (Non-Linear Systems Model M-24). Signal amplitude and polarity were displayed on the digital voltmeter, and the signal, along with appropriate identification and timing data, was printed on paper tape. Sampling rate was approximately 1.7 samples per second.

In addition, 10 of the 30 bridge outputs were connected to a patch panel through which any four of these 10 channels could be patched to strip-chart recorders for continuous recording in parallel with the voltmeter system.

B-1.3 Data Processing

The temperature data recorded on printed paper tape was edited manually and punched on paper tape with a Flexowriter. The punched-tape data were transcribed and put into a different format on magnetic tape. Equipment which has subsequently become available would have permitted direct recording on magnetic tape. The taped data were then utilized as problem input data for an IBM 7090 procedure written in FORTRAN language. While the main purpose of the IBM program was to reduce or convert the measured voltages to temperatures, a secondary purpose was to utilize the sorting and printing capabilities of the computer so that the reduced output data could be printed in a form readily adaptable to final data reporting format.

For the program, the voltage-to-temperature conversion function, based on the bridge calibration curve for the range of from -400°F to -425°F and on experimental data (see Sec. B-1.4 below) for higher temperatures, was curve-fitted with several polynomial and linear equations — depending upon the sign and magnitude of the voltages. During voltage-to-temperature conversion, the taped data were tested to determine the sign (positive or negative bridge output voltage), magnitude, channel or thermometer sequence, etc. Once the sign and the magnitude of a particular voltage were determined, the appropriate coefficients for that range of the conversion function were applied to compute the temperature.

B-1.4 Calibration Procedures

On receipt of the thermometers from the vendor, resist-

ances were checked at the ice point and at the boiling point of nitrogen and found to be satisfactory (within the limitations of available test equipment). The complete system was assembled, excluding the thermometers; precision resistors of 4.998 ± .005 ohms and 24.025 ± .005 ohms were substituted in turn for each thermometer; and the bridges were individually adjusted to give the desired zero and span.

Bridge outputs at temperatures above -400°F were determined experimentally with precision resistances corresponding to thermometer resistances at four temperatures in the range of from 32°F to -400°F. This information was used in processing ullage-gas temperature data.

During the experiment, power-supply voltage, stability, amplifier gain and zero, and system noise were routinely checked and monitored.

B-1.5 Performance

Overall measurement accuracy was within the desired ± 0.2°F, as indicated by the repeatability shown by comparison of data from several thermometers from all experimental runs when referenced to existing vapor-pressure data and thermometer-bridge calibration accuracies.

Four thermometer failures occurred; in addition, difficulty due to intermittent response or drift arose with five thermometer channels. Three of the failures (Thermometers 6, 11, and 12) were characterized by obviously erroneous outputs at cryogenic temperatures, which were due to either changes in sensor characteristics or harness insulation breakdown

inside the tank. One thermometer (No. 20) was broken by contact with the vent-pipe inlet. Sampling of Thermometer Channels 1, 21, and 30 was intermittent on some runs and Channels 4 and 25 drifted excessively on some runs. However, the response of Number 25 was such that it appeared possible that the anomalous readings might be due to contact with the tank wall. Subsequent to the experiment, resistances of all thermometers except the broken one were the same ($\pm$ 1 ohm) at room temperature.

The thermometers enhibited no apparent radiation damage or significant error due to radiation heating (see below). Maximum exposures received were estimated to be 1.3×10^8 r of gamma rays, and 8.6×10^{15} n/cm^2 (E > 0.3 mev) of neutrons. Visual examination of the thermometers and harness after the experiment showed no serious changes in appearance due to environmental conditions. Photographs in Figures B-3 and B-4 were made after the experiment. Fiberglas insulating tape and polyvinyl-Fiberglas insulating sleeving showed no deterioration. Several thermometers, however, did have a slight amount of spalling of their ceramic insulation at the junctures of the lead wires and ceramic coating. This effect is barely discernible on the thermometer shown in Figure B-4 and probably resulted from a combination of stress induced during the mounting of the thermometers and thermal stresses arising during the experiment. The sensors were cycled from ambient to cryogenic to ambient temperatures approximately 30 times during the experiment.

Self-heating error appeared to be negligible, and examination of the data indicated a possible maximum error due to radiation heating and/or localized bulk-temperature anomalies of approximately +0.1°F. This estimate is based on the relative temperatures indicated by thermometers (at the bottom of the dewar and near the liquid surface) on runs where data were obtained with and without the reactor operating and with the system vented to atmosphere in both cases.

Lead-wire resistance compensation by the bridge units was not satisfactory and invalidated the bridge calibrations performed by the vendor; this necessitated recalibration by GD/FW.

Experience gained during the experiment indicated the possibility of improving measurement accuracy by using the dewar system for calibration and by making further reductions in system noise. Apparently, a lack of stratification in the dewar when vented, together with the appropriate use of temperature references, would permit more uniform adjustment of the bridges, provided that a comparable reduction in system noise can be achieved. Signal-to-noise ratio for maximum bridge output (60 mv) was approximately 1200/1 with the amplifier and approximately 120/1 without the amplifier. An accuracy of $\pm$ 0.1°F appears feasible when similar equipment is used, with a possibility of achieving $\pm$ .05°F.

B-2 Ambient-Temperature Measurement

B-2.1 Sensors

Ten iron-constantan thermocouples were used in measuring

dewar wall temperatures in order to determine nuclear heating rates.[a] The dewar was empty for this particular phase of the experiment.

Five of the thermocouples were installed inside the dewar on a positioning rig and five other junctions were permanently attached to the exterior of the dewar. Attachment was made with epoxy containing 90% by weight aluminum powder filler. In addition, two other junctions were solder-attached to the inside of the dewar neck. These two thermocouples were not used on the nuclear heating test; however, they were used to monitor dewar temperature during warmup after subsequent cryogenic portions of the experiment.

Wires from the thermocouples on the positioning rig were connected to the 22AWG extension-wire leads with dual-pin thermocouple connectors. The extension-wire leads were routed through a solder-type, feed-through header in the dewar lid to a 48-pin. thermocouple connector on the thermocouple extension cable. Leads from the five thermocouples on the outside of the dewar wall and from Flowmeters 1 and 3 were also routed through this multi-pin connector to the extension cable.

B-2.2 System

Thermocouple outputs were recorded on a multipoint Brown temperature recorder, using a standard iron-constantan chart and scale for the range 0-300°F.

---

[a]Two additional thermocouples were used in conjunction with the flowmeters. These are discussed in Section B-4.

B-2.3 Data Processing

The strip-chart-recorded data were processed manually.

B-2.4 Calibration Procedures

All junctions, including those in the flowmeters, were matched to obtain uniformity of output ($\pm$ 2°F) over the range of from 32° to 150°F. The multipoint Brown recorder was calibrated against a Leeds and Northrup Model 8693 temperature potentiometer.

B-2.5 Performance

After initial installation and checkout at the test site, with all thermometers at ambient temperature (85°F), the temperatures indicated for all thermocouples agreed to within $\pm$ 1°F. Temperature measured during the experiment ranged from 70°F to 135°F.

On the basis of the calibration and observed performance, the repeatability and measurement accuracies are cited as $\pm$ 1°F and $\pm$ 2°F, respectively.

B-3 Pressure Measurement

B-3.1 Sensors

Provisions were made for monitoring the system (dewar) pressure with a pressure transducer and visual gages. The pressure transducer (International Resistance Corporation, Model 70-2955) was coupled to the dewar through the dewar lid with an impulse line approximately 96 in. long. Pressure in the same impulse line was transmitted through an isolation diaphragm to an oil-filled line coupled to the two visual gages. One of the gages was located in the control room, and the other was located at the LH_2 fill station.

The visual gages were compound gages with a range from -30 in. Hg to 100 psig.

B-3.2 System

Output of the pressure transducer (0-100 mv, corresponding to 0-60 psig) was put through a voltage divider and monitored on a 0-10-mv Brown strip-chart recorder. Timing information was noted manually on the charts during the tests.

B-3.3 Data Processing

Pressures at appropriate time intervals were picked off the chart records and tabulated and/or replotted as required.

B-3.4 Calibration Procedures

The pressure transducer and control-room visual gage, together with the isolation diaphragm, were calibrated in the GD/FW Standards Laboratory with a 100-in. mercury manometer. During the experiment, the calibrations were checked against precision Heise gages with 0-15-psig and 0-100-psig ranges. Gage accuracies of 0.3% full scale had been established by the Standards Laboratory.

B-3.5 Performance

Repeated calibration checks indicated that measurements near zero psig (system vented to atmosphere) were accurate to $\pm$ 0.25 psi. Measurements above atmospheric pressure were accurate to $\pm$ 8% of the measurement.

Transducer output proved to be excessively temperature dependent and showed considerable hysteresis.

The fluid coupling with the visual gage proved unsatisfactory because of the inertia of the long fluid line.

During the latter part of the experiment, a 0-100-psig Heise gage was mounted on the test setup and coupled to the gas impulse line. The gage was monitored with one of the closed-circuit TV cameras, and gage readings were noted on the pressure transducer recorder chart and used as a check during data processing.

B-4 Flow Measurement

B-4.1 Meters

Gross, total hydrogen flow from the system was monitored with a turbine-type meter (FM-2) located in the vent line. Boil-off rates were measured upstream from FM-2 with a large positive-displacement-type meter, FM-1. The amount of pressurization gas added to the system was measured with a smaller, positive-displacement-type meter, FM-3, located in the pressurization control system. In addition, FM-3 was used to measure the boil-off for the ambient heat-leak measurements when it was determined that the rates were too low for FM-1 to be used for this purpose. These meters are described in more detail below.

FM-1, a Rockwell Manufacturing Co. (Model 10,000) flowmeter, has a maximum rated volumetric flow-rate capacity of 10,000 cu ft/hr. This type of meter is basically a direct-reading volumetric flowmeter; however, for this application it was modified to put out an electrical impulse signal proportional to the mass flow rate. The meter, as purchased,

was equipped with a temperature-modulated valve-bellows linkage mechanism which corrected gas volume to a base temperature of 60°F. The temperature-modulated output of the linkage mechanism drove a Rockwell Type I Emcorrector, which corrected the volume to a base pressure of 14.7 psia. In turn, the pressure- and temperature-corrected index drive on the Emcorrector drove an interrupter-switch assembly which generated, nominally, one pulse per ten cubic feet, corrected to the base pressure and temperature. In addition, an iron-constantan thermocouple was located in the inlet to the meter to permit gas-temperature monitoring.

FM-2, a turbine-type flowmeter made by Potter Aeronautical Company (Model 3-57630) has a signal output of approximately 60 pulses per cubic foot of gas. This meter was used primarily to monitor the start of LH_2 flow and flow-rate stability, since the temperature and inlet specific volume of the gasified H_2 varied as a flow test proceeded.

FM-3, A Rockwell Manufacturing Co., (Model 1600, 1600 cfh capacity) flowmeter, is similar to FM-1. However, the output signal is not directly proportional to mass flow. Inlet gas temperature and pressure were recorded for later conversion of the data to mass flow. The meter was modified by GD/FW to obtain a signal for remote recording. Inlet gas temperature was monitored with an iron-constantan thermocouple. One lead from the thermocouple was routed through a normally closed switch located inside the meter. The switch was opened each time the bellows expanded in the

meter. The gas temperature and flow signal were thereby recorded on the same recorder.

B-4.2 System

FM-1. Output pulses from the meter were recorded on a strip chart. Total flow during a test run was directly proportional to the number of pulses recorded. Flow rate at a particular time was indicated by the pulse repetition rate on the chart. Inlet gas temperature was recorded on a Brown temperature recorder.

FM-2. Output pulses were fed into an amplifier and then to a rate meter whose dc output was recorded on a strip chart.

FM-3. As noted above, the meter modulated the inlet gas temperature signal at a rate proportional to flow. The signal was recorded on a Brown temperature recorder.

B-4.3 Data Processing

The strip-chart records were processed manually. The pulse repetition rates obtained from FM-1 were multiplied by 14.7 (see Section B-4.4 below) to obtain cubic feet per minute (at 14.7 psia, 60°F). These values were in turn corrected to 32°F to obtain flow rates in terms of standard cubic feet per minute.

The FM-2 data were not processed, since the vent-stack flow rate was a control parameter.

The FM-3 data were converted to standard conditions (14.7 psia, 32°F) using the appropriate temperature and pressure data.

B-4.4 Calibration Procedures

FM-1 and FM-3 were calibrated by the manufacturer prior to the test. FM-2 was not calibrated, since it was not to be used for quantitative measurements.

Subsequent to the experiment, correlation tests were run between FM-1 and FM-3 with the meters in series, and FM-3 was calibrated with a Rockwell Manufacturing Co. Flow Prover. FM-1 was not checked because of a thread insert failure which occurred in the outlet from the meter body when being prepared for calibration. The FM-3 calibration showed the meter to read high by 1.1 to 0.8% over the range in which the meter was used during the experiment (500 to 1800 cfh).

The correlation tests showed deviations of less than 5% between FM-3 and the visual, non-pressure-corrected index on FM-1. However, the pressure-corrected index and electrical output from FM-1 was approximately 32% low. Subsequently, the readout assembly (Rockwell Emcorrector with Cryenco switch-interrupter assembly) was removed from FM-1, and the mechanism was driven manually to determine the effects of the loading imposed by the switch-interrupter assembly. If the non-pressure-corrected index is called I_1 and the pressure-corrected index, I_2 (to which the switch was coupled), it was found that the switch would not actuate consistently when the loading imposed was less than that for which a ratio of $I_1/I_2 = 1.22$ was obtained and that the mechanism would jam when the loading was greater than that which produced

a ratio of $I_1/I_2 = 1.67$. The mean of these values, 1.45, is approximately equal to the value obtained during the correlation tests, 1.47. The latter value was used, albeit somewhat arbitrarily, in arriving at a modified pulse-to-cubic-foot conversion factor for the FM-1 data. Instead of a conversion factor of 10 cu ft per pulse, which was the designed factor, a conversion factor of 10 x 1.47 = 14.7 cu ft per pulse was used in processing the data. The possible variation, as indicated by the results discussed above, is from -2.5 to +2.0 cu ft per pulse, or from -17 to +13.5%. The overall accuracy of the conversion factor was taken to be ± 17%.

B-4.5 Performance

As discussed in the preceding section, difficulties with the readout system on FM-1 necessitated placement of limitations of ± 17% on the flow measured with that meter. Taking into consideration other possible errors (reactor power level, pressure measurement, etc.), the overall accuracy of the boil-off (heating) values calculated from the flow data is estimated to be ± 25%.

Pressurization gas utilization, as measured with FM-3, is conservatively estimated to be accurate to within ± 5%, the primary source of error being due to pressure regulator instability during the initial pressurization of the system preceding the flow runs. No difficulty was experienced with either the meter or the readout system.

Note that because of the low flow rates and the high capacity of FM-1, the system was temporarily re-plumbed during

the experiment so that zero power level (reactor) boil-off flow rates could be measured with FM-3.

FM-2 performed satisfactorily. However, more precise information was obtained from liquid-level-detector and thermometer data correlated to liquid volume. This turbine meter was used primarily to monitor variation in flow rate.

B-5 Liquid-Level Measurement

B-5.1 Sensors

Liquid-hydrogen level in the dewar was detected with ten 6.8-kohm, 1/4-w carbon resistors. Self-heating was the least and resistance the highest when the resistors were submerged in the liquid. The sensors were installed on the thermometer positioning rig, as shown in Figure B-4, at positions indicated in Figure 2.3-1 and listed in Table 2.3-1.

B-5.2 System

A simplified circuit diagram is shown in Figure B-6. Current through the resistors was monitored with ten 0-200 microammeters located at the control console and five similar meters located at the LH_2 fill station.

B-5.3 Data Processing

The liquid-level detection system was used primarily for control purposes and, except for cases where the data supplements the available information obtained from the thermometer data on liquid level, has not been reported. Information on liquid-level versus time for the flow runs was obtained from the thermometer data in the following manner: (1) time correlation was established between the thermometer strip-chart records and the

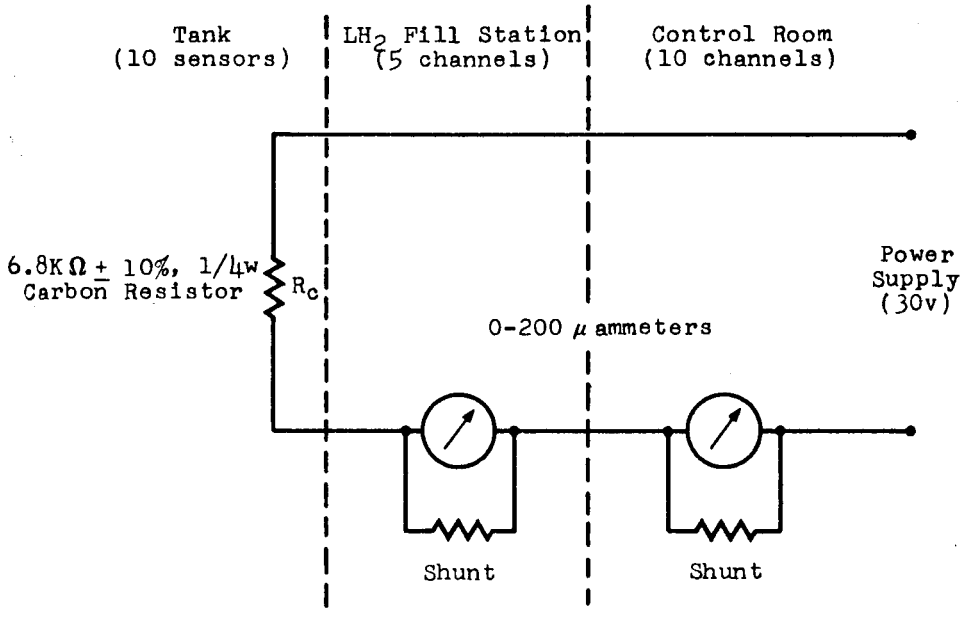

Meter Current: 200 μ a, Temperature R_c = Ambient
50 μ a, Temperature $R_c \approx -420^{\circ}F$

Circuit Current: Approximately 4500 μ a when meter current is 200 μ a.

Figure B-6 Simplified Circuit of Liquid-Level Detectors

data recorded with the Digital Data System (2) a temperature scale was arrived at for each chart record, and (3) the time at which a thermometer registered a temperature corresponding to the saturated vapor temperature was determined from the chart and specified as the time at which the liquid surface was level with the particular thermometer.

B-5.4 Calibration Procedure

Supply voltage to the system was adjusted for full-scale meter deflection (200 μa) with the sensors at or near ambient temperature. Meter current dropped to approximately 75 μa during dewar cool-down, and the current would abruptly drop to 50 μa upon submersion in LH_2.

B-5.5 Performance

As noted previously, the liquid-level detection system was used for control purposes. Performance as such was satisfactory. However, for future tests of this type it is recommended that the system output be coupled to an event recorder in order to obtain a precise record of the liquid level as a function of time, which would be immediately available after the run. Such information is available from the thermometer data only after extensive processing.

The accuracy with which liquid-level-time determinations were made from the thermometer data for the flow runs was affected by (1) thermometer system response time, (2) the accuracy with which the strip-chart curves could be temperature indexed, and (3) the accuracy with which the strip-chart curves could be time indexed. The controlling factor was the last, since

thermometer system responses of the order of 10°R in 0.1 min. were common on the high-flow-rate runs and the slopes of the temperature curves near the saturation temperatures were such that the liquid-level-time determinations were relatively insensitive to errors in temperature determinations. Strip-chart and digital-system data were correlated to within one-half of a sampling period, or $\leq$ 0.16 minute. In terms of liquid level and volume at a specified time, the uncertainty is $\leq$ 0.6 in. and $\leq$ 2.2 gal in the cylindrical portion of the tank.

B-6 Radiation-Intensity Measurement

The radiation detectors used in the liquid hydrogen were all of the integrating type and were chosen for their compatibility with the cryogenic environment.

B-6.1 Gamma Rays

Cobalt-glass dosimeters were used for gamma-ray detection. The glass was supplied by Bausch and Lomb in approximately 19/32- by 1/4-in. rectangular pices 1/16-in.-thick. Each piece of glass was placed in a box of 1/16-in.-thick walls composed of boron-10 and an epoxy binder. These boxes served as low-energy neutron filters and, thus, virtually eliminated any neutron effects in the readings of the dosimeters. The gamma dose was measured by the intensity of discoloration of the cobalt-glass caused by gamma rays. The discoloration intensity was determined by measuring the transmission of wave lengths of 390 and 470 mμ with a spectrophotometer before and after exposure of the glass to radiation. Calibration of this type dosimeter was performed with a 1.5-kc cobalt-60 gamma source. Calibration curves were obtained at 93°F and -320°F. The two

curves differed only slightly, with a maximum difference of the order of 10%. Although the calibration of the dosimeters does not appear to be highly temperature sensitive, the calibration curve obtained at -320°F was used for the dosimeters exposed in liquid hydrogen.

The reproducibility of the gamma measurements was of the order of ± 5%, and the accuracy of the measurements is believed to be about ± 10%.

B-6.2 Neutrons

The neutron-flux distributions were measured with radioactivants. Radioactivants have long been used to obtain neutron flux measurements and are considered to have an accuracy of the order of ± 20%. The thermal-neutron flux was measured by the cadmium-difference technique. The thermal, or sub-cadmium, flux includes neutrons with energies below 0.48 ev., the approximate cadmium-cutoff energy for 20-mil cadmium. Gold foils were used as the thermal-neutron detectors. Copper wires were also used to map thermal-neutron profiles in the liquid hydrogen. The magnitudes of the profiles were normalized to the gold-foil measurements.

No temperature corrections were made on the cross sections used in reducing the gold-foil data. What error this might introduce in the magnitude of the thermal-neutron flux measurements cannot be estimated at this time.

The fast-neutron flux measurements were made with sulfur,

aluminum, and magnesium by utilizing the threshold-type nuclear reactions of each element. These reactions and the approximate effective threshold of each are given below:

Reaction	Threshold (Mev)
$S^{32}(n, p)P^{32}$	2.9
$Mg^{24}(n,p)Na^{24}$	7.5
$Al^{27}(n,\alpha)Na^{24}$	8.1

Although tests indicated that the cryogenic environment produced no adverse physical effects on the pressed sulfur pellets, the pellets were wrapped in aluminum foil as a precautionary measure in the event of shattering or crumbling of the pellet.

After irradiation, all the radioactivants were processed and counted in the semiautomated counting room. The counting data, radiation-exposure data, and detector-location data were processed by a computer program which resulted in a tabulation of the neutron flux for each detector position. Further details of the computer program, detectors, calibration procedures, and techniques used in conjunction with radioactivants as neutron detectors are given in Reference 8.

APPENDIX C

NUCLEAR ANALYSES METHODS

In this appendix the methods and assumptions used in performing the nuclear analyses calculations with the C-17 and COHORT codes are discussed. Complete descriptions of the codes are given in References 1 and 6.

C-1 Methods of C-17 Calculations

The C-17 code, a shield penetration program for calculating a modified gamma spectrum, is based on the differential energy spectra obtained by a moments-method solution of the Boltzmann transport equation (Ref. 9). The fast-neutron portion of the program yields a spectrum that is based upon differential energy spectra calculated by the Nuclear Development Corporation of America (NDA) for a point-isotropic fission source in an infinite medium. The fast-neutron results for this analysis were from an NDA calculation representing a moments-method solution of the Boltzmann transport equation for water (Ref. 10).

For these calculations, the source of nuclear environment, the ASTR, is represented by a total of 126 source points, each of which corresponds to a certain volume element of the core and the power distribution applied thereto. The total power of the reactor core was normalized to one watt for use in the computer program.

A diagram of the calculational model used for the C-17 calculations is shown in Figure C-1. Certain geometric limitations on the description of various regions were encountered

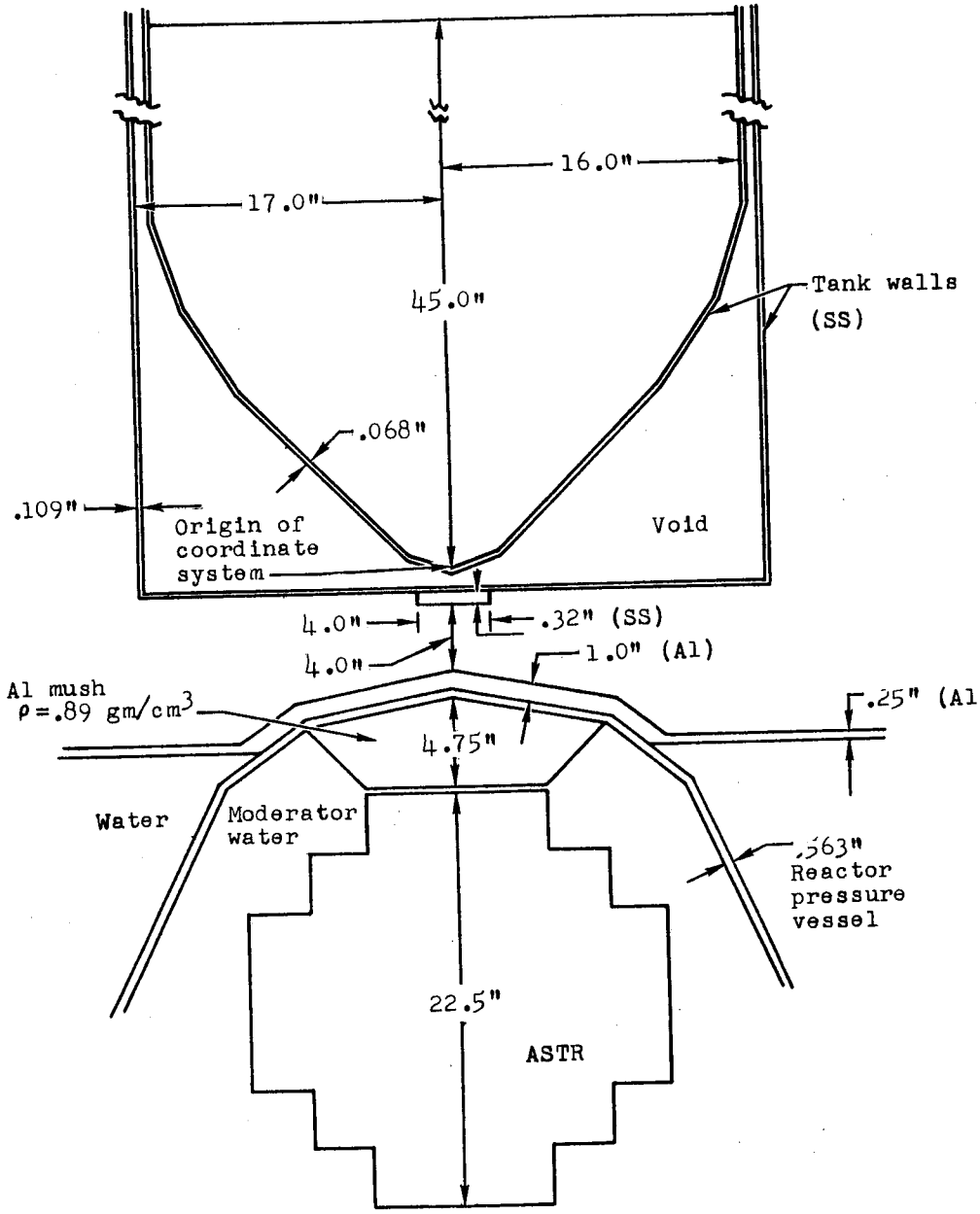

Figure C-1 C-17 Calculational Model: Configuration 1

in the calculational model employed in the shield penetration program. Specifically, any region which is represented as a solid of revolution must have as its axis of revolution the x-axis in a Cartesian coordinate system. In view of this, it is readily seen that some cylindrical regions existed which were not adaptable to this type of geometric definition. For the calculational model, the regions of different materials were defined as precisely as possible. However, in some instances, it was necessary to approximate some curved surfaces by a number of planes. The conical, or bottom, portion of the dewar was represented by a series of frusta of cones. For simplification in defining a calculational model, the axis or centerline of the dewar was chosen as the x-axis with detector locations, etc. being referenced thereto. For convenience, the coordinate system had as its origin the bottom of the inside of the dewar (or a zero liquid level).

Detector locations for which the calculations were made were situated in the x,y plane. Although exact symmetry did not exist in the test geometry for the x,y and x,z planes, several calculations were made to determine the variation of dose rate in the two planes. The difference was extremely small, and the assumption was made that the system was symmetrical in the two planes. Thus, the x,y-plane was chosen arbitrarily as the plane in which to make the calculations. The detector locations were selected so that they would yield a well-defined nuclear map within the liquid hydrogen. In some instances, it was necessary to cross-plot and/or inter-

polate the calculated data in order to obtain a direct comparison with measured data.

The calculated gamma total dose rates consist of several components considered to be the most probable contributors to the total. It is believed that the major sources of secondary gammas were investigated. Some of the sources considered yielded results of negligible importance.

The primary-gamma dose rate is that resulting from the gamma-leakage flux from the reactor. This leakage flux is due to the prompt-fission and decay gammas in the fuel and to the radiative capture and inelastic scattering of neutrons which occur in all materials in the reactor-core structure.

Secondary gamma rays are considered to be those produced by means of radiative capture of thermal neutrons and inelastic scattering of fast neutrons in materials outside of the reactor core. The capture-gamma source materials investigated for this analysis were the liquid hydrogen and the stainless-steel reactor pressure vessel for both configurations. In addition, the captures produced in the four inches of water in Configuration 2 were included. The only source considered for the production of gammas by means of inelastic scattering of fast neutrons was the iron in the stainless-steel pressure vessel around the ASTR.

The thermal- and fast-neutron fluxes employed in the calculation of secondary gamma rays produced in the stainless-steel pressure vessel and in the surrounding water for Configuration 2 were obtained from a neutron map made of the ASTR

pressure vessel prior to this experiment. This particular map was made with the ASTR completely submerged, so that the water appears as an infinite medium. Thus, the calculated fluxes represent perhaps more realistically the Configuration 2 geometry (4 in. of additional water outside the pressure vessel) than the Configuration 1 geometry. From these fluxes measured on the surface of the ASTR pressure vessel, fluxes were obtained by exponential attenuation at the points of interest (source-point locations) in the steel and water.

To compute the intensities of the secondary gamma sources in a particular medium due to neutron capture (n,γ) or neutron inelastic scattering (n, n') reactions, an elemental volume was chosen which was represented by a specific source-point location. The intensity of each source point was then computed from

$$\text{source strength} = V\Sigma\bar{\Phi}$$

where V = volume associated with a particular source point,

Σ = capture or inelastic cross sections, and

$\bar{\Phi}$ = thermal- or fast-neutron flux (n/cm^2-sec) at the point of interest.

Once the source strengths were computed, they became source terms for the computer program (C-17) and, with the appropriate gamma input spectrum for the secondary event under consideration, their contribution to the gamma dose rate in the liquid-hydrogen was calculated.

The C-17 code computes the gamma heat generation rate $Q_\gamma(\bar{r})$ at a point $\bar{r}$ from the equation

$$Q_\gamma(\bar{r}) = K \int_{E_{min}}^{E_{max}} \mu_a(E_\gamma)\, S_\gamma(E_\gamma, \bar{r})\, E_\gamma\, dE_\gamma ,$$

where K = conversion constant;

E_{min} = minimum photon energy in the spectrum;

E_{max} = maximum photon energy;

$\mu_a(E_\gamma)$ = energy absorption coefficient for the reaction, defined as that fraction of the incident photon energy which is dissipated as heat per unit length (it is a function of the material, type of reaction, and photon energy);

$S_\gamma(E_\gamma, \bar{r})$ = gamma spectrum at the point; and

E_γ = photon energy (Mev).

The gamma energy absorption coefficients $\mu a(E_\gamma)$ are defined as

$$\mu_a(E_\gamma) = \mu(E_\gamma) - \mu_{cs}(E_\gamma) ,$$

where $\mu(E_\gamma)$ = total linear absorption coefficient and

$\mu_{cs}(E_\gamma)$ = Compton scattering coefficient.

A similar equation can be written for the calculation of energy deposition by neutrons. The energy absorption coefficient of the gamma energy deposition equation need only be changed to some function $H(E_n)$, which involves the cross section for a given neutron reaction and the energy dissipated as heat by the reaction. Elastic, inelastic, and charged-particle reactions are considered in the C-17 neutron energy deposition.

C-2 Methods of COHORT Calculations

The original approach of the analysis utilizing the COHORT Monte Carlo procedures was to divide the analysis into two parts because of the double symmetry of the experimental configuration and the limitation of 50 material regions to describe the

geometry. The first part of the analysis was devoted to the ASTR and was to generate a source plane to be used in the second part of the analysis. The second part of the analysis was concerned with the nuclear energy deposition rates in the liquid hydrogen.

As it became apparent that considerable computer time would be required to generate a source plane free from large statistical fluctuations, the original approach was abandoned. Instead, the measured radiation distributions on the bottom of the dewar were used to generate a source plane rather than to calculate one, and fission neutron and gamma spectra with isotropic angular distributions were assumed. Emphasis was then placed on calculating the nuclear energy deposition rates in the liquid-hydrogen regions.

The geometry description of the configuration consisted of surfaces of revolution symmetrical about the z-axis and planes perpendicular to the z-axis. The axis defined as the z-axis for the COHORT analysis is referred to as the x-axis in all other discussions of this report. As indicated in Figure C-2, the conical bottom of the liquid-hydrogen tank was approximated by a parabaloid. For the calculation of energy deposition at different levels of hydrogen in the tank, the tank was divided into seven different regions. The geometry describing the liquid-hydrogen tank configuration included 42 regions bounded by 43 boundaries. The materials making up the geometry description were water, iron, aluminum, and hydrogen. Total, scattering, and elastic cross sections for neutrons and total,

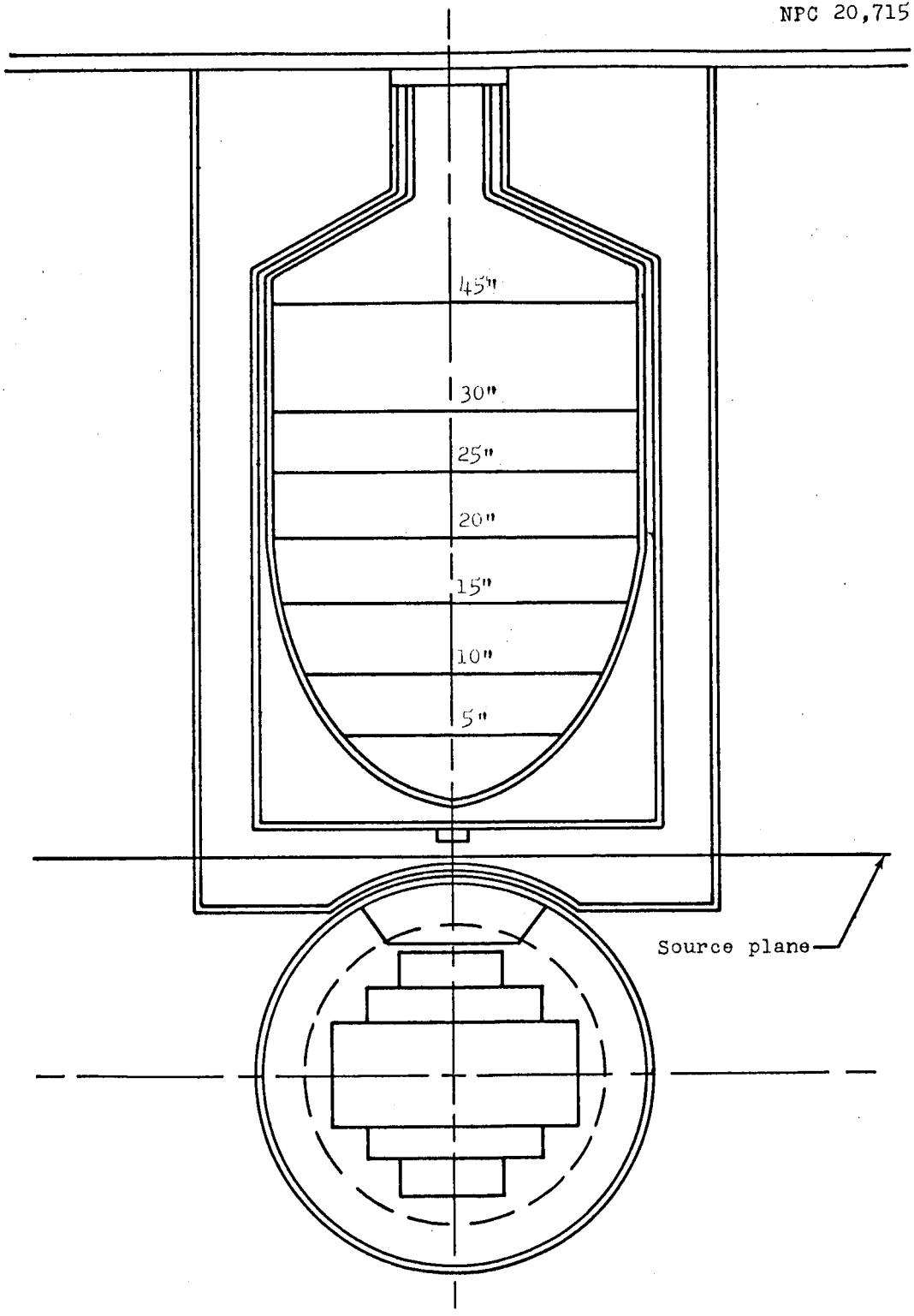

Figure C-2 COHORT Calculational Model

pair-production plus Compton, and Compton cross sections for gamma rays were tabulated for each element. The neutron cross sections were tabulated for energies ranging from 0.2 to 10 Mev, and gamma-ray cross sections were tabulated for energies ranging from 0.05 to 10 Mev. Neutron cross-section data for iron, oxygen, and aluminum were obtained from Reference 11. Hydrogen and uranium data were obtained from Reference 12. The Legendre expansion coefficients for the angular distributions of elastically scattered neutrons were taken from Reference 11 and adapted to the required COHORT input. The gamma cross-section data were taken from Reference 9.

No secondary-gamma calculations were made in this analysis. Since the measured radiation intensities at the bottom of the dewar were used as the source term, only the liquid-hydrogen secondaries that were not considered in this analysis were included in the C-17 analysis. The C-17 analysis indicated that these contributed only about 2 or 3% of the total heating.

In the process of performing these calculations, a new COHORT procedure was developed. The purpose of the procedure is to calculate direct-beam flux at detector points and to search through the COHORT geometry input for possible errors.

REFERENCES

1. Peterson, D. M., Shield Penetration Programs C-17 and L-63. General Dynamics/Fort Worth Report FZK-9-170 (NARF-61-39T, December 1961).

2. Baumeister, T., Mechanical Engineer's Handbook (6th ed.). New York: McGraw-Hill Book Company, Inc. (1958), pp. 4-104, 4-106, and 4-107.

3. Morris, B. E., King, N. D., and Carter, H. G., Measurement of Radiation Heating in Aerospace Structural Materials. General Dynamics/Fort Worth Report FZK-9-187 (NARF-63-8T, 16 September 1963).

4. Price, B. T., Horton, C. C., and Spinney, K. T., Radiation Shielding. New York: Pergamon Press (1957), p. 72.

5. Liquid Hydrogen Technology. General Dynamics/Astronautics Report AE62-0774 (September 1962).

6. Collins, D. G., and DeVries, T. W., Monte Carlo Calculations of Energy Depositions and Radiation Transport, Vols. I and II. General Dynamics/Fort Worth Report FZK-176-1 and -2 (December 1963).

7. Pancoast, J. T., 10-Mw ASTR. General Dynamics/Fort Worth Report FZK-190 (to be published).

8. Dungan, W. E., and Lewis, J. H., Nuclear Measurement Techniques for Radiation-Effects Environmental Testing. General Dynamics/Fort Worth Report FZK-9-185 (NARF-62-4T, March 1962).

9. Goldstein, H., and Wilkins, J. R., Calculations of the Penetration of Gamma Rays. Nuclear Development Associates Report NYO-3075(NDA-15C-41, June 1954).

10. Krumbein, A. D., Summary of NDA Unclassified Results of Moments Calculations for the Penetration of Neutrons Through Various Materials. Nuclear Development Corporation of America Report NDA-92-2 (Rev., August 1957).

11. Troubetzkoy, E. S., Fast-Neutron Cross Sections of Iron, Silicon, Aluminum, and Oxygen. Nuclear Development Corporation of America Report NDA 2111-3 (17 December 1958—30 September 1959).

12. Hughes, D. J., and Schwartz, R. B., Neutron Cross Sections. Brookhaven National Laboratory Report BNL 325 (July 1958).

DISTRIBUTION LIST

National Aeronautics and Space Administration
Washington, D. C. 20546
Attention: RNN/David Novik
Attention: RNN/David J. Miller
Attention: NPO/Harold B. Finger

National Aeronautics and Space Administration
Ames Research Center
Moffet Field, California 94035
Attention: Librarian

National Aeronautics and Space Administration
Goddard Space Flight Center
Greenbelt, Maryland 20771
Attention: Librarian

National Aeronautics and Space Administration
Langley Research Center, Langley Station
Hampton, Virginia 23365
Attention: Librarian

National Aeronautics and Space Administration
Lewis Research Center
21000 Brookpark Road
Cleveland, Ohio 44135
Attention: Librarian (3)
Attention: Hugh M. Henneberry (MS 54-1)
Attention: Herman H. Ellerbrock (MS 54-1)
Attention: Donald J. Connolley (MS 54-1) (20)
Attention: AD&E Procurement Section (MS 54-1)
Attention: Norman T. Musial, Patent Counsel (MS 77-1)
Attention: Solomon Weiss (MS 54-1)
Attention: John C. Liwosz (MS 54-1)

National Aeronautics and Space Administration
Manned Spacecraft Center
Houston, Texas 77001
Attention: Librian

National Aeronautics and Space Administration
George C. Marshall Space Flight Center
Huntsville, Alabama 35812
Attention: Librarian

National Aeronautics and Space Administration
Jet Propulsion Laboratory
4800 Grove Drive
Pasadena, California 91103
Attention: Librian

DISTRIBUTION LIST (Cond't)

National Aeronautics and Space Administration
Space Nuclear Propulsion Office - Cleveland
Lewis Research Center
21000 Brookpark Road
Cleveland, Ohio 44135
Attention: H. S. Tushar (MS 54-2)

U. S. Atomic Energy Commission
Technical Information Service Extension
Post Office Box 62
Oak Ridge, Tennessee (3)

National Aeronautics and Space Administration
Scientific and Technical Information Facility
Box 5700
Bethesda 14, Maryland
Attention: NASA Representative (6
+ 1 reproducible)